

PERFORMANCE EVALUATION OF CURRENT DENSITY BASED MAGNETIC  
RESONANCE ELECTRICAL IMPEDANCE TOMOGRAPHY  
RECONSTRUCTION ALGORITHMS

A THESIS SUBMITTED TO  
THE GRADUATE SCHOOL OF NATURAL AND APPLIED SCIENCES  
OF  
MIDDLE EAST TECHNICAL UNIVERSITY

BY

RASİM BOYACIOĞLU

IN PARTIAL FULFILLMENT OF THE REQUIREMENTS  
FOR  
THE DEGREE OF MASTER OF SCIENCE  
IN  
BIOMEDICAL ENGINEERING  
IN  
ELECTRICAL AND ELECTRONICS ENGINEERING

SEPTEMBER 2009

Approval of the thesis

**PERFORMANCE EVALUATION OF CURRENT DENSITY BASED  
MAGNETIC RESONANCE ELECTRICAL IMPEDANCE TOMOGRAPHY  
RECONSTRUCTION ALGORITHMS**

Submitted by **RASİM BOYACIOĞLU** in partial fulfillment of the requirements for the degree of **Master of Science in Biomedical Engineering, in Electrical and Electronics Engineering Department, Middle East Technical University** by,

Prof. Dr. Canan Özgen  
Dean, Graduate School of **Natural and Applied Sciences**

Prof. Dr. İsmet Erkmen  
Head of Department, **Electrical and Electronics Engineering**

Prof. Dr. Murat Eyüboğlu  
Supervisor, **Electrical and Electronics Engineering Dept., METU**

**Examining Committee Members**

Prof. Dr. Nevzat Güneri Gençer  
Electrical and Electronics Engineering Dept., METU

Prof. Dr. Murat Eyüboğlu  
Electrical and Electronics Engineering Dept., METU

Prof. Dr. Kemal Leblebicioğlu  
Electrical and Electronics Engineering Dept., METU

Assist. Prof. Dr. Yeşim Serinağaoğlu Doğrusöz  
Electrical and Electronics Engineering Dept., METU

Prof. Dr. Ziya İder  
Electrical and Electronics Engineering Dept., Bilkent University

**Date:** 02.09.2009

**I hereby declare that all information in this document has been obtained and presented in accordance with academic rules and ethical conduct. I also declare that, as required by these rules and conduct, I have fully cited and referenced all material and results that are not original to this work.**

Name, Last name: Rasim BOYACIOĞLU

Signature:

# ABSTRACT

## PERFORMANCE EVALUATION OF CURRENT DENSITY BASED MAGNETIC RESONANCE ELECTRICAL IMPEDANCE TOMOGRAPHY RECONSTRUCTION ALGORITHMS

Boyacıoğlu, Rasim

MSc., Department of Electrical and Electronics Engineering, Biomedical  
Engineering

Supervisor : Prof. Dr. B. Murat Eyüboğlu

September 2009, 153 pages

Magnetic Resonance Electrical Impedance Tomography (MREIT) reconstructs conductivity distribution with internal current density (MRCDI) and boundary voltage measurements. There are many algorithms proposed for the solution of MREIT inverse problem which can be divided into two groups: Current density (J) and magnetic flux density (B) based reconstruction algorithms. In this thesis, J-based MREIT reconstruction algorithms are implemented and optimized with modifications. These algorithms are simulated with five conductivity models which have different geometries and conductivity values. Results of simulation are discussed and reconstruction algorithms are compared according to their performances. Equipotential-Projection algorithm has lower error percentages than other algorithms for noise-free case whereas Hybrid algorithm has the best performance for noisy cases. Although J-substitution and Hybrid algorithms have relatively long reconstruction times, they produced the best images perceptually.

Integration along Cartesian Grid Lines and Integration along Equipotential Lines algorithms diverge as noise level increases. Equipotential-Projection algorithm has erroneous lines starting from corners of FOV especially for noisy cases whereas Solution as a Linear Equation System has a typical grid artifact. When performance with data of experiment 1 is considered, only Solution as a Linear Equation System algorithm partially reconstructed all elements which show that it is robust to noise. Equipotential-Projection algorithm reconstructed resistive element partially and other algorithms failed in reconstruction of conductivity distribution. Experimental results obtained with a higher conductivity contrast show that Solution as a Linear Equation System, J-Substitution and Hybrid algorithms reconstructed both phantom elements and Hybrid algorithm is superior to other algorithms in percentage error comparison.

Keywords: electrical impedance tomography, magnetic resonance imaging, current density imaging

# ÖZ

## AKIM YOĞUNLUĞU TABANLI MANYETİK REZONANS ELEKTRİKSEL EMPEDANS TOMOGRAFİSİ GERİÇATIM ALGORİTMALARININ PERFORMANS DEĞERLENDİRMESİ

Boyacıođlu, Rasim

Yüksek Lisans, Elektrik ve Elektronik Mühendisliđi Bölümü, Biyomedikal  
Mühendisliđi

Tez Yöneticisi : Prof. Dr. B. Murat Eyübođlu

Eylül 2009, 153 sayfa

Manyetik Rezonans Elektriksel Empedans Tomografisi (MREIT) akım yoğunluđu (MRCDI) ve yüzey potansiyelleri ölçümleri yardımıyla iletkenlik dağılımını geriçatmaktadır. MREIT geri probleminin çözümünde kullanılan birçok metot ve algoritma vardır. Bu algoritmalar iki gruba ayrılır: Akım (J) ve manyetik akı (B) yoğunluđu tabanlı geriçatım algoritmaları. Bu çalışmada J-tabanlı MREIT geriçatım algoritmaları gerçekleştirilip bazı deđişikliklerle eniyilenmiştir. Bu algoritmaların farklı geometrilere ve iletkenlik deđerlerine sahip beş iletkenlik modeli ile benzetimi yapılmıştır. Benzetim sonuçları yorumlanıp, geriçatım algoritmaları performanslarına göre kıyaslanmıştır. Eşpotansiyel-İzdüşüm algoritması gürültüsüz durum için en düşük hata oranlarına sahipken, gürültülü durumda Karma algoritma en başarılıdır. J-Deđiştirme ve Karma algoritmaları diđer algoritmalara oranla daha uzun geriçatım

sürelerine sahiptir. Buna rağmen bu algoritmaların sonuçları daha başarılıdır. Kartezyen Izgara Çizgileri boyunca İntegral ve Eşpotansiyel Çizgileri boyunca İntegral algoritmaları gürültü seviyesi arttıkça ıraksar. Eşpotansiyel-İzdüşüm algoritmasında gürültülü durumlarda görüntüleme alanının köşelerinden başlayan hatalı çizgiler belirmektedirken Lineer Denklem Sistemi Çözümü ile Geriçatım algoritmasının tipik ızgara artefaktı vardır. İlk yapılan deneyde elde edilen sonuçlara bakıldığında, sadece Lineer Denklem Sistemi Çözümü ile Geriçatım algoritması bütün elemanları kısmi olarak geriçatabilmiştir. Bu da bu algoritmanın gürültüye karşı dirençli olduğunu göstermektedir. Buna karşın, Eşpotansiyel-İzdüşüm algoritması daha yalıtkan olan kare elemanı kısmen geriçatabilmiştir. Diğer algoritmalar deneysel veriler ile görüntü geriçatımında başarısız olmuşlardır. Daha yüksek iletkenlik kontrastına sahip bir fantomla yapılan deney sonucunda, Lineer Denklem Sistemi Çözümü ile Geriçatım, J-Değiştirme ve Karma algoritmalarının her iki fantom elemanını da geriçattığı ve Karma algoritmanın hata oranlarında daha iyi olduğu görülmüştür.

Anahtar Kelimeler: elektriksel empedans görüntüleme, manyetik rezonans görüntüleme, akım yoğunluğu görüntüleme

## ACKNOWLEDGEMENTS

Firstly, I would like to thank my family for their continuous support, understanding and love. I made all my critical decisions and accomplishments in my life with your motivation of “always support, full support”. Thank you for standing behind me.

I would also like to express my gratitude to my supervisor Prof. Dr. Murat Eyübođlu for his guidance throughout the study. Your support and advices for my future plans always meant a lot for me.

I also wish to thank to my lab mates and friends: Evren, Gökhan, Tankut, Ali, Ümit, Hüseyin, Alireza, Ceren, Ersin, Sedat, Berna, Feza, Koray and others for their valuable advice and chats. A special thanks to Emre as he is a statue of typical METU graduate with inquiring questions rather than “right answers” and a relaxed friend with a great humor. Experimental study of this thesis could not be finished without him. And of course, a special thanks to Balkar, I think we will meet somewhere for sure.

I also wish to thank to my friends: Neşe, Alişan, Naim, Sedat, Sinan, Cem, Çevik, Tosun, Yaser, Erkan, Burak, Yunus and others for all valuable memories. Ankara has a meaning just because of you.

A special thanks to my old and current home mates: Moşet, Tapas and Şopar.

Finally, special thanks to Özlem for her support throughout my Master’s study. Everything is easier and delightful with you. My life is completely changed with you and you are the reason for where and who I am.

# TABLE OF CONTENTS

ABSTRACT.....	iv
ÖZ.....	vi
ACKNOWLEDGEMENTS.....	viii
TABLE OF CONTENTS.....	ix
CHAPTER	
1. CHAPTER 1 .....	1
1.1 Objectives of the Thesis .....	5
1.2 Organization of the Thesis .....	6
2. CHAPTER 2 .....	7
2.1 Introduction .....	7
2.2 Problem Definition.....	7
2.3 Forward Problem.....	8
2.4 Inverse Problem .....	10
2.5 Basic MRCDI Procedure and Magnetic Field Extraction.....	11
3. CHAPTER 3 .....	13
3.1 Introduction .....	13
3.2 Reconstruction by Integration Along Equipotential Lines.....	14

3.2.1	Implementation .....	16
3.3	Reconstruction by Integration along Cartesian Grid Lines.....	22
3.3.1	Implementation .....	23
3.4	Reconstruction by Solution of a Linear Equation System using Finite Differences .....	23
3.4.1	Implementation .....	25
3.5	Reconstruction with Equipotential – Projection Algorithm.....	29
3.5.1	Determination of surface potentials .....	30
3.5.2	Obtaining equipotential lines .....	30
3.5.3	Calculation of potential distribution and its gradient.....	30
3.5.4	Obtaining conductivity distribution .....	31
3.6	Reconstruction with J-substitution Algorithm .....	31
3.6.1	Problem and parameter definition.....	32
3.6.2	Reconstruction algorithm.....	33
3.7	J-Substitution and Filtered Equipotential-Projection Based Hybrid Reconstruction Algorithm.....	35
4.	CHAPTER 4 .....	37
4.1	Introduction.....	37
4.2	Simulation Phantoms .....	37
4.2.1	Simulation model 1 .....	38
4.2.2	Simulation model 2 .....	39
4.2.3	Simulation Model 3.....	40

4.2.4	Simulation model 4 .....	41
4.2.5	Thorax phantom .....	42
4.2.6	Experimental phantom .....	44
4.3	Simulation of Measurement Noise.....	46
4.4	Error Calculation and Stopping Criteria .....	47
4.5	Simulation Results for Current Density Based Algorithms .....	48
4.5.1	Simulation Results for Model 1 .....	48
4.5.2	Simulation Results for Model 2 .....	59
4.5.3	Simulation Results for Model 3 .....	72
4.5.4	Simulation Results for Model 4 .....	76
4.5.5	Simulation Results for Thorax Phantom.....	94
4.5.6	Experimental Data.....	102
5.	CHAPTER 5 .....	130
5.1	Conclusions .....	130
5.2	Future work .....	138
	REFERENCES.....	140
	APPENDICES.....	145
	A. MREIT EXPERIMENT PROCEDURE.....	145

# LIST OF TABLES

## TABLES

Table 4.1 Conductivity Values of Thorax Phantom.....	44
Table 4.2 General and Regional Percentage Errors for Simulations with Model 1 ...	58
Table 4.3 General and Regional Percentage Errors for Simulations with Thorax Phantom .....	101
Table 4.4 Circle Element Error Percentages of Reconstructed Images .....	129
Table 5.1 Numerical Values for Star Plot .....	137
Table A.1 Composition of Phantom elements.....	150

# LIST OF FIGURES

## FIGURES

Figure 2.1 Conductivity Model .....	8
Figure 3.1 Pathways of four equipotential lines initiated from the left boundary .....	16
Figure 3.2 Equipotential line $l$ and integration path from $s_1$ to $s$ .....	17
Figure 3.3 The case where 2 equipotential line pass through pixel 2 and a single equipotential line passes through pixel 4. ....	18
Figure 3.4 Flowchart of Integration along Equipotential Lines algorithm .....	21
Figure 3.5 Regions for discretization .....	25
Figure 3.6 . Indices of Logarithmic resistivity, Pixels and Current Densities .....	26
Figure 4.1 Geometry of Simulation Model 1 .....	39
Figure 4.2 Starting position for impulsive elements in Simulation Model 2.....	40
Figure 4.3 End position for impulsive elements in Simulation Model 2 .....	40
Figure 4.4 Geometry of Simulation Model 3.....	41
Figure 4.5 Geometry of Simulation Model 4.....	42
Figure 4.6 Geometry of Thorax Phantom .....	43
Figure 4.7 Two Oblique Views of CAD Simulations of Experimental Phantom.....	45

Figure 4.8 Geometry of Experimental Phantom .....	45
Figure 4.9 Original Conductivity Distribution of Experimental Phantom.....	46
Figure 4.10 Reconstruction Results for Noise-free case a) Original distribution, b) Integration along Cartesian grid lines, c) Integration along equipotential lines, d) Solution as a linear equation system, e) equipotential projection, f) j-substitution, g) hybrid .....	49
Figure 4.11 Reconstruction Results for SNR 30 a) Integration along Cartesian grid lines, b) Integration along equipotential lines, c) Solution as a linear equation system, d) Equipotential-Projection, e) J-Substitution, f) Hybrid.....	52
Figure 4.12 Reconstruction Results for SNR 13 a) Integration along Cartesian grid lines, b) Integration along equipotential lines, c) Solution as a linear equation system, d) Equipotential-Projection, e) J-Substitution, f) Hybrid.....	55
Figure 4.13 Image Profiles for Conductive Case a) Original FWHM, b) Original conductivity distribution with cross-section, c)Integration along Cartesian Grid Lines, d) Integration along Equipotential Lines, e) Solution as a Linear Equation System, f) Equipotential-Projection, g) J-Substitution, h) Hybrid .	60
Figure 4.14 FWHM Values with respect to Position, Conductive Case.....	62
Figure 4.15 Reconstructed Values of Impulsive Elements with respect to Position, Conductive Case.....	64
Figure 4.16 Image Profiles for Resistive Case a) Original FWHM, b) Original conductivity distribution with cross-section, c)Integration along Cartesian Grid Lines, d) Integration along Equipotential Lines, e) Solution as a Linear Equation System, f) Equipotential-Projection, g) J-Substitution, h) Hybrid .	66
Figure 4.17 FWHM Values with respect to Position, Resistive Case.....	68

Figure 4.18 Reconstructed Values of Impulsive Elements with respect to Position, Resistive Case .....	70
Figure 4.19 Reconstructed Images for Model 3 Conductive Case a) Original Distribution, b) Integration along Cartesian Grid Lines, c) Integration along Equipotential Lines, d) Solution as a Linear Equation System, e) Equipotential-Projection, f) J-Substitution, g) Hybrid.....	73
Figure 4.20 Reconstructed Images for Model 3 Resistive Case a) Original Distribution, b) Integration along Cartesian Grid Lines, c) Integration along Equipotential Lines, d) Solution as a Linear Equation System, e) Equipotential-Projection, f) J-Substitution, g) Hybrid.....	75
Figure 4.21 General Errors with Changing Conductivity Contrast, Conductive Case .....	78
Figure 4.22 Square Errors with Changing Conductivity Contrast, Conductive Case	80
Figure 4.23 Average Conductivity Value of Square with Changing Conductivity Contrast, Conductive Case.....	82
Figure 4.24 Average Conductivity Value of Square with Changing Conductivity Contrast , Conductive Case, Zoomed Version.....	83
Figure 4.25 Reconstructed Conductivity Distributions for Model 4 Conductive Case a) Original Distribution, b) Integration along Cartesian Grid Lines, c) Integration along Equipotential Lines, d) Solution as a Linear Equation System, e) Equipotential-Projection, f) J-Substitution, g) Hybrid.....	84
Figure 4.26 General Errors with Changing Conductivity Contrast, Resistive Case ..	86
Figure 4.27 General Errors with Changing Conductivity Contrast, Resistive Case, Zoomed Version.....	87
Figure 4.28 Square Errors with Changing Conductivity Contrast, Resistive Case....	89

Figure 4.29 Square Errors with Changing Conductivity Contrast, Resistive Case, Zoomed Version.....	90
Figure 4.30 Average Conductivity Value of Square with Changing Conductivity Contrast , Resistive Case.....	92
Figure 4.31 Reconstructed Conductivity Distributions for Model 4 Resistive Case a) Original Distribution, b) Integration along Cartesian Grid Lines, c) Integration along Equipotential Lines, d) Solution as a Linear Equation System, e) Equipotential-Projection, f) J-Substitution, g) Hybrid.....	93
Figure 4.32 Reconstructed Images for Thorax Phantom Noise-free case a) Original Distribution, b) Integration along Cartesian Grid Lines, c) Solution as a Linear Equation System, d) Equipotential-Projection, e) J-Substitution, f) Hybrid .....	95
Figure 4.33 Reconstructed Images for Thorax Phantom with SNR 30 a) Integration along Cartesian Grid Lines, b) Solution as a Linear Equation System, c) Equipotential-Projection, d) J-Substitution, e) Hybrid .....	97
Figure 4.34 Reconstructed Images for Thorax Phantom with SNR 13 a) Integration along Cartesian Grid Lines, b) Solution as a Linear Equation System, c) Equipotential-Projection, d) J-Substitution, e) Hybrid .....	100
Figure 4.35 Phase image of $z$ slice for vertical and negative current injection.....	103
Figure 4.36 Phase image of $z$ slice for vertical and positive current injection.....	103
Figure 4.37 $B_z$ image for vertical current injection, in units of Tesla.....	104
Figure 4.38 $B_z$ image for horizontal current injection, in units of Tesla. ....	104
Figure 4.39 Derivative of $B_z$ (T/m) with respect to $x$ direction for vertical current injection.....	105

Figure 4.40 Derivative of $B_z$ (T/m) with respect to $y$ direction for vertical current injection.....	105
Figure 4.41 Derivative of $B_z$ (T/m) with respect to $x$ direction for horizontal current injection.....	106
Figure 4.42 Derivative of $B_z$ (T/m) with respect to $y$ direction for horizontal current injection.....	106
Figure 4.43 $\frac{\partial B_y}{\partial z}$ (T/m) image for vertical current injection .....	108
Figure 4.44 $\frac{\partial B_y}{\partial z}$ (T/m) image for horizontal current injection.....	108
Figure 4.45 $\frac{\partial B_x}{\partial z}$ (T/m) image for vertical current injection .....	109
Figure 4.46 $\frac{\partial B_x}{\partial z}$ (T/m) image for horizontal current injection .....	109
Figure 4.47 $J_x$ ( $A/m^2$ ) image for vertical current injection.....	110
Figure 4.48 $J_y$ ( $A/m^2$ ) image for vertical current injection .....	111
Figure 4.49 $J_x$ ( $A/m^2$ ) image for horizontal current injection .....	111
Figure 4.50 $J_y$ ( $A/m^2$ ) image for horizontal current injection.....	112
Figure 4.51 $J$ ( $A/m^2$ ) image for vertical current injection.....	112
Figure 4.52 $J$ ( $A/m^2$ ) image for horizontal current injection .....	113
Figure 4.53 Arrow Plot for Current Density Distribution of Vertical Current Injection .....	113

Figure 4.54 Arrow Plot for Current Density Distribution of Horizontal Current Injection.....	114
Figure 4.55 Reconstructed Images with Simulated Data for Experiment 1, a) Original Distribution, b) Equipotential-Projection, c) Solution as a Linear Equation System, d) J-Substitution (3 iteration), d) Hybrid (3 iteration).....	115
Figure 4.56 Reconstructed Conductivity (S/m) for Experimental Data with Equipotential-Projection Algorithm.....	116
Figure 4.57 Filtered Version of Reconstructed Conductivity (S/m) with Equipotential-Projection Algorithm.....	117
Figure 4.58 Reconstructed Conductivity (S/m) for Experimental Data of Vertical Current Injection with Equipotential-Projection Algorithm .....	117
Figure 4.59 Reconstructed Conductivity (S/m) for Experimental Data of Horizontal Current Injection with Equipotential-Projection Algorithm .....	118
Figure 4.60 Reconstructed Conductivity Distribution (S/m) with Hybrid Algorithm .....	119
Figure 4.61 Reconstructed Conductivity Distribution (S/m) with J-Substitution Algorithm .....	119
Figure 4.62 Reconstructed Conductivity Distribution (S/m) with Solution as a Linear Equation System Algorithm.....	120
Figure 4.63 $J_x$ ( $A/m^2$ ) Image For Vertical Current Injection, Experiment 2.....	122
Figure 4.64 $J_y$ ( $A/m^2$ ) Image For Vertical Current Injection, Experiment 2 .....	122
Figure 4.65 $J_x$ ( $A/m^2$ ) Image For Horizontal Current Injection, Experiment 2....	123
Figure 4.66 $J_y$ ( $A/m^2$ ) Image For Horizontal Current Injection, Experiment 2 ...	123

Figure 4.67 Arrow Plots a) Vertical Pattern, b)Horizontal Pattern.....	124
Figure 4.68 Reconstructed Images with Simulated Data for Experiment 2, a) Original Distribution, b) Equipotential-Projection, c) Solution as a Linear Equation System, d) J-Substitution (3 iteration), d) Hybrid (3 iteration).....	125
Figure 4.69 General Percentage Errors of a) J-Substitution, b) Hybrid algorithm ..	126
Figure 4.70 Reconstructed Image (S/m) with Equipotential-Projection Alg., Experiment 2 .....	127
Figure 4.71 Reconstructed Image (S/m) with Solution as a Lin. Eq. Sys. Alg., Experiment 2 .....	128
Figure 4.72 Reconstructed Image (S/m) with J-Substitution Alg., Experiment 2 ...	128
Figure 4.73 Reconstructed Image (S/m) with Hybrid Alg., Experiment 2 .....	129
Figure 5.1 Star Plot .....	138
Figure A.1 General Setup for MREIT Experiments.....	145
Figure A.2 RF Coil.....	146
Figure A.3 Current Source a) Front View, b) Back View.....	147
Figure A.4 Plexiglas Phantom, a) Oblique View, b) Upper Side Removed.....	147
Figure A.5 Molds for Phantom Elements, a) Mold for Square Element, b) Mold for Circle Element.....	148
Figure A.6 Phantom with all Elements, a) Phantom Elements, b) Phantom Elements and Background Solution.....	149
Figure A.7 Conductivity Cell.....	149

Figure A.8 MREIT Pulse Sequence.....	150
Figure A.9 Screen Shot Image of MRI software for $B_z$ imaging.....	151
Figure A.10 Screen Shot Image of MRI software for $B_x$ imaging.....	152
Figure A.11 Screen Shot Image of MRI software for $B_y$ imaging.....	153

# CHAPTER 1

## INTRODUCTION

Different properties of biological tissues have been investigated to get more information about human body and develop new imaging modalities. One of these parameters is electrical resistivity of biological tissues. Electrical resistivity of tissues changes for different parts of the body and physiological state [1]. Moreover, tissue impedance is usually modeled as combination of a resistance and a reactance element which forces tissue impedance to vary with frequency [2]. Imaging of impedance distribution inside human body enables to examine human body in a different perspective than conventional imaging modalities like CT and MRI.

Electrical Impedance Tomography (EIT) is an imaging modality which was first proposed by Henderson and Webster [3] and attracts many scientists over the past three decades. Henderson and Webster [3] published first impedance images. However, first tomographic images were obtained and published by Brown and Barber [4] just before they introduced the first clinical impedance tomography system, which is called Applied Potential Tomography (APT). Interested reader for EIT history is guided to [5] and [6].

EIT mainly consists of currents applied between pairs of electrodes on the imaging subject and then measuring surface potentials between remaining electrodes. There are mainly two ways of current application, by injecting via electrodes attached to surface [6] or inducing via a coil around the body with the help of time varying magnetic fields [7] and [8].

Induced EIT studies are extended with addition of contactless measurement system by Gencer and Tek [9],[10] and [11]. After data collection, transfer impedances are calculated with the ratio of measured potentials to applied currents and EIT images are reconstructed with these transfer impedances.

There are many drawbacks of EIT which are studied by many research groups. These are low spatial resolution, low signal-to-noise ratio, image reconstruction in 3D and sensitivity of body measurements to body shape. The typical limitation of EIT is that transfer impedance is constructed with the effect of whole body impedance which brings sensitivity to inner regions to be low. As a result, spatial resolution differs for inner regions and regions close to the boundary. In other words, spatial resolution is position dependent [5].

This limitation showed the need to determine current density data directly from measurements inside the body. However, there was no such non-invasive method until Scott and Joy showed that Magnetic Resonance Imaging (MRI) can be used to measure internal current density data with a relatively high spatial resolution, [12] and [13]. They applied currents attached to the boundary of a phantom and measured magnetic field due to these currents with a suitable MR pulse sequence. Then by taking the curl of magnetic fields, current density data inside the phantom is obtained as (1.1).

$$\mathbf{J} = \nabla \times \mathbf{B} / \mu_0 \quad (1.1)$$

where,  $\mathbf{B} = (B_x, B_y, B_z)$ ,  $\mathbf{J} = (J_x, J_y, J_z)$ , and  $\mu_0$  is the magnetic permeability of free space. A rotation of phantom is necessary to obtain three components of  $\mathbf{B}$ . They called this new imaging Magnetic Resonance Current Density Imaging (MRCDI). Their studies gave birth to a new research area called Magnetic Resonance Electrical Impedance Tomography (MREIT).

MREIT is basically a different form of EIT where current density in imaging object is obtained with MRCDI techniques. Then, conductivity distribution inside imaging object is reconstructed with MREIT reconstruction algorithms. First studies of MREIT were accomplished by Zhang [14], Woo *et al* [15] and Ider and Birgul [16].

Zhang [14] proposed the first MREIT reconstruction algorithm which uses internal current density distribution and many boundary voltage measurements. The algorithm makes use of (1.2),

$$V_{ab} = \int_C \rho \mathbf{J} dl \quad (1.2)$$

where  $V_{ab}$  is the potential difference between two points, a and b, on the boundary,  $C$  is the contour for line integral connecting a and b and  $\rho$  is the resistivity distribution [6]. After discretization of imaging object, a linear system of equations can be formed as (1.3) for  $M$  pixels and  $N$  boundary voltage measurements,

$$\mathbf{V}_{N \times 1} = \mathbf{G}_{N \times M} \mathbf{R}_{M \times 1} + \mathbf{N}_{N \times 1} \quad (1.3)$$

where,  $\mathbf{V}$ ,  $\mathbf{R}$  and  $\mathbf{N}$  are vectors of voltage measurements, resistivity distribution and noise, respectively.  $\mathbf{G}$  is the current density data. Solution of this linear equation system is the resistivity distribution of imaging slice. However, this algorithm needs too many boundary voltage measurements for a solution with a high spatial resolution.

Another early algorithm is proposed by Woo *et al* [15]. They modeled an error function between measured and calculated current density in terms of resistivity distribution. A sensitivity matrix which relates measured current density data to resistivity distribution deviations is employed for minimization of error function. Minimizing the error function means converging to true values of resistivity distribution. Ider and Birgul [16] also used a sensitivity matrix for their algorithm. But, this time sensitivity matrix is formed between magnetic flux measurements and resistivity distribution. An iterative method is also proposed by Eyüboğlu [17] where resistivity distribution is updated after solving internal current density distribution with FEM with the resistivity of previous iteration.

These early studies initiated the research of MREIT and other algorithms. MREIT reconstruction algorithms can be grouped in two categories, using magnetic field  $\mathbf{B}$  directly and current density  $\mathbf{J}$  calculated from  $\mathbf{B}$  [18]. It is important to note that algorithms employing  $\mathbf{J}$  suffer from a technical difficulty which is the need for rotation of imaging object because MRI can only measure only one component of  $\mathbf{B}$  that is parallel to the main magnetic field of MRI system.

**J**-based MREIT reconstruction algorithms in literature are Integration along Equipotential Lines, Integration along Cartesian Grid Lines and Solution as a Linear Equation System algorithms by Ider [19], J-Substitution algorithm [20] and Equipotential-Projection algorithm [21].

## 1.1 Objectives of the Thesis

MREIT research has been conducted by many groups since 1991 after Scott *et al* [12] introduced MRCDI to the literature. There are many techniques used for MREIT inverse problem. Although MREIT literature contains many J-based reconstruction algorithms, most of the studies are based on simulation study. Moreover, these reconstruction algorithms' performances are tested with different simulation phantoms which make it difficult to compare them. In a previous study, Lorca [22] compared some of the reconstruction algorithms with a rather simple phantom. In recent years, MREIT research is focused on experimental study rather than inventing new reconstruction algorithms. As a result, this thesis seeks further investigation of J-based reconstruction algorithms and experimentation with real data. Objectives of this thesis are:

- To implement J-based MREIT reconstruction algorithms in literature
- To optimize implemented J-based MREIT reconstruction algorithms
- To propose a novel current density based reconstruction algorithm
- To evaluate and compare J-based MREIT reconstruction algorithms with a variety of conductivity models
- To compare J-based MREIT reconstruction algorithms' performances with experimental data

Implemented J-based reconstruction algorithms are Integration along Equipotential Lines, Integration along Cartesian Grid Lines and Solution as a Linear Equation system algorithms by by Ider *et al* [19], Equipotential-Projection algorithm by Özdemir and Eyüboğlu [21], [23] and J-Substitution algorithm [20]. Also, a new Hybrid algorithm proposed by Boyacıoğlu and Eyüboğlu [24] is also implemented in the thesis.

## **1.2 Organization of the Thesis**

Chapter 2 includes problem definition, forward and inverse problems of MREIT. Moreover, basic MRCDI techniques to extract current density information are formulated in this chapter. In Chapter 3, theory of reconstruction algorithms are explained in detail with their formulations. Some modifications are done to optimize each reconstruction algorithm and these are explained in implementation sections of Chapter 3. Chapter 4 starts with definition and purposes of constructed simulation phantoms. Then, simulation results for reconstruction algorithms with each simulation phantom are given in subchapters. Furthermore, comparison of performances of reconstruction algorithms is also done. Also, application of reconstruction algorithms to experimental data is carried out in Chapter 4. Finally, Chapter 5 includes the conclusion and future work possibilities.

## CHAPTER 2

### THEORY

#### 2.1 Introduction

In this section, problem definition of MREIT, which includes governing equations and definitions, is given. Then, forward and inverse problem for MREIT are explained in detail. In general, forward problem consists of calculating potential fields in a conductor object for given boundary conditions and conductivity distribution when current is applied on its boundary [18]. However, MREIT forward problem also includes calculation of current density and magnetic fields. On the other hand, inverse problem is the calculation of conductivity distribution of a conductor object when current density inside is given. Different formulations and algorithms are employed for inverse problem.

Forward problem solution can be used both for obtaining simulation data and at each step of an iterative algorithm for the solution of inverse problem. However, in real data experiments current density is extracted with MRCDI techniques. The procedure to obtain current density from magnetic field measurements with MRI is also formulated.

#### 2.2 Problem Definition

In Figure 2.1, current carried by lead wires  $l_1$  and  $l_2$  is applied to a conductive medium  $\Omega$  through electrodes  $E_1$  and  $E_2$  attached on its boundary  $\partial\Omega$ . Let magnitude of current applied be  $I$ . Applied current will flow inside  $\Omega$  according to its resistivity distribution  $\rho$ .

That is, areas with relatively low resistivity will acquire relatively more current density, and vice versa. As a result, current density distribution  $J$  inside  $\Omega$  contains coded information of  $\rho$ .

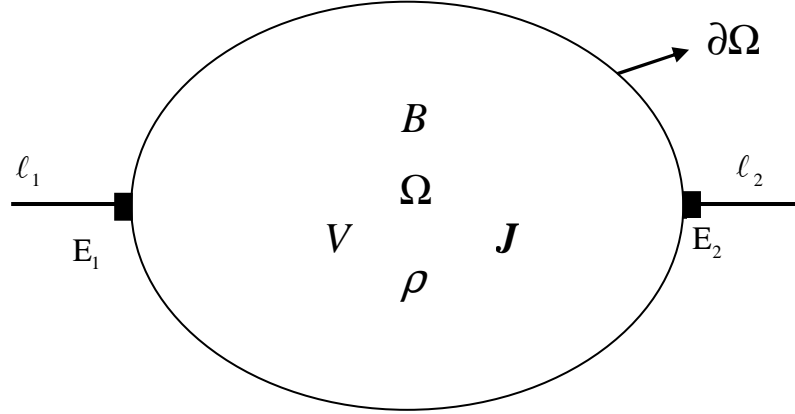


Figure 2.1 Conductivity Model

When resistivity distribution is changed, internal current pathways, thus  $J$ , changes which also effects boundary voltages. In conventional EIT, these boundary voltages are insensitive to local changes and small deviations which brings low spatial resolution and nonlinearity problem [5]. However, measurement of magnetic field  $B$  with MRI and calculation of  $J$  from  $B$  ensures spatial resolution to be same everywhere inside  $\Omega$ .

### 2.3 Forward Problem

Forward problem of MREIT is formulated with the following boundary value problem along with Neumann boundary conditions (2.1).

$$\nabla \cdot \left[ \frac{1}{\rho(\mathbf{r})} \nabla V(\mathbf{r}) \right] = 0 \quad \text{in } \Omega \quad (2.1)$$

$$-\frac{1}{\rho} \nabla V \cdot \mathbf{n} = g \quad \text{on } \partial\Omega$$

where  $\mathbf{n}$ ,  $g$  and  $\mathbf{r}$  are outward unit normal vector on  $\partial\Omega$ , normal component of current  $I$  on  $\partial\Omega$  and a position vector in  $\mathbb{R}^3$ , respectively [6]. Also, current injection electrodes satisfy,

$$\int_{E_j} g ds = \pm I \quad j = 1, 2 \quad (2.2)$$

Sign of  $I$  depends on direction of current injection pattern and  $g$  is obviously nonzero only for the boundary contacting current injection electrodes.

For the unique solution of  $V$ , potential of a single point on  $\partial\Omega$  has to be specified because  $\nabla V$  is uniquely determined with the solution of (2.1). After potential distribution is calculated, electric field  $E$  inside  $\Omega$  can be obtained.

$$E = -\nabla V \quad (2.3)$$

Ohm's law relates current density distribution  $J$  to electric field distribution  $E$  as,

$$\mathbf{J}(\mathbf{r}) = -\frac{1}{\rho} \mathbf{E}(\mathbf{r}) \quad (2.4)$$

Furthermore, Biot-Savart law can be employed to obtain magnetic field  $\mathbf{B}$  inside  $\Omega$ .

$$\mathbf{B}_\Omega(\mathbf{r}) = \frac{\mu_0}{4\pi} \int_\Omega \mathbf{J}(\mathbf{r}') \times \frac{\mathbf{r} - \mathbf{r}'}{|\mathbf{r} - \mathbf{r}'|^3} dv' \quad (2.5)$$

where  $\mu_0$  is the permeability of free space.

Analytical solutions of (2.1) only exist for specific geometries, so numerical methods such as Finite Element Method (FEM) or Boundary Element Method (BEM) need to

be employed. In this thesis, FEM is chosen for forward problem solution [18]. COMSOL Multiphysics software is employed and application mode “2D Conductive Media DC” from “AC/DC module” is used. To ensure true solution of forward problem, a model with homogeneous conductivity distribution and electrodes with size of a single side is constructed. After the solution of forward problem, current density data is extracted and investigated. Extracted current density does not change with position in the direction orthogonal to current injection. Moreover, total current is calculated by integrating current density over a slice which is perpendicular to current direction. Applied and calculated current values turn out to be the same.

## 2.4 Inverse Problem

MREIT inverse problem is the reconstruction of conductivity distribution of a conductor object whose current density or magnetic field distribution is given along with one or two boundary voltage measurements when current is applied on its boundary. As explained earlier, governing equations and formulations differ for each reconstruction algorithm. Some of the algorithms are direct algorithms whereas the others are iterative. Iterative algorithms usually solve forward problem at each iteration and try to minimize an error function to reach true values of conductivity. In this section governing equations for each J-based reconstruction algorithm are explained briefly. Detailed formulation and implementation stages are explained in CHAPTER 3

Ider proposed three algorithms in [19]. All of them are derived from (2.6).

$$\nabla \times \mathbf{E} = 0 \quad (2.6)$$

Since,

$$\mathbf{E} = \rho \mathbf{J} \quad (2.7)$$

(2.6) can be written as,

$$\nabla \times \rho \mathbf{J} = 0 \quad (2.8)$$

After expansion of (2.8), (2.9) can be written,

$$\nabla\rho\times\mathbf{J} + \rho\nabla\times\mathbf{J} = 0 \quad (2.9)$$

With the definition of  $\mathfrak{R} = \ln \rho$ ,

$$\nabla\mathfrak{R}\times\mathbf{J} = -\nabla\times\mathbf{J} \quad (2.10)$$

Since current density  $\mathbf{J}$  is known, (2.10) is used for calculation of  $\mathfrak{R}$  and then  $\rho$ .

Equipotential-Projection algorithm by [21] Özdemir and Eyüboğlu uses Ohm's Law in (2.7) to reconstruct conductivity distribution. Internal potential distribution is calculated with boundary potentials projected inside FOV in the form of equipotential lines.

J-Substitution and Hybrid algorithm solve forward problem at each iteration and update resistivity distribution.

## 2.5 Basic MRCDI Procedure and Magnetic Field Extraction

MRCDI is utilized to obtain current density distribution  $\mathbf{J}$  when current is applied from electrodes attached to the surface of a conductor object. Pioneers of this technique are the Toronto group [25], [12], [13] and [26]. MRCDI can be divided into three basic groups according to the frequency of applied current. VF-MRCDI [27] uses currents with variable frequency below a few kHz whereas RF-MRCDI [28], as the name implies, injects currents with radio frequency. However, the most common and widely used technique is LF-MRCDI which uses low frequency currents. In this thesis, dc currents are employed both for simulation and experimental study. Furthermore, formulation of magnetic field extraction is based on LF-MRCDI.

Z direction is chosen to be parallel to the main magnetic field,  $\mathbf{B}_0$ , of the MRI system. When current  $I$  is applied through electrodes attached to the surface of a conductor object for a  $T_c$  time interval, these currents produce a magnetic field

inhomogeneity,  $\mathbf{B} = (B_x, B_y, B_z)$ , which forces main magnetic field to change to  $\mathbf{B}_0 + \mathbf{B}$  [6]. Actually, it is changed to  $\mathbf{B}_0 + B_z$ , taking only z component of  $\mathbf{B}$ . In consequence, resulting signal equations with positive, (2.11), and with negative, (2.12), current are,

$$S^{I^+}(m, n) = \int \int_{-\infty}^{+\infty} M(x, y) e^{j\gamma B_z(x, y) T_c} e^{j(xm\Delta k_x + yn\Delta k_y)} dx dy \quad (2.11)$$

$$S^{I^-}(m, n) = \int \int_{-\infty}^{+\infty} M(x, y) e^{-j\gamma B_z(x, y) T_c} e^{j(xm\Delta k_x + yn\Delta k_y)} dx dy \quad (2.12)$$

where  $M$  is the transverse magnetization and  $\gamma$  is the gyromagnetic ratio of hydrogen [6]. After taking Fourier transform of signals in (2.11) and (2.12), and then dividing resulting complex images of  $M$  gives,

$$\text{Arg}\left(\frac{M_c^{I^+}(x, y)}{M_c^{I^-}(x, y)}\right) = \text{Arg}(2e^{j\gamma B_z(x, y) T_c}) = \tilde{\Phi}_z(x, y) \quad (2.13)$$

However,  $\tilde{\Phi}_z$  needs unwrapping since it is wrapped to  $[-\pi, \pi]$  interval. In the end, magnetic flux density due to injection current can be extracted as in (2.14).

$$B_z(x, y) = \frac{1}{2\gamma T_c} \Phi_z(x, y) \quad (2.14)$$

where  $\Phi_z$  is unwrapped version of  $\tilde{\Phi}_z$ .

## CHAPTER 3

### CURRENT DENSITY BASED RECONSTRUCTION ALGORITHMS

#### 3.1 Introduction

In Chapter 3, theories and formulation of reconstruction algorithms are given. Furthermore, modifications to optimize the performance of each reconstruction algorithm are explained in detail in implementation subchapters.

In Section 2.4, Equation (2.10) set the relation between logarithmic resistivity and current density distribution as,

$$\nabla \mathfrak{R} \times \mathbf{J} = -\nabla \times \mathbf{J} \quad (3.1)$$

After applying curl operator and rearranging terms, Equation (3.2) is obtained in a matrix form.

$$\begin{bmatrix} 0 & J_z & -J_y \\ -J_z & 0 & J_x \\ J_y & -J_x & 0 \end{bmatrix} \begin{bmatrix} \frac{\partial \mathfrak{R}}{\partial x} \\ \frac{\partial \mathfrak{R}}{\partial y} \\ \frac{\partial \mathfrak{R}}{\partial z} \end{bmatrix} = - \begin{bmatrix} \frac{\partial J_z}{\partial y} - \frac{\partial J_y}{\partial z} \\ \frac{\partial J_x}{\partial z} - \frac{\partial J_z}{\partial x} \\ \frac{\partial J_y}{\partial x} - \frac{\partial J_x}{\partial y} \end{bmatrix} \quad (3.2)$$

Equation (3.2) is the starting point for Ider algorithms. On the other hand, Equipotential-Projection algorithm makes use of Ohm's law and J-Substitution algorithm reconstructs conductivity distribution iteratively.

## 3.2 Reconstruction by Integration Along Equipotential Lines

Ider [19] stated that method of characteristics is a common technique used for the solution of a single first order linear partial differential equation. The formulation is the following.

Let us define, a first order linear partial differential equation with a vector field  $A(x)$  and scalar field  $b(x)$ , where  $x = [x \ y \ z]^T$ , as

$$A \cdot \nabla u = b \quad (3.3)$$

This system has a characteristic curves in the form of an integral curve  $x(s)$  such that,

$$x'(s) = A(x(s)) \quad (3.4)$$

where  $x' = dx/ds$ . So, any characteristic curve starting from point  $s_0$ , can be formulated with Equation (3.5).

$$x(s) = x(s_0) + \int_{s_0}^s A(x(t))dt \quad (3.5)$$

Also,

$$\frac{d}{ds}u(x(s)) = \nabla u \cdot x'(s) = b(x(s)) \quad (3.6)$$

Equation (3.6) means that, on the characteristic curve of system defined in Equation (3.3), solution of  $u$  can be found if its value is defined on a single point,  $s = s_1$ , as in Equation (3.7),

$$u(s) = u(s_1) + \int_{s_1}^s b(x(t))dt \quad (3.7)$$

In the case of Integration Along Equipotential Lines, the single first order linear partial differential equation turns out to be,

$$\frac{\partial \mathfrak{K}}{\partial x} J_y - \frac{\partial \mathfrak{K}}{\partial y} J_x = -\left(\frac{\partial J_y}{\partial x} - \frac{\partial J_x}{\partial y}\right) \quad (3.8)$$

or

$$\tilde{\mathbf{J}}_3 \cdot \nabla \mathfrak{K} = -(\nabla \times \mathbf{J})_3 \quad (3.9)$$

This equation has characteristic curves defined by  $x'(s) = \tilde{\mathbf{J}}_3(x(s))$  staying on a plane with constant  $z$  value. That is, there is no variation in  $z$  direction.

Let us now assume  $z = z_0$  plane where  $z_0$  is constant and denote the intersection of this plane with  $\Omega$  as  $\Omega_{xy}^{z_0}$ .  $\left[\frac{\partial \mathfrak{K}}{\partial x} \quad \frac{\partial \mathfrak{K}}{\partial y}\right]^T$  is the gradient of  $\mathfrak{K}$  on  $\Omega_{xy}^{z_0}$  where  $z$  dependence is omitted and left hand side of Equation (3.8) is the projection of this gradient on  $\left[J_y \quad -J_x\right]^T$  direction. So, left hand side of Equation (3.8) is perpendicular to current direction  $\left[J_x \quad J_y\right]^T$  and current streamlines. As a result, characteristic curves of system defined in (3.8) and (3.9),  $x'(s) = \tilde{\mathbf{J}}_3(x(s))$ , are equipotential lines. That result gives the opportunity to use method of characteristics to calculate  $\mathfrak{K}$  in  $\Omega_{xy}^{z_0}$  by integrating along equipotential lines if  $\mathfrak{K}$  is known for at least one point on each equipotential line.

Ider [19] explains explicitly the need for at least two current injection patterns for unique solution. Let us assume there are two current injection patterns,  $\mathbf{J}^1$  and  $\mathbf{J}^2$  being current density distributions for these patterns. Moreover,  $\mathbf{J}_{xy}^1$  and  $\mathbf{J}_{xy}^2$  are projections of  $\mathbf{J}^1$  and  $\mathbf{J}^2$  in  $\Omega$  onto  $\Omega_{xy}^{z_0}$ . If the condition  $\mathbf{J}_{xy}^1 \times \mathbf{J}_{xy}^2 \neq \mathbf{0}$  is satisfied for each current injection pattern and for all equipotential lines, then assigning one pixel in  $\Omega_{xy}^{z_0}$  with its true  $\mathfrak{K}$  value ensures true calculation of  $\mathfrak{K}$  distribution in  $\Omega_{xy}^{z_0}$ .

### 3.2.1 Implementation

#### 3.2.1.1 Equipotential Lines

To obtain equipotential lines, current density distribution is utilized with the fact that equipotential lines are perpendicular to current streamlines.

Equipotential lines are initialized from pixels on the same boundary of the imaging phantom. Since the starting point and current streamline direction is known in a single pixel on the boundary, the point which the equipotential line exists for that pixel is found. The same procedure is applied to the pixel which the equipotential line is entering next. As a stopping criterion, when the equipotential line reaches a boundary of the imaging phantom, the calculation of that equipotential line is finished.

A simple example is shown in Figure 3.1. Here, four equipotential lines are initiated from the left boundary.

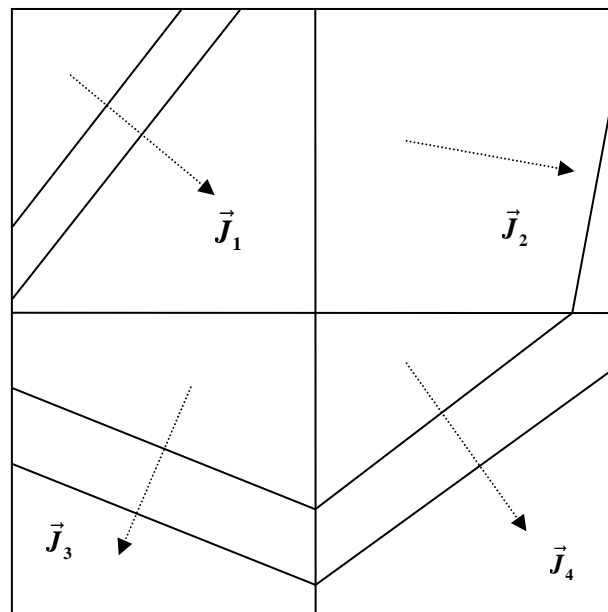


Figure 3.1 Pathways of four equipotential lines initiated from the left boundary

### 3.2.1.2 Formulation of Integration

Lorca [22] explained the formulation of integration in detail. The integration of  $\mathfrak{R}$  over the entire imaging region is done with Equation (3.10), which is the solution of first order linear partial differential equation in (3.8) with method of characteristics.

$$\mathfrak{R}(s) = \mathfrak{R}(s_1) + \int_{s_1}^s - \left( \frac{\partial J_y}{\partial x} - \frac{\partial J_x}{\partial y} \right) d\vec{l} \quad (3.10)$$

Here,  $d\vec{l}$  is the differential element on the integration path  $l$ , i.e. equipotential line, which is illustrated in Figure 3.2.

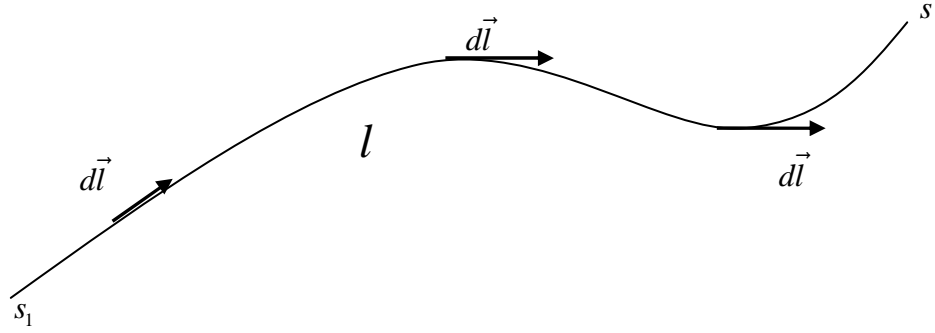


Figure 3.2 Equipotential line  $l$  and integration path from  $s_1$  to  $s$

For Cartesian coordinates, Equation (3.10) takes the form

$$d\vec{l} = (dx, dy) \quad (3.11)$$

and

$$\mathfrak{R}(s) = \mathfrak{R}(s_1) - \int_{s_1}^s \frac{\partial J_y}{\partial x} dx + \int_{s_1}^s \frac{\partial J_x}{\partial y} dy \quad (3.12)$$

With the discretization of Equation (3.12) with trapezoidal method of integration, Equation (3.13) is obtained.

$$\mathfrak{R}(s) = \mathfrak{R}(s_1) - \left[ \frac{\partial J_y(s_1)}{\partial x} + \frac{\partial J_y(s)}{\partial x} \right] \frac{(s_x - s_{1x})}{2} + \left[ \frac{\partial J_x(s_1)}{\partial y} + \frac{\partial J_x(s)}{\partial y} \right] \frac{(s_y - s_{1y})}{2} \quad (3.13)$$

Also, differential elements are changed as,

$$\Delta x = s_x - s_{1x} \quad \text{and} \quad \Delta y = s_y - s_{1y} \quad (3.14)$$

The final formulation is

$$\mathfrak{R}(s) = \mathfrak{R}(s_1) - \left[ \frac{\partial J_y(s_1)}{\partial x} + \frac{\partial J_y(s)}{\partial x} \right] \frac{\Delta x}{2} + \left[ \frac{\partial J_x(s_1)}{\partial y} + \frac{\partial J_x(s)}{\partial y} \right] \frac{\Delta y}{2} \quad (3.15)$$

Consider the system illustrated in Figure 3.3 where two equipotential lines are initiated from the left boundary. Assuming logarithmic resistivity in pixel 1 and 3 are known, pixel 2 and 4 can be calculated.

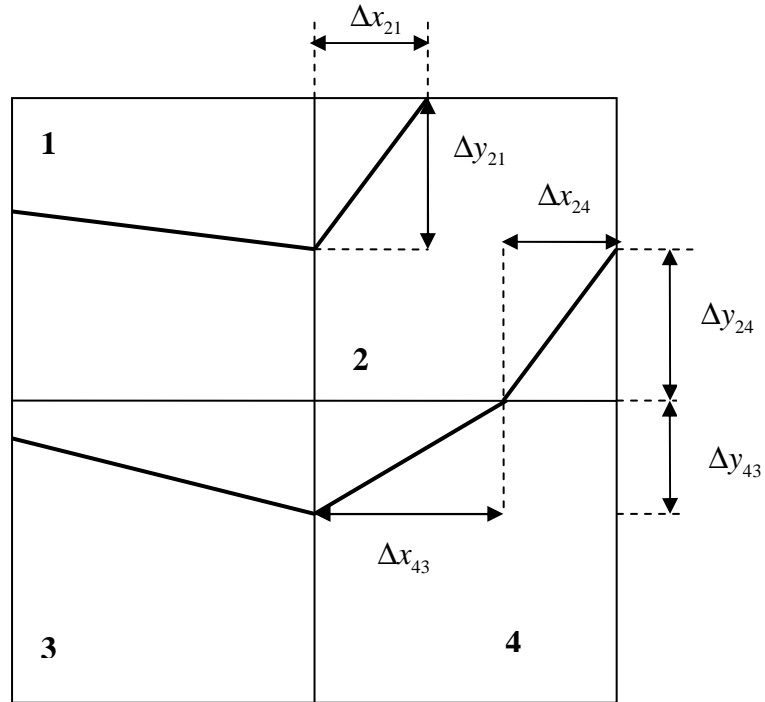


Figure 3.3 The case where 2 equipotential line pass through pixel 2 and a single equipotential line passes through pixel 4.

Assuming pixel 3 is known, logarithmic resistivity in 4 can be calculated as,

$$\Re(4) = \Re(3) - \left[ \frac{\partial J_y(3)}{\partial x} + \frac{\partial J_y(4)}{\partial x} \right] \frac{\Delta x_{43}}{2} + \left[ \frac{\partial J_x(3)}{\partial y} + \frac{\partial J_x(4)}{\partial y} \right] \frac{\Delta y_{43}}{2} \quad (3.16)$$

After pixel 4 is processed, logarithmic resistivity in pixel 2 can be calculated. But in this case, both pixel 4 and 1 are taken into account for calculation of logarithmic resistivity in pixel 2 because equipotential lines entering pixel 2 are coming from pixel 4 and 1. Thus, an averaging is utilized as in Equation (3.17).

$$\begin{aligned} \Re(2) = & \frac{1}{2} \left[ \Re(1) - \left[ \frac{\partial J_y(1)}{\partial x} + \frac{\partial J_y(2)}{\partial x} \right] \frac{\Delta x_{21}}{2} + \left[ \frac{\partial J_x(1)}{\partial y} + \frac{\partial J_x(2)}{\partial y} \right] \frac{\Delta y_{21}}{2} \right] + \\ & \frac{1}{2} \left[ \Re(4) - \left[ \frac{\partial J_y(4)}{\partial x} + \frac{\partial J_y(2)}{\partial x} \right] \frac{\Delta x_{24}}{2} + \left[ \frac{\partial J_x(4)}{\partial y} + \frac{\partial J_x(2)}{\partial y} \right] \frac{\Delta y_{24}}{2} \right] \end{aligned} \quad (3.17)$$

For a generalization of Equation (3.17), Equation (3.18) can be constructed for a pixel  $r_0$  which has  $n$  equipotential lines coming each one from a previous pixel  $r_i$ .

$$\Re(r_0) = \frac{1}{n} \sum_{i=1}^n \left[ \Re(r_i) - \left[ \frac{\partial J_y(r_i)}{\partial x} + \frac{\partial J_y(r_0)}{\partial x} \right] \frac{\Delta x_{0i}}{2} + \left[ \frac{\partial J_x(r_i)}{\partial y} + \frac{\partial J_x(r_0)}{\partial y} \right] \frac{\Delta y_{0i}}{2} \right] \quad (3.18)$$

To calculate  $\Re$  in a pixel, *a priori* information is needed. *A priori* information is the  $\Re$  values of the previous pixels from which equipotential lines are coming. That condition forces the algorithm to be recursive.

The algorithm is implemented as the following. Starting from the end pixel of each equipotential line, for each equipotential line in that end pixel, it is checked if previous pixels of these equipotential line are processed. If all the previous pixels are processed, the end pixel is calculated. Generally, that is not the case. So, previous pixels of the end pixel are processed in the same manner, recursively. In the end, all the previous pixels contributing to calculation of that end pixel directly or indirectly are processed and the end pixel can be processed. The algorithm will continue with the second equipotential line. When all the end pixels are processed, the algorithm stops.

Flowchart of the algorithm is illustrated in Figure (4). There are  $n$  equipotential lines,  $l_i$ ,  $i = 1, 2, \dots, n$  with end pixels,  $\mathfrak{R}(x_{l_i}, y_{l_i})$ .

Current density derivatives are calculated with Sobel operators as explained in [12].

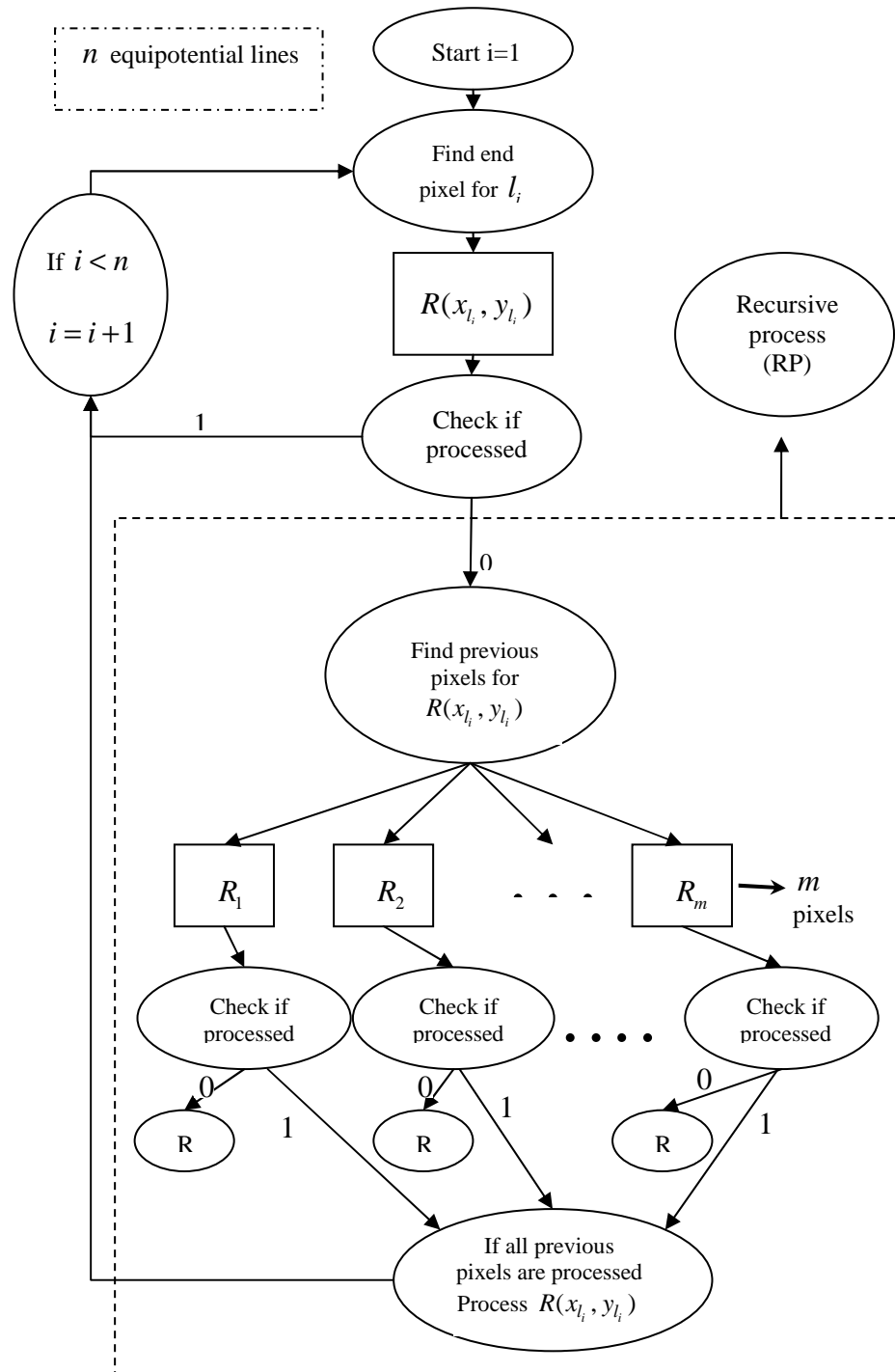


Figure 3.4 Flowchart of Integration along Equipotential Lines algorithm

### 3.3 Reconstruction by Integration along Cartesian Grid Lines

Ider [19] stated that a potential function in  $\Omega$  can be found if its gradient is known in  $\Omega$  except for an additional constant. The exact function can be calculated by specifying the potential function in a single point in  $\Omega$ . In the case of Reconstruction by Integration Along Cartesian Grid Lines algorithm, potential function corresponds to logarithmic resistivity distribution. Reconstruction of true logarithmic resistivity distribution is ensured by assigning a single pixel with its true logarithmic resistivity value.

In the case of a single current injection pattern, gradient of  $\mathfrak{R}$  can not be calculated since the determinant of coefficient matrix in (3.2) is zero. That is, at least two current injection patterns should be utilized. Let us assume, two current injection patterns are applied,  $J^1$  and  $J^2$  are corresponding current density distributions. As a result, third row Equation (3.2) can be rewritten with the concatenation of the two current density distributions as,

$$\begin{bmatrix} J_y^1 & -J_x^1 \\ J_y^2 & -J_x^2 \end{bmatrix} \begin{bmatrix} \frac{\partial \mathfrak{R}}{\partial x} \\ \frac{\partial \mathfrak{R}}{\partial y} \end{bmatrix} = \begin{bmatrix} \frac{\partial J_x^1}{\partial y} & \frac{\partial J_y^1}{\partial x} \\ \frac{\partial J_x^2}{\partial y} & \frac{\partial J_y^2}{\partial x} \end{bmatrix} \quad (3.19)$$

$\begin{bmatrix} \frac{\partial \mathfrak{R}}{\partial x} & \frac{\partial \mathfrak{R}}{\partial y} \end{bmatrix}^T$  can be calculated at any point (x,y,z) if  $-J_y^1 J_x^2 + J_y^2 J_x^1$  is not zero at that point. General form of that condition is,

$$J_{xy}^1 \times J_{xy}^2 \neq 0 \quad (3.20)$$

where  $J_{xy}^1$  and  $J_{xy}^2$  are projections of  $J_1$  and  $J_2$  onto the xy plane, respectively.

For 2-D case, where imaging slice is on xy plane, first and second rows of Equation (3.2) are not considered since, z dependence is omitted and calculation of  $\frac{\partial \mathfrak{R}}{\partial z}$  is unnecessary.

### 3.3.1 Implementation

The coefficient matrix on the left hand side of Equation (3.19),

$$\begin{bmatrix} J_y^1 & -J_x^1 \\ J_y^2 & -J_x^2 \end{bmatrix} \quad (3.21)$$

and the right hand side of Equation (3.19),

$$\begin{bmatrix} \frac{\partial J_x^1}{\partial y} & \frac{\partial J_y^1}{\partial x} \\ \frac{\partial J_x^2}{\partial y} & \frac{\partial J_y^2}{\partial x} \end{bmatrix} \quad (3.22)$$

are calculated for each pixel. Sobel operators [12] are utilized for calculation of current derivatives. After gradients of logarithmic resistivity  $\mathfrak{R}$  are obtained for every pixel in the imaging slice, logarithmic resistivity distribution can be calculated from a point which is assigned with its true  $\mathfrak{R}$  value.

## 3.4 Reconstruction by Solution of a Linear Equation System using Finite Differences

Reconstruction by Solution as a Linear Equation System depends on discretization of Equation (3.8), which is third row of Equation (3.2) with finite differences. For 2-D case, Equation (3.2) is reduced to Equation (3.8) assuming the imaging slice is on xy plane.

Discretization of Equation (3.8) with central differences for inner elements results in

$$\begin{aligned}
& \frac{1}{2\Delta x} \left[ (\mathfrak{R}_{i+1,j} - \mathfrak{R}_{i-1,j})(J_y)_{i,j} \right] - \frac{1}{2\Delta y} \left[ (\mathfrak{R}_{i,j+1} - \mathfrak{R}_{i,j-1})(J_x)_{i,j} \right] \\
& = - \left[ \frac{1}{2\Delta x} \left( (J_y)_{i+1,j} - (J_y)_{i-1,j} \right) - \frac{1}{2\Delta y} \left( (J_x)_{i,j+1} - (J_x)_{i,j-1} \right) \right]
\end{aligned} \tag{3.23}$$

where  $i$  and  $j$  are indices of elements in the  $x$  and  $y$  directions, respectively.  $\Delta x$  and  $\Delta y$  stands for differential elements. For boundary and corner elements' discretization, backward or forward differences are used. After Equation (3.8) is discretized for all elements, the matrix representation of the equations of all rectangular mesh elements is obtained as in Equation (3.24).

$$\mathbf{CR} = \mathbf{B} \tag{3.24}$$

Here,  $R$  represents logarithmic resistivity values of rectangular mesh elements and  $N$  is number of elements in a row.

$$R = \left[ R_1 \quad R_2 \quad \dots \quad R_{N^2-1} \quad R_{N^2} \right]^T \tag{3.25}$$

$C$  is a  $N^2 \times N^2$  matrix consisting of coefficients of  $R$ s on the left hand side of Equation (3.23). That is, multiplication of each row of  $C$  with  $R$  gives the left hand side of Equation (3.23) for a particular element. On the other hand, each row of  $B$  is the right hand side term of Equation (3.23) for that particular element.

For  $M$  different current injection patterns, there are  $M$  different matrix representations of Equation (3.24). These are concatenated to form a combined set of equations as,

$$\begin{bmatrix} C_1 \\ C_2 \\ \vdots \\ C_{M-1} \\ C_M \end{bmatrix} R = \begin{bmatrix} B_1 \\ B_2 \\ \vdots \\ B_{M-1} \\ B_M \end{bmatrix} \tag{3.26}$$

After combined set of equations is obtained, logarithmic resistivity values can be reconstructed with a matrix inversion.

### 3.4.1 Implementation

Let the imaging slice in  $xy$  plane  $\Omega: (-D, D) \times (-D, D)$  be divided into  $N \times N$  pixels. In all the pixels,  $\Omega_{i,j}$ , current density  $J$  and logarithmic resistivity  $\mathfrak{R}$  is assumed constant where  $i$  and  $j$  are indices in the  $y$  and  $x$  directions, respectively. Moreover, positive  $x$  and  $y$  directions are taken as right and up, respectively. As discussed earlier, discretization of Equation (3.8) will be different for interior, boundary and corner pixels. These regions and formulation of indices for logarithmic resistivity, pixels, and current densities are shown in Figure 3.5 and Figure 3.6, respectively.

1	2	3
4	5	6
7	8	9

Figure 3.5 Regions for discretization

Starting with inner pixels, i.e. region 5,

$$2 \leq i \leq N-1, \quad 2 \leq j \leq N-1 \quad \text{and} \quad \Delta x = \Delta y = 2D/N,$$

Equation (3.8) is discretized with central differences as,

$$\begin{aligned} & \frac{Jy}{2\Delta x} R_{(i-1)N+j+1} - \frac{Jy}{2\Delta x} R_{(i-1)N+j-1} - \frac{Jx}{2\Delta y} R_{(i-2)N+j} + \frac{Jx}{2\Delta y} R_{iN+j} \\ & = \frac{Jx_{i-1,j} - Jx_{i+1,j}}{2\Delta y} - \frac{Jy_{i,j+1} - Jy_{i,j-1}}{2\Delta x} \end{aligned} \quad (3.27)$$

	$\Omega_{i-1,j} R_{(i-2)N+j}$ $Jx_{i-1,j} Jy_{i-1,j}$	
$\Omega_{i,j-1}$ $R_{(i-1)N+j-1}$ $Jx_{i,j-1} Jy_{i,j-1}$	$\Omega_{i,j} R_{(i-1)N+j}$ $Jx_{i,j} Jy_{i,j}$	$\Omega_{i,j+1}$ $R_{(i-1)N+j+1}$ $Jx_{i,j+1} Jy_{i,j+1}$
	$\Omega_{i+1,j} R_{iN+j}$ $Jx_{i+1,j} Jy_{i+1,j}$	

Figure 3.6 . Indices of Logarithmic resistivity, Pixels and Current Densities

For discretization of upper side pixels, i.e. region 2, central differences are used for x direction. On the other hand, backward difference is used for y direction. That is,

$$i = 1, 2 \leq j \leq N - 1,$$

$$\begin{aligned} & \frac{Jy}{2\Delta x} R_{(i-1)N+j+1} - \frac{Jy}{2\Delta x} R_{(i-1)N+j-1} - \frac{Jx}{\Delta y} R_{(i-1)N+j} + \frac{Jx}{\Delta y} R_{iN+j} \\ &= \frac{Jx_{i,j} - Jx_{i+1,j}}{\Delta y} - \frac{Jy_{i,j+1} - Jy_{i,j-1}}{2\Delta x} \end{aligned} \quad (3.28)$$

In the case of lower side pixels, i.e. region 8, central differences and forward differences are used for x and y directions, respectively. Then, Equation (3.8) becomes,

$$i = N, 2 \leq j \leq N - 1$$

$$\begin{aligned} & \frac{Jy}{2\Delta x} R_{(i-1)N+j+1} - \frac{Jy}{2\Delta x} R_{(i-1)N+j-1} - \frac{Jx}{\Delta y} R_{(i-2)N+j} + \frac{Jx}{\Delta y} R_{(i-1)N+j} \\ &= \frac{Jx_{(i-1),j} - Jx_{i,j}}{\Delta y} - \frac{Jy_{i,j+1} - Jy_{i,j-1}}{2\Delta x} \end{aligned} \quad (3.29)$$

For left side pixels, i.e. region 4, forward and central differences are used for x and y directions, respectively as shown in Equation (3.30).

$$2 \leq i \leq N-1, j = 1$$

$$\begin{aligned} & \frac{Jy}{\Delta x} R_{(i-1)N+j+1} - \frac{Jy}{\Delta x} R_{(i-1)N+j} - \frac{Jx}{2\Delta y} R_{(i-2)N+j} + \frac{Jx}{2\Delta y} R_{iN+j} \\ &= \frac{Jx_{(i-1),j} - Jx_{i+1,j}}{2\Delta y} - \frac{Jy_{i,j+1} - Jy_{i,j}}{\Delta x} \end{aligned} \quad (3.30)$$

Region 6 pixels, which are on the right boundary, are discretized with central difference and backward difference for y and x directions, respectively as in Equation (3.31).

$$2 \leq i \leq N-1, j = N$$

$$\begin{aligned} & \frac{Jy}{\Delta x} R_{(i-1)N+j} - \frac{Jy}{\Delta x} R_{(i-1)N+j-1} - \frac{Jx}{2\Delta y} R_{(i-2)N+j} + \frac{Jx}{2\Delta y} R_{iN+j} \\ &= \frac{Jx_{(i-1),j} - Jx_{i+1,j}}{2\Delta y} - \frac{Jy_{i,j} - Jy_{i,j-1}}{\Delta x} \end{aligned} \quad (3.31)$$

Left-up corner pixel in region 1 is a combination of upper and left side discretization formulas. That is, forward difference in x direction and backward difference in y direction is applied to Equation (3.8), which results in Equation (3.32).

$$i = 1, j = 1$$

$$\begin{aligned} & \frac{Jy}{\Delta x} R_{(i-1)N+j+1} - \frac{Jy}{\Delta x} R_{(i-1)N+j} - \frac{Jx}{\Delta y} R_{(i-1)N+j} + \frac{Jx}{\Delta y} R_{iN+j} \\ &= \frac{Jx_{i,j} - Jx_{i+1,j}}{\Delta y} - \frac{Jy_{i,j+1} - Jy_{i,j}}{\Delta x} \end{aligned} \quad (3.32)$$

With the same logic, right-up corner pixel in region 3 is formulated, Equation (3.33), with combination of Equation (3.28) and Equation (3.31) for upper and right side discretizations, respectively.

$$i = 1, j = N$$

$$\begin{aligned} & \frac{Jy}{\Delta x} R_{(i-1)N+j} - \frac{Jy}{\Delta x} R_{(i-1)N+j-1} - \frac{Jx}{\Delta y} R_{(i-1)N+j} + \frac{Jx}{\Delta y} R_{iN+j} \\ &= \frac{Jx_{i,j} - Jx_{i+1,j}}{\Delta y} - \frac{Jy_{i,j} - Jy_{i,j-1}}{\Delta x} \end{aligned} \quad (3.33)$$

Region 7 pixel on the left down corner combines Equation (3.29) and Equation (3.30) for lower and left side pixels, respectively in Equation (3.34). Here, forward difference is applied both in x and y directions.

$$i = N, j = 1$$

$$\begin{aligned} & \frac{Jy}{\Delta x} R_{(i-1)N+j+1} - \frac{Jy}{\Delta x} R_{(i-1)N+j} - \frac{Jx}{\Delta y} R_{(i-2)N+j} + \frac{Jx}{\Delta y} R_{(i-1)N+j} \\ &= \frac{Jx_{i-1,j} - Jx_{i,j}}{\Delta y} - \frac{Jy_{i,j+1} - Jy_{i,j}}{\Delta x} \end{aligned} \quad (3.34)$$

Finally, right down pixel in region 9 is discretized with a combination of Equation (3.29) and Equation (3.31) for lower and right boundary pixels, respectively. In Equation (3.35), forward and backward differences are utilized in y and x directions, respectively.

$$i = N, j = N$$

$$\begin{aligned} & \frac{Jy}{\Delta x} R_{(i-1)N+j} - \frac{Jy}{\Delta x} R_{(i-1)N+j-1} - \frac{Jx}{\Delta y} R_{(i-2)N+j} + \frac{Jx}{\Delta y} R_{(i-1)N+j} \\ &= \frac{Jx_{i-1,j} - Jx_{i,j}}{\Delta y} - \frac{Jy_{i,j} - Jy_{i,j-1}}{\Delta x} \end{aligned} \quad (3.35)$$

After all pixels in 9 regions are discretized with Equation (3.27) to Equation (3.35), linear equation system represented in Equation (3.24) is constructed. Moreover, there is need for at least two current injection patterns to ensure reconstruction of true conductivity values. With the concatenation of linear equation systems for two current injection profiles, the following equation system is obtained.

$$\begin{bmatrix} C_1 \\ C_2 \end{bmatrix} R = \begin{bmatrix} B_1 \\ B_2 \end{bmatrix} \quad (3.36)$$

Rank of the linear equation system in Equation (3.36) is  $N^2 - 1$  which means that at least one pixel has to be assigned to its true logarithmic resistivity value. To satisfy that criteria, left corner pixel is assigned to its true logarithmic resistivity value.

The next step is to solve linear equation system. Preconditioned conjugate gradient method [29], which ensures fast convergence of the conjugate gradient method, is utilized to solve Equation (3.36). Preconditioned conjugate gradient method requires  $C$  being symmetric and positive-definite. To satisfy that criteria, both sides of Equation (3.36) are multiplied with the transpose of coefficient matrix  $C$  as in Equation (3.37).

$$\begin{bmatrix} C_1^T & C_2^T \end{bmatrix} \begin{bmatrix} C_1 \\ C_2 \end{bmatrix} R = \begin{bmatrix} C_1^T & C_2^T \end{bmatrix} \begin{bmatrix} B_1 \\ B_2 \end{bmatrix} \quad (3.37)$$

### 3.5 Reconstruction with Equipotential – Projection Algorithm

Equipotential-Projection algorithm is proposed by Eyüboğlu *et al*'s US Patent [23] and applied to real data by Özdemir [21]. Theory behind the algorithm and verification with real data experiments are explained in detail in [21]. Moreover, Lorca [22] extended the algorithm with slight modifications.

Equipotential-Projection algorithm reconstructs conductivity distribution,  $\sigma$ , with the help of current density distribution and surface potential measurements [21]. Measured surface potential measurements are projected inside FOV in the form of equipotential lines as explained earlier. Then, the potential distribution  $\phi$ , and its gradient  $\nabla\phi$ , inside FOV can be calculated. By making use of Ohm's law and measured current density distribution by MRCDI techniques, conductivity distribution,  $\sigma$ , is reconstructed.

$$\sigma = -\frac{\vec{J}}{\nabla\phi} \quad (3.38)$$

Basically, there are four steps for Equipotential-Projection algorithm which are,

- determination of surface potentials
- obtaining equipotential lines
- calculation of potential distribution and its gradient
- obtaining conductivity distribution

Implementation procedure in [21] and modifications done by Lorca [22] are explained explicitly in these subsections.

### **3.5.1 Determination of surface potentials**

Özdemir measured surface potentials of the experimental phantom at 18 points. Moreover, by interpolating between these measurements points, surface potential at four boundaries of the phantom are calculated. On the other hand, Lorca used another method for surface potential calculation. Assuming conductivity of a column or boundary of FOV is known, potential gradient on that column can be calculated with Equation (3.38). Then, potentials on that column can be found by integration of potential gradient. This modification reduces experimental difficulties.

### **3.5.2 Obtaining equipotential lines**

Equipotential lines are obtained as described in Section 3.2.1.1.

### **3.5.3 Calculation of potential distribution and its gradient**

After equipotential lines are projected inside FOV, potential distribution can be calculated. Since there can be more than one equipotential line in a pixel, the potential value in that pixel is a weighted average of the potential values of

equipotential lines intersecting that pixel. The weighting factor is the length of equipotential lines inside that pixel. If there are  $n$  equipotential crossing  $k^{th}$  pixel, the potential of that pixel,  $\phi_k$ , is

$$\phi_k = \frac{\sum_{i=1}^n l_i \phi_{eq_i}}{\sum_{i=1}^n l_i} \quad (3.39)$$

where  $l_i$  is the length of the  $i^{th}$  equipotential line inside and  $\phi_{eq_i}$  is its potential value.

If there are no equipotential lines through a pixel, its potential value is calculated by the averaging of its neighbor pixels' potential values.

Gradient of potential distribution,  $\nabla\phi$ , is calculated by Sobel operators.

### 3.5.4 Obtaining conductivity distribution

After gradient of potential distribution is calculated, Ohm's law in (3.38) is applied to every pixel in FOV to obtain conductivity distribution. Since true potential values of starting column for equipotential lines are used, reconstructed conductivity distribution does not need any scaling.

In the case of two current injection patterns, the final conductivity distribution is found by averaging of reconstructed conductivity distributions for the two current injection patterns. Moreover, if a conductivity value of a pixel can not be calculated for one of the patterns, the conductivity value found by the other pattern is assigned for the final distribution.

## 3.6 Reconstruction with J-substitution Algorithm

Kwon et al [20] proposed J-Substitution algorithm in 2002 which differs from other algorithms by using only magnitude of the current density inside FOV and being

iterative. The algorithm mainly tries to minimize a cost function defined as the difference between measured and calculated current density distributions at each step. It is explained explicitly in three sections which are problem and parameter definitions, reconstruction algorithm and implementation.

### 3.6.1 Problem and parameter definition

Let  $\Omega$  denote 2D cross section of a conductive body with boundary,  $\partial\Omega$ .  $\rho^*$  and  $V_p^*$  are resistivity and potential distribution when current  $I$  is applied from electrodes on the boundary.  $J^*$  is the current density magnitude which is measured by MRCDI techniques.  $j_l$  is the inward pointing normal component of current densities on the boundary which satisfies the compatibility condition in Equation (3.40).

$$\int_{\partial\Omega} j_l ds = 0 \quad (3.40)$$

For a given resistivity,  $\rho$ , the forward problem is defined as,

$$\nabla \cdot \left( \frac{1}{\rho} \nabla V_\rho \right) = 0 \quad \text{in } \Omega \quad (3.41)$$

and

$$\frac{1}{\rho} \frac{\partial V_\rho}{\partial n} = j_l \quad \text{on } \partial\Omega \quad (3.42)$$

where  $V_\rho$  and  $n$  are voltage distribution inside FOV and the unit outward normal vector at the boundary  $\partial\Omega$ , respectively.

If  $\rho$  is taken as  $\rho^*$ , the boundary problem in (3.41) and (3.42) becomes,

$$\nabla \cdot \left( \frac{\mathbf{J}^*}{|\nabla V_{\rho^*}|} \nabla V_{\rho^*} \right) = 0 \quad \text{in } \Omega \quad (3.43)$$

$$\frac{\mathbf{J}^*}{|\nabla V_{\rho^*}|} \frac{\partial V_{\rho^*}}{\partial n} = j_l \quad \text{on } \partial\Omega$$

where,  $1/\rho^*$  takes the form of  $\mathbf{J}^*/|\nabla V_{\rho^*}|$  through a modification of Ohm's law. The iterative J-Substitution algorithm reconstructs true resistivity distribution  $\rho^*$  from the highly nonlinear equation depicted in (3.43) where only  $\mathbf{J}^*$  is known.

### 3.6.2 Reconstruction algorithm

The cost function  $\Psi(\rho)$  expressed in Equation (3.44) is starting point for the reconstruction algorithm.

$$\Psi(\rho) := \int_{\Omega} \left| \mathbf{J}^*(\mathbf{r}) - \frac{1}{\rho(\mathbf{r})} \mathbf{E}_{\rho}(\mathbf{r}) \right|^2 d\mathbf{r} \quad (3.44)$$

where  $\mathbf{J}^*(\mathbf{r})$  is the magnitude of measured current density and  $\mathbf{E}_{\rho}(\mathbf{r})$  is the calculated electric field intensity when forward problem defined in (3.41) and (3.42) is solved with a given  $\rho$  value.

The formulation which leads to the following algorithm steps are explained in further detail in [20]. Moreover, Kwon [20] showed the need for at least two current injection patterns,  $I^1$  and  $I^2$ , satisfying the condition,

$$|\mathbf{J}^1 \times \mathbf{J}^2| \neq 0 \quad (3.45)$$

Here,  $\mathbf{J}^1$  and  $\mathbf{J}^2$  are the two current density distributions resulting from  $I^1$  and  $I^2$ . If condition in (6) is satisfied, at least one of  $\mathbf{J}^1$  and  $\mathbf{J}^2$  will change at the boundary of two media with different resistivity values. In other words, there will be sufficient information to reconstruct resistivity distribution.

J-Substitution algorithm which is used to reconstruct  $\rho^*$  from two pairs of current density data  $(I^q, J^q)$ ,  $q=1,2$  is the following.

- i. Initial guess: A homogeneous resistivity distribution  $\rho^0$  is chosen.
- ii. Forward problem solution: With the given resistivity  $\rho^{2p+q}$  ( $q=1,2$  and  $p=0,1,2,\dots$ ) where  $p$  is the iteration number, forward problem expressed in Equation (3.46) is solved.

$$\nabla \cdot \left( \frac{1}{\rho^{2p+q}} \nabla V_p^q \right) = 0 \quad \text{in } \Omega \quad (3.46)$$

$$\frac{1}{\rho^{2p+q}} \frac{\partial V_p^q}{\partial n} = j_{I^q} \quad \text{on } \partial\Omega \quad \text{and} \quad \int_{\partial\Omega} V_p^q ds = 0$$

Among many numerical methods, finite element method (FEM) [18] is used to calculate potential distribution and electric field intensity in (3.46).

- iii. Update equation: Resistivity distribution to be used for forward problem solution in the next iteration is calculated.

$$\rho^{2p+q+1} := \frac{|\nabla V_p^q|}{J^q} \quad (3.47)$$

Consider the case of two resistivity distributions,  $\rho$  and  $\alpha\rho$ . The current density distributions for two resistivity distributions are the same, whereas, one of the potential distributions for the case of  $\alpha\rho$  is scaled to  $\alpha V$  when  $V$  is the potential distribution for the case of  $\rho$ . To overcome this uniqueness problem, update equation is modified as,

$$\rho^{2p+q+1} := \frac{|\nabla V_p^q|}{J^q} \frac{f_{\rho^*}^q}{f_{\rho^{2p+q}}^q} \quad (3.48)$$

where  $f_{\rho^{2p+q}}^q$  is the voltage difference between two current injection electrodes and  $f_{\rho^*}^q$  is the measured voltage difference for the same current injection pattern.

- iv. Stopping criteria check: To stop the algorithm, a precision difference  $\varepsilon$  between two successive steps of the algorithm is employed.

$$\left| \rho^{2p+q+1} - \rho^{2p+q} \right| < \varepsilon \quad (3.49)$$

If the condition in (3.49) is satisfied, the algorithm stops. Otherwise, the algorithm returns to step (ii) with  $q = q + 1$  when  $q = 1$ , or  $p = p + 1$  and  $q = 1$  when  $q = 2$ .

### 3.7 J-Substitution and Filtered Equipotential-Projection Based Hybrid Reconstruction Algorithm

In this thesis, a new MREIT reconstruction algorithm is proposed, J-Substitution and Filtered Equipotential-Projection Based Hybrid Reconstruction Algorithm. In this section, the steps leading to the hybrid algorithm and implementation of the algorithm are explained.

J-substitution algorithm [20] as explained in Section 3.6 reconstructs conductivity distribution with a better image contrast and percentage error with respect to other MREIT reconstruction algorithms. However, J-substitution algorithm has the worst performance in image reconstruction time since it is iterative and solves forward problem in each iteration. On the other hand, Equipotential-Projection algorithm [21] is one of the fastest algorithms. Equipotential-Projection algorithm has a poorer performance in percentage error. Another important point about J-Substitution algorithm is that it converges to the solution with a smart choice of starting conductivity [20].

Considering these properties of J-Substitution and Equipotential-Projection algorithm, the hybrid algorithm is proposed as the following.

- Conductivity distribution is reconstructed with Equipotential-Projection algorithm.
- A low-pass filter is applied to the reconstructed image to smooth errors in the background.

- Filtered conductivity distribution is assigned as the initial conductivity distribution for J-Substitution algorithm.
- J-Substitution algorithm is used to reconstruct true conductivity distribution.

Low-pass filter is employed before assigning the initial conductivity of J-Substitution algorithm to reduce the effect errors in the background.

## CHAPTER 4

### SIMULATION AND COMPARISON

#### 4.1 Introduction

In this chapter, simulation results for MREIT reconstruction algorithms described in CHAPTER 3 will be given. Five different simulation models are used in simulation study. Each model has a different purpose which will be explained in further detail. Moreover, according to the results of these simulations, reconstructions algorithms are compared with 6 different criteria. These are reconstruction time, electrode size, number of potential measurements and current injection patterns, noise performance, percentage error, and reconstructed image quality. All of these criteria are important in terms of readiness for clinical use.

#### 4.2 Simulation Phantoms

In experimental study, 0.15 T METU MRI system is used to collect data. To measure magnetic flux density perturbations created by currents applied, a new RF coil is designed. Hence, experimental phantom size is restricted by the size of RF coil and METU MRI system. It is designed as the biggest phantom, with size of 9cm x 9cm, that fits into the RF coil. Simulation phantom sizes are chosen the same as the experimental phantom for consistency.

Another important parameter is the resolution or pixel size. Restriction for pixel size comes from the resolution of METU MRI system. Since the resolution is 2 mm, phantoms are discretized into 40x40 square pixels.

Different current levels are used in simulation and experimental studies of MREIT. Birgül [30] and Özbek [31] used 20 mA for data collection with METU MRI system. Ider [19] applied 100 mA for simulation. In this thesis, 20 mA is used for

experimental purposes. Considering all of these studies and to be consistent with experimental study, 20 mA is chosen as the magnitude of current injection for the following simulations.

Electrode size which is one of the performance criteria is chosen to be 1.8 cm, 1/5 of the phantom side length. Moreover, electrodes are placed in the middle of phantom sides. However, some algorithms are simulated with boundary electrodes which cover a whole side of the phantom because these algorithms are originally designed for boundary electrodes and they turned out to have poor performances with small electrodes.

For most of the reconstruction algorithms, two current injection patterns are applied. For this reason, 4 electrodes are placed in the middle of each side of simulation phantoms. The first current injection, horizontal pattern, is formed by applying current from the left side electrode and collecting from right side. In the vertical pattern, current is applied from upside electrode and collected from downside electrode. As a result, two current injection patterns are orthogonal satisfying the condition in Equation (3.45).

In the following section, simulation phantoms designed will be described with their purposes, geometry and conductivity values.

#### **4.2.1 Simulation model 1**

The first simulation model, whose geometry with 4 electrodes is shown in Figure 4.1, is designed to compare overall performance of reconstruction algorithms. Moreover, this phantom is implemented for experimental study which enables to check the results of simulation study against real data experiments.

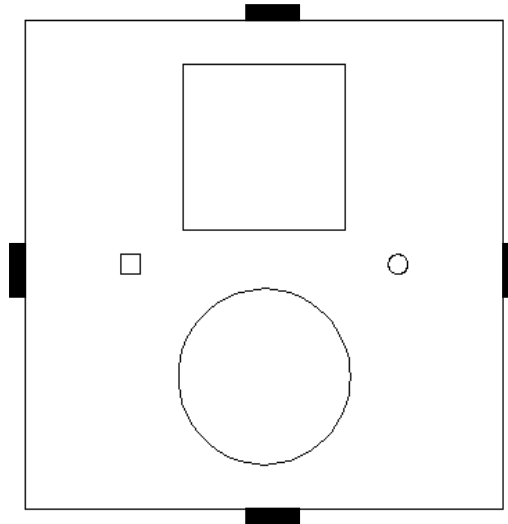


Figure 4.1 Geometry of Simulation Model 1

Background of the phantom is set to 0.2 S/m, whereas the big square has a conductivity of 0.1 S/m and the big circle is slightly more conductive than background with a conductivity of 0.4 S/m. The small elements serve for impulsive response of reconstruction algorithms since they have 2 S/m conductivity for the square and 0.02 S/m for the circle element.

#### 4.2.2 Simulation model 2

This model has two impulsive elements at the centre of the phantom. 10 simulations, where these two elements will get far from each other, will be performed. As a result, Full Width at Half Maximum (FWHM) values with respect to position will be plotted. This analysis enables to see the spatial resolution of each reconstruction algorithm.

There will be two cases for this simulation model, a more and a less conductive case. To have an impulsive effect for the more conductive case, small elements have a conductivity of 2 S/m with a background of 0.2 S/m. On the other hand, less conductive case includes 0.02 S/m conductivity for small elements and again 0.2 S/m conductivity for the background.

In Figure 4.2 and Figure 4.3, the starting and end positions for these two elements, when they are separated from each other at each simulation step, can be seen.

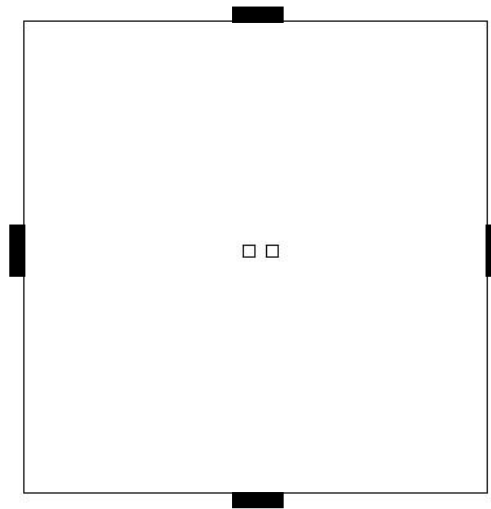


Figure 4.2 Starting position for impulsive elements in Simulation Model 2

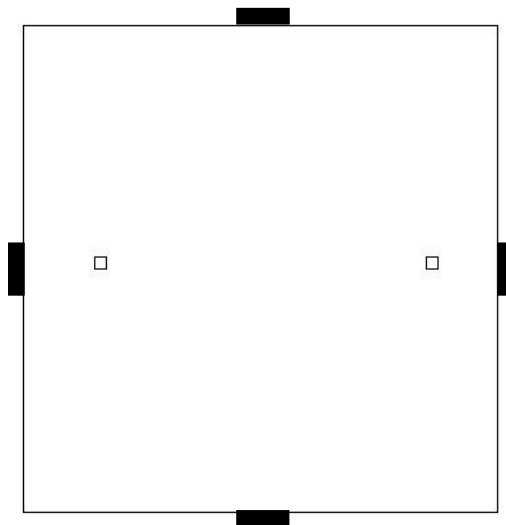


Figure 4.3 End position for impulsive elements in Simulation Model 2

### 4.2.3 Simulation Model 3

Simulations with model 3 are carried out to see the position dependency of reconstruction algorithms. There are 9 impulsive elements distributed from left-up corner to right-bottom corner as in Figure 4.4. Two cases with resistive and

conductive elements are investigated. For the resistive case, small elements are assigned with 0.02 S/m conductive. Simulation for conductive case has 2 S/m conductivity for small elements. In both cases, background is set to 0.2 S/m conductivity.

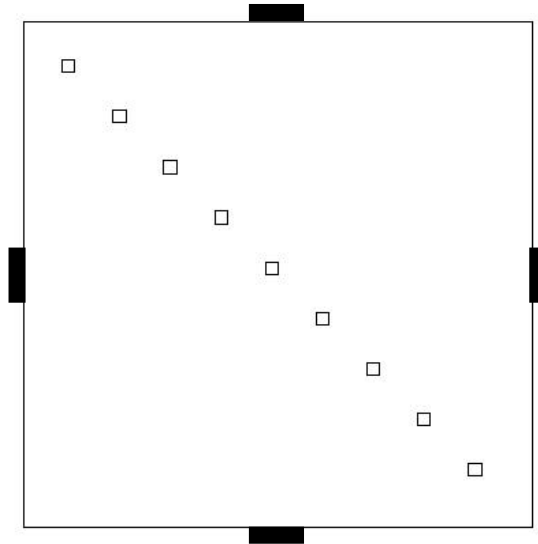


Figure 4.4 Geometry of Simulation Model 3

#### 4.2.4 Simulation model 4

This model is designed to see the numerical accuracy of reconstruction algorithms with changing conductivity contrast. Geometry of the model is rather simple with a square, which has side length of 2.2 cm, in the middle of the phantom as can be seen in Figure 4.5.

For each reconstruction algorithm, 10 simulations will be carried out. In each simulation, the conductivity contrast will change. The conductivity contrast between the background and the square will increase from 1 to 10 for the conductive case, whereas the contrast will decrease from 1 to 0.1 for the resistive case. As a result, a plot illustrating the change of average reconstructed conductivity value of the square with respect to its true conductivity value will be constructed.

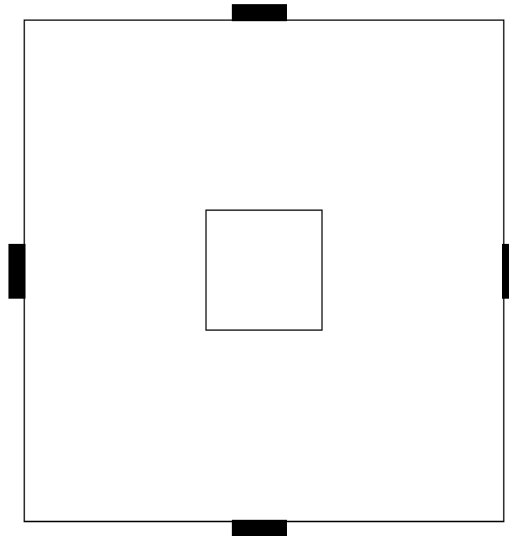


Figure 4.5 Geometry of Simulation Model 4

#### **4.2.5 Thorax phantom**

The last phantom developed is a thorax phantom which is the most complex. It is designed with true tissue conductivity values. The basic idea behind the thorax phantom is comparing reconstruction algorithms with a more complex phantom. Moreover, simulation results of the thorax phantom will give a valuable perspective of performance of reconstruction algorithms before carrying out experiments with real tissue or animals.

Many studies on measuring true tissue conductivity values [32], [33] and thorax images are investigated before deciding on the geometry and conductivity value of each element within the thorax phantom. Although, there are many inconsistent measurement values in these studies, common results are chosen to be consistent. Geometry and conductivity values are illustrated in Figure 4.6 and Table 4.1, respectively.

Thorax is one of the most complex parts of the body which includes many different organs with a variety of geometry and conductivity values. Also, there is big contrast between the conductivity values of elements in the thorax phantom. As can be seen in Figure 4.6, spinal cord inside the spine will serve for the ability of algorithms to

reconstruct the areas with relatively low current density since a small proportion of injected current will go through the bone.

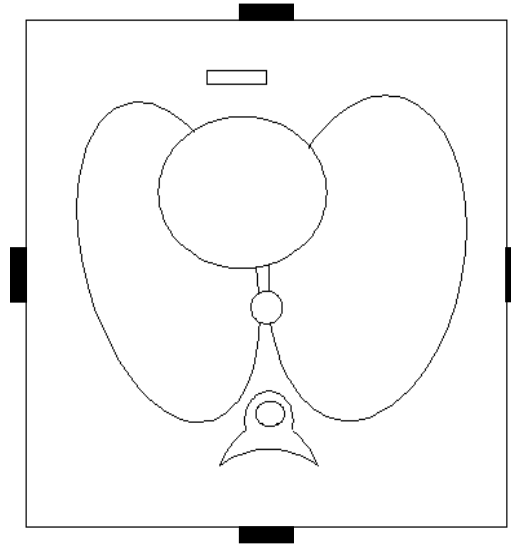


Figure 4.6 Geometry of Thorax Phantom

Region 1, background in Figure 4.6, corresponds to skeletal muscle with a conductivity value of 0.2 S/m. Two ellipses in the middle of the phantom, region 2, are designed to be lungs which have 0.0667 S/m conductivity. Region 3 is simulating the heart with a conductivity of 0.6667 S/m. Region 4 elements have the conductivity of bone which are sternum on the upper side and the spine below the lungs. Sternum will enable to see the ability of current to pass through a region with a relatively high resistivity. Spinal cord with the resistivity of CSF (cerebrospinal fluid) is forming region 5 and its conductivity value is 1.5625 S/m. In the end, region 6 is designed to be aorta with the same conductivity of heart. All these values are listed in Table 4.1.

Table 4.1 Conductivity Values of Thorax Phantom

Region	Tissue type	Conductivity (S/m)
1	Skeletal muscle	0.2
2	Lung	0.0667
3	Heart	0.6667
4	Bone	0.006
5	Spinal cord (CSF)	1.5625
6	Aorta	0.6667

#### 4.2.6 Experimental phantom

Throughout the thesis work, an experimental phantom is designed and constructed. There are many experimental MREIT studies in the literature. One of the most important results of previous studies is the need for recessed electrodes to eliminate the effect of relatively high current density near the electrodes [34]. So, recessed electrodes are chosen for experimental phantom.

Experimental phantom has another important feature. It is designed to serve both for 2D and 3D experiments. Moreover, its geometry and size is restricted to the size and shape of RF coil used in METU MRI System. Design of the experimental phantom is carried out with CAD simulations. After the simulations and design, its fabrication is done by a private company. For the fabrication of the experimental phantom plexiglas material is used.

To satisfy the exact position in RF coil when experimental phantom is rotated, a table mechanism is also designed. Small legs on the experimental phantom fit exactly to the holes in the table, so imaging from the same slice is ensured when the experimental phantom is rotated. Two oblique CAD views of the experimental phantom together with the table can be seen in Figure 4.7

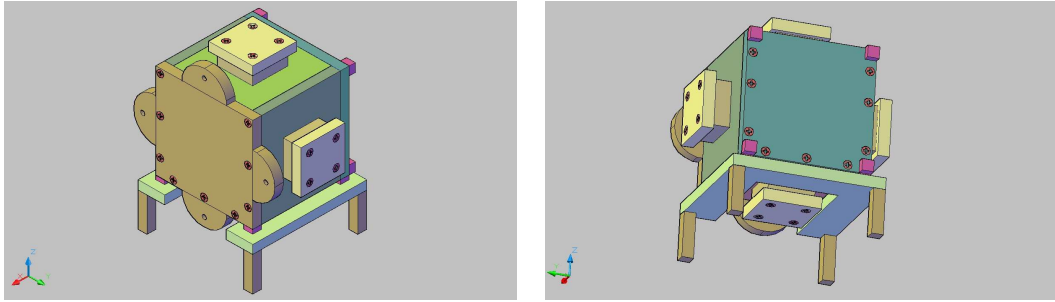


Figure 4.7 Two Oblique Views of CAD Simulations of Experimental Phantom

As can be seen from Figure 4.7 experimental phantom is basically a cube and two sides of the phantom do not have electrodes. Actually, that is the setup for 2D imaging with two current injection profiles. However, these sides can be taken out replaced with other sides which have electrodes attached onto them. As a result, the experimental phantom will turn into a 3D phantom with three current injection profiles.

Geometry and original conductivity distribution of experimental phantom 1 are shown in Figure 4.8 and Figure 4.9. Two experiments are conducted as for the first experiment, square and circle elements have 0.1 and 0.4 S/m conductivity values whereas background is set to 0.2 S/m. On the other hand, second experiment includes square, circle and background elements with zero, 1,9 and 0.2 S/m conductivity. Phantom elements are made with agar, TX151 and TX150 materials [35]. Every element has a different combination of these thickening materials.

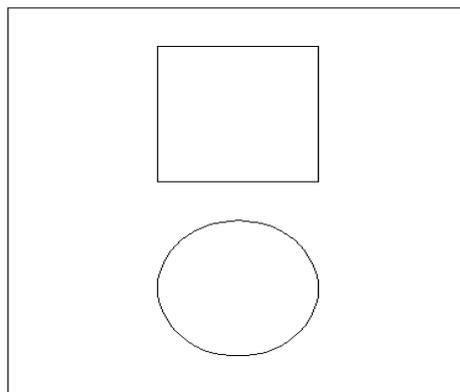


Figure 4.8 Geometry of Experimental Phantom

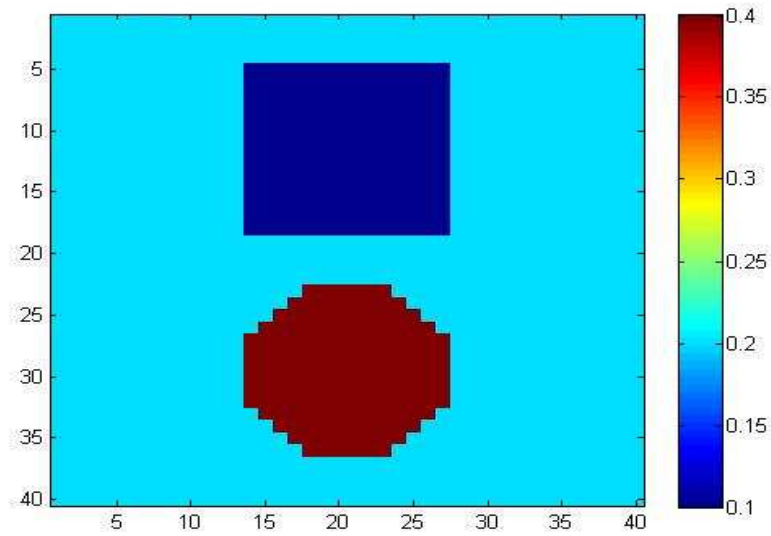


Figure 4.9 Original Conductivity Distribution of Experimental Phantom

### 4.3 Simulation of Measurement Noise

Simulations of reconstruction algorithms with simulation phantom 1 and complex thorax phantom are also carried out with noisy data. These phantoms are chosen for simulations in the presence of noise because they have rather complex geometries and can be used for numerical analysis in different regions of FOV.

For noise simulation, random Gaussian noise model proposed by Scott *et al* [13] is used. In their model, added noise is independent from applied currents and magnetic flux density. It only depends on SNR of MRI system where magnetic flux density due to injection currents is measured.

According to this noise model, first magnetic flux densities due to injection currents are calculated. Then, a random Gaussian noise is added to magnetic flux density based on SNR of the MRI system. With new magnetic flux density, noisy current density is calculated. A detailed formulation can be found in [22] and [36].

Two noise levels are used for simulations in this thesis. First noise level is SNR 30 and the other one is SNR 13 which is actually the SNR of METU MRI system [36].

Same noisy data is used for all algorithms to assure consistency. However, some algorithms which are more vulnerable to noise could not reconstruct conductivity distribution with noisy current density. Because random noise addition changed current density values dramatically in some regions especially where initial current density is relatively low. So, after addition of noise, these algorithms are tried first. When they were successful in reconstructing conductivity, the other algorithms are fed with the same noisy current density.

#### 4.4 Error Calculation and Stopping Criteria

Error calculation is also carried out for numerical analysis and performance comparison of reconstruction algorithms. For error calculation, true values of conductivity are necessary which are already available with simulation data.

General error  $\varepsilon_{\sigma}$  for the whole image is calculated as,

$$\varepsilon_{\sigma} = \sqrt{\frac{1}{N} \sum_{i=1}^N \frac{(\sigma_{ir} - \sigma_{ic})^2}{\sigma_{ir}^2}} \times 100 \quad (4.1)$$

where  $N$ ,  $\sigma_{ir}$  and  $\sigma_{ic}$  are pixel number, real and calculated conductivity values, respectively.

Regional errors  $\varepsilon_{\sigma,rg}$  are also calculated based on Equation (4.1) to determine position dependency of errors.

$$\varepsilon_{\sigma,rg} = \sqrt{\frac{1}{M} \sum_{i=1}^M \frac{(\sigma_{ir,rg} - \sigma_{ic,rg})^2}{\sigma_{ir,rg}^2}} \times 100 \quad (4.2)$$

where  $M$ ,  $\sigma_{ir,rg}$  and  $\sigma_{ic,rg}$  are pixel number of that specific region, real and calculated conductivity values, respectively.

Stopping criterion of iterative algorithms is studied in detail in [22]. Lorca stated that J-Substitution algorithm converged to a minimum error result after 5 iterations. The

same phenomenon is also encountered in this thesis study. Iterative algorithms, J-Substitution and Hybrid algorithm, reconstructed conductivity distribution with minimum error after 3 iterations and remained with that percentage errors in the following iterations. Perceptually, reconstructed images are not changed much after 3 iterations. Therefore, all results for J-substitution and Hybrid algorithm are obtained with 3 iterations.

## **4.5 Simulation Results for Current Density Based Algorithms**

In the following sections, results of simulations for the reconstruction algorithms are given and reconstruction algorithms' performances are compared with respect to different criteria.

### **4.5.1 Simulation Results for Model 1**

This section includes results obtained with simulation model 1. Model 1, whose conductivity distribution is shown in Figure 4.10a, is designed to see overall effect and noise performance of reconstruction algorithms. It includes a big square with conductivity set to 0.1 S/m and a big circle with 0.4 S/m conductivity. Moreover, there are two small elements to illustrate impulsive response. Small square on the left has 2 S/m conductivity and small circle is set to 0.02 S/m conductivity. However, small circle on the left appears to be a square when it is discretized. Background conductivity is 0.2 S/m.

There are two noise levels employed in simulations, SNR 30 and SNR 13. Errors are added with the procedure explained in Section 4.3. Errors added to the current density data are independent from current density values in each pixel, so pixels with relatively low current density are more affected by noise. Performance of reconstruction algorithm regarding this phenomenon is an important criterion. SNR 13 is chosen for noise simulation since it is the noise level of METU MRI system.

In Figure 4.10, results obtained with simulation of reconstruction algorithms for noise-free case are shown. Moreover, reconstructed conductivity distributions with noise

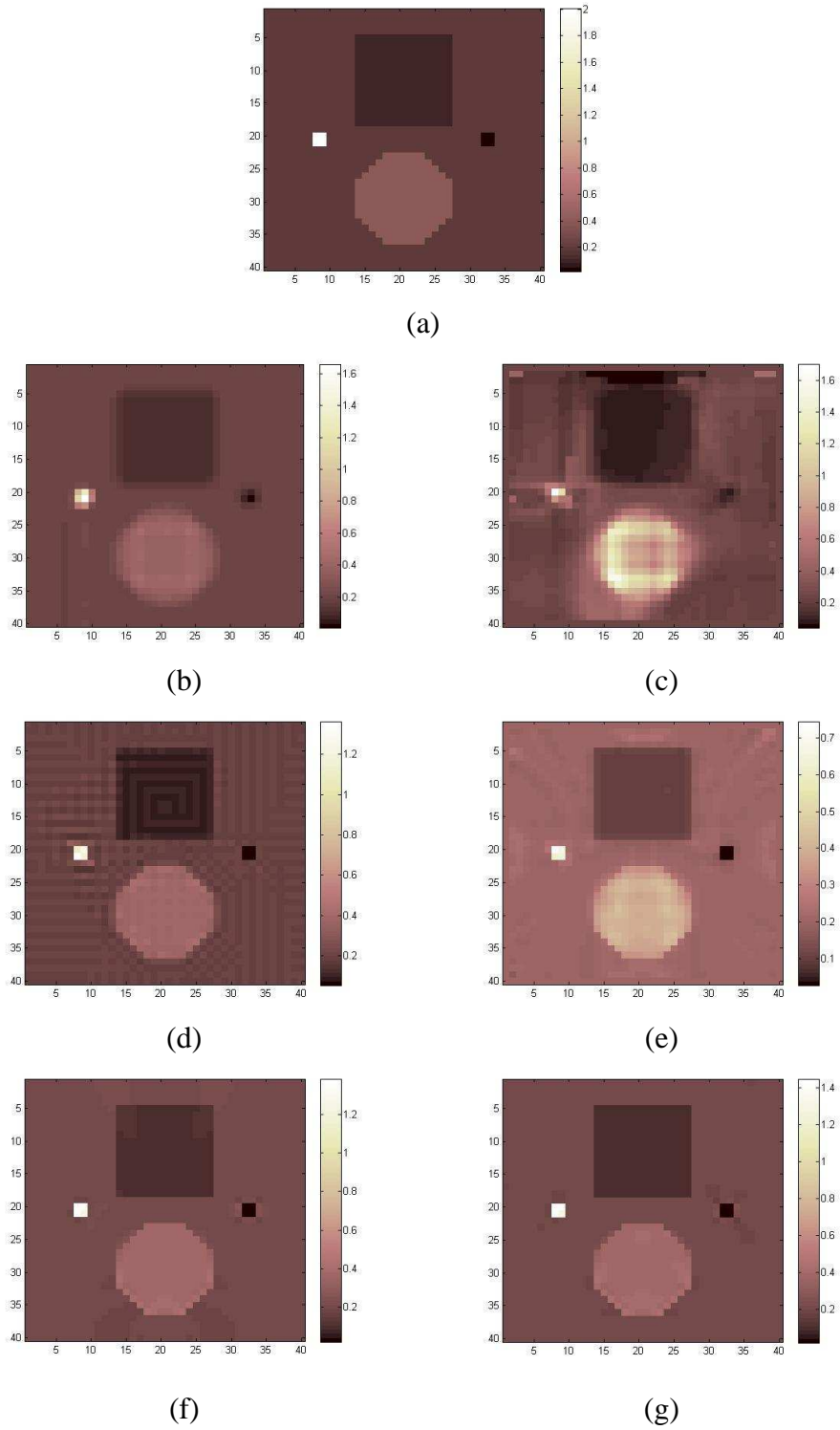


Figure 4.10 Reconstruction Results for Noise-free case a) Original distribution, b) Integration along Cartesian grid lines, c) Integration along equipotential lines, d) Solution as a linear equation system, e) equipotential projection, f) j-substitution, g) hybrid

levels of SNR 30 and SNR 13 are illustrated in Figure 4.11 and Figure 4.12, respectively.

Although reconstructed images give a perceptual idea on performance of reconstruction algorithms, percentage errors of all elements and total errors are listed in Table 4.2. So, numerical analysis of each algorithm with its noisy simulations and other algorithms is possible. Artifacts in reconstructed images and the reasons behind them are explained explicitly for each algorithm.

Ider [19] only used equipotential lines originated from the left boundary for simulation of Integration along Equipotential Lines algorithm. But, in this thesis conductivity distribution is reconstructed for four times with equipotential lines started from left, right, top and bottom boundary columns. At the end, their average is taken to find final conductivity distribution. It is important to state that it is impossible to use all equipotential lines originated from four boundaries in a single step. Because, algorithm is started from pixels which are at the end of equipotential lines and it is a recursive algorithm. Integration along Equipotential Lines algorithm mainly produces errors at element boundaries since it uses integration of current density derivatives. Nevertheless, averaging of four reconstructed conductivity distributions reduces percentage error dramatically because errors distributed from an element boundary or corner is not seen in other three reconstructed images.

Another drawback of Integration along Equipotential Lines algorithm is that pixels which do not contain any equipotential lines can not be reconstructed since there is no information that can be used to reconstruct them. Nevertheless, conductivity values of these pixels can be reconstructed with equipotential lines originated from other boundaries. When averaging is done, only reconstructed values are taken into account. For example, if a pixel's conductivity value is reconstructed with equipotential lines originated from right and top boundary, its value is found by averaging these two values.

Some equipotential lines come across to pixel corners and are terminated at that point. These equipotential lines are finished at that point. Moreover, some

equipotential lines turn back to their starting boundary which may result in crashing of the algorithm due to its recursive nature. These equipotential lines are also eliminated for the sake of algorithm.

This algorithm has a total error of 64% whereas it is more successful in reconstructing resistive elements. Big square and square elements have relatively less error than circle elements.

Next analysis of Integration along Equipotential Lines algorithm is its performance with noisy current density data. As can be seen in Figure 4.11 and Figure 4.12, the worst performance with noisy data comes from Integration along Equipotential Lines algorithm. Although SNR 30 is not considered as a significant noise level, Integration along Equipotential Lines algorithm has a total reconstruction error of 230%. Two big elements are still separated from background but boundaries of these elements are not clear with respect to noise-free case. The main reason behind is that equipotential lines can not cover whole FOV and some points are only reconstructed with equipotential lines originated from a single boundary. This is clearer with SNR 13 noise level. Integration along Equipotential Lines algorithm can not reconstruct conductivity distribution properly. Actually, any of the elements can not be distinguished from background and only a small portion of the FOV is reconstructed. Due to this reason, errors for SNR 13 are not listed in Table 4.2. Integration along Cartesian Grid Lines algorithm is also employing integration to reconstruct conductivity distribution as Integration along Equipotential Lines algorithms. But its advantage is that it uses information of two current injection patterns in a single step. Logarithmic resistivity derivatives are calculated for each pixel with the help of current density data from two current injection patterns and these derivatives are integrated over FOV with the assumption that a logarithmic resistivity of a single pixel is known. In this thesis, it is assumed that upper left corner pixel's resistivity value is known. Moreover, an averaging is done to reduce artifacts and errors due to integration. Assuming upper left corner pixel value is known, pixels on the top boundary are calculated and these pixels are used as initial values for integration downwards. Another integration strategy is first calculating pixels on the left

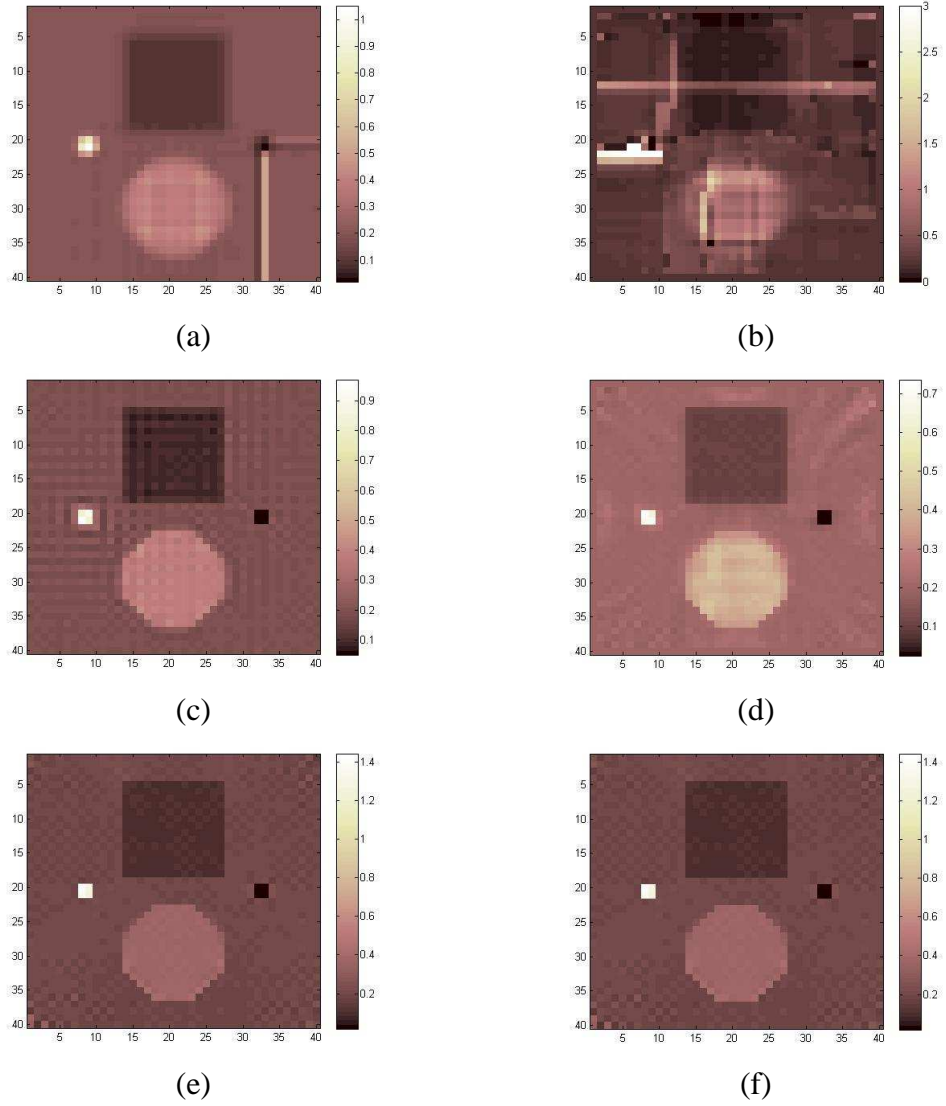


Figure 4.11 Reconstruction Results for SNR 30 a) Integration along Cartesian grid lines, b) Integration along equipotential lines, c) Solution as a linear equation system, d) Equipotential-Projection, e) J-Substitution, f) Hybrid

boundary and then reconstructing pixels to the right. In the end, two reconstructed logarithmic resistivity values are averaged.

Although Integration along Cartesian Grid Lines algorithm can not reconstruct element boundaries as sharp as other algorithms, boundaries are still definite. This result is also proved with relatively small errors for big square and circle. Percentage errors of small elements are not an important criterion since they have extreme conductivity values and consist of only four pixels. Nevertheless, it fails in reconstructing impulsive elements with their true values.

Big square and circle elements have percentage error around 10% and addition of noise does not affect reconstruction of these elements. Dramatic increase in total error is mainly caused by background error which is due to integration artifact moving to the right and down boundary and caused by small circle on the left. True conductivity value of small circle is 0.02 S/m and forces current to flow outside of itself. So, added noise affects small circle more than other areas since noise is independent from current density amplitude. As a result, errors created in the small circle propagate with integration to the right and downwards. This phenomenon can be seen in simulations with SNR 30 and SNR 13 but it is more obvious with SNR 13. Moreover, error lines originated from big square start to distort the image with SNR 13.

In conclusion, Integration along Cartesian Grid Lines algorithm can reconstruct elements with definite boundaries and relatively small percentage errors. However, addition of noise may result in miscalculated pixels due to errors introduced by relatively more resistive areas.

Solution as a Linear Equation System algorithm also uses information from two current injection patterns and does not include integration which results in a superior performance over Integration along Equipotential Lines and Integration along Cartesian Grid Lines algorithms. It states the relation between logarithmic resistivity and current density data as a linear equation system with the help of finite differences and solves this linear equation system to reconstruct conductivity distribution.

Since Lorca [22] stated that four neighbor pixels are used for each pixel discretization, there appears an artifact in the form of a grid shape. However, boundaries of elements are definite. If errors for impulsive elements are ignored, there is 7.48% error for the background and 12.69% total error. Moreover, simulation with SNR 30 noise level produced 7.65% and 12.59% error for background and in total, respectively. However, SNR 13 forced total error to be 18.5%. Perceptually, grid artifact becomes more obvious with increasing noise.

Therefore, Solution as a Linear Equation System algorithm is robust to noise and reconstructs all elements with sharp contours but has a grid effect on reconstructed images which grows with low SNR.

Next algorithm to be investigated is Equipotential-Projection algorithm. It makes use of equipotential lines as Integration along Equipotential Lines algorithm with the difference that it uses equipotential lines originated from 4 boundaries together. So, artifacts and errors introduced by elimination of equipotential lines are not encountered with Equipotential-Projection algorithm.

Object boundaries are sharper and errors are smaller than algorithms explained above for noise-free, SNR 30 and SNR 13 cases. Moreover, elements are homogenous leading to around 6% and 9% error for big square and circle elements even with SNR 13. The main artifact is due to erroneous lines starting from corners of FOV and propagates into background which becomes obvious with SNR 13 simulation. These artifacts force Equipotential-Projection algorithm to have 16.79% error for background with SNR 13 which is bigger than 14.33% error value of Solution as a Linear Equation System but thanks to relatively small errors in big square and circle element, total error of 15.69% is still below 18.5% total error of Solution as a Linear Equation System.

As a result, Equipotential-Projection algorithm reconstructs conductivity distribution with sharp boundaries but have erroneous lines starting from corners and distorting reconstructed image with increasing noise level.

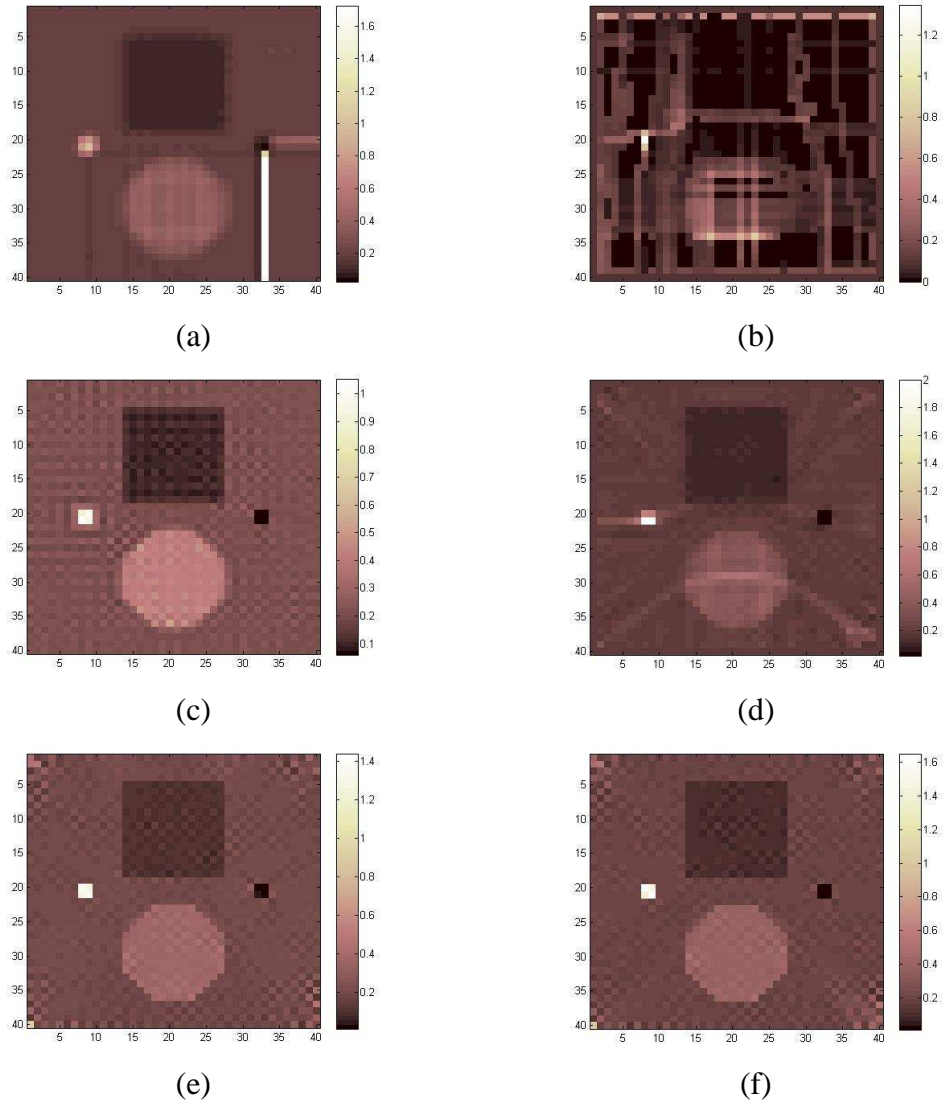


Figure 4.12 Reconstruction Results for SNR 13 a) Integration along Cartesian grid lines, b) Integration along equipotential lines, c) Solution as a linear equation system, d) Equipotential-Projection, e) J-Substitution, f) Hybrid

J-Substitution algorithm is an iterative algorithm and solves forward problem at all iterations which results in relatively longer solution times. The result of third iteration is chosen for the results since it produced the smallest errors for all elements. Nevertheless, it took eight minutes of reconstruction time for three iterations whereas algorithms explained above have reconstruction times shorter than 10 seconds.

Perceptually, J-Substitution algorithm along with Hybrid algorithm produced sharper contours and better reconstructed images than all other algorithms. For noise-free case its performance is better than Equipotential-Projection algorithms but worse than Hybrid algorithm with 3.89% and 4.58% errors for background and in total, respectively. Addition of noise with SNR 30 mainly affected background conductivity and forced total error to be 8.17%. This effect is clearer when noise level is set to SNR 13 which can be seen in Figure 4.12e. It is important to state that for simulation of J-Substitution algorithm small electrodes are used which result in relatively low current densities in corners. When noise is added these areas are affected more than other areas. So, error increase in background dominates total error.

Hybrid algorithm differs from J-Substitution algorithm only in selection of initial conductivity distribution. J-Substitution algorithm is initiated with a homogenous conductivity distribution of 0.2 S/m which actually is background conductivity whereas Hybrid algorithm uses filtered conductivity distribution obtained with Equipotential-Projection. Hybrid algorithm has smallest errors for all elements except small circle for noise free case. Application of Hybrid algorithm to the result of Equipotential-Projection algorithm can be seen as an optimization of both percentage error and homogeneity of each element.

With SNR 30, homogeneity of elements start to decrease but errors are still in the range of Equipotential-Projection algorithm and better than J-Substitution algorithm. When noise level is increased SNR 13, erroneous current density data and artifacts of Equipotential-Projection start to increase errors for background and in total.

Nevertheless, all elements are still homogenous and Hybrid algorithm manages to correct erroneous lines of Equipotential-Projection algorithm.

As a result, Hybrid algorithm produced the lowest errors for noise free case, but with increasing noise level erroneous lines of Equipotential-Projection algorithm and noisy current data are added up to distort image and increase errors.

Table 4.2 General and Regional Percentage Errors for Simulations with Model 1

	<b>Square (%)</b>	<b>Circle (%)</b>	<b>Small Square (%)</b>	<b>Small Circle (%)</b>	<b>Background (%)</b>	<b>Total (%)</b>
<b>Integration along Cartesian Grid Lines</b>						
<b>Noise-free</b>	13.68	10.18	41.25	331.56	13.41	21.25
<b>SNR 30</b>	14.18	10.43	58.94	335.20	22.56	26.82
<b>SNR 13</b>	13.61	11.98	60.68	351.21	92.13	83.26
<b>Integration along Equipotential Lines</b>						
<b>Noise-free</b>	19.49	140.47	51.76	430.80	46.50	64.16
<b>SNR 30</b>	131.57	147.08	78.74	572.28	252.39	233.31
<b>SNR 13</b>	-	-	-	-	-	-
<b>Solution as a Linear Equation System</b>						
<b>Noise-free</b>	11.63	5.14	38.69	194.65	7.48	12.69
<b>SNR 30</b>	12.53	6.13	55.96	181.52	7.65	12.59
<b>SNR 13</b>	17.14	8.40	51.10	231.45	14.33	18.50
<b>Equipotential-Projection</b>						
<b>Noise-free</b>	5.74	8.39	66.53	38.84	5.26	6.87
<b>SNR 30</b>	6.07	8.48	65.59	39.22	6.51	7.68
<b>SNR 13</b>	6.19	9.47	67.88	33.48	16.79	15.69
<b>J-Substitution</b>						
<b>Noise-free</b>	3.02	7.33	33.24	6.46	3.89	4.58
<b>SNR 30</b>	6.78	7.71	33.36	10.60	8.21	8.17
<b>SNR 13</b>	14.84	9.07	33.26	46.96	19.17	18.11
<b>Hybrid</b>						
<b>Noise-free</b>	0.67	3.41	30.51	9.65	2.67	3.04
<b>SNR 30</b>	5.99	4.29	30.61	9.43	8.06	7.69
<b>SNR 13</b>	13.99	6.70	23.83	48.72	20.84	19.29

## **4.5.2 Simulation Results for Model 2**

### **4.5.2.1 Full Width at Half Maximum and Spatial Resolution Analysis**

In this section, all algorithms are simulated with simulation model 2 to compare their performance with respect to their spatial resolution. In many imaging studies, spatial resolution of a system is measured with Full Width at Half Maximum (FWHM) of a Point Spread Function (PSF) [37].

As discussed in Section 4.2.2, there are two impulsive elements in the middle of simulation model 2 which will serve as a PSF. There are two cases employed, conductive and resistive case. In the conductive case, impulsive elements have conductivity value of 2 S/m whereas 0.02 S/m is assigned as the conductivity value of impulsive elements in the resistive case. For both cases, background conductivity is 0.2 S/m.

10 simulations are carried out for each reconstruction algorithm and each case. In the first simulation, two impulsive elements are closest to each other. There is only one pixel assigned with the background conductivity separating the two impulsive elements. Then, at each simulation, the two impulsive elements are separated from each other. In the last simulation, the two impulsive elements are closest to the boundaries.

### **4.5.2.2 Conductive case**

In the conductive case, the cross-section of reconstructed images at the line where the two impulsive elements are positioned is investigated. In the ideal case, FWHM is expected to be equal to length of a single pixel which is 0.225 cm for the first case. Original conductivity distribution and its image profile are illustrated in Figure 4.13. Moreover, cross-section plots of reconstructed images with all algorithms are shown in Figure 4.13.

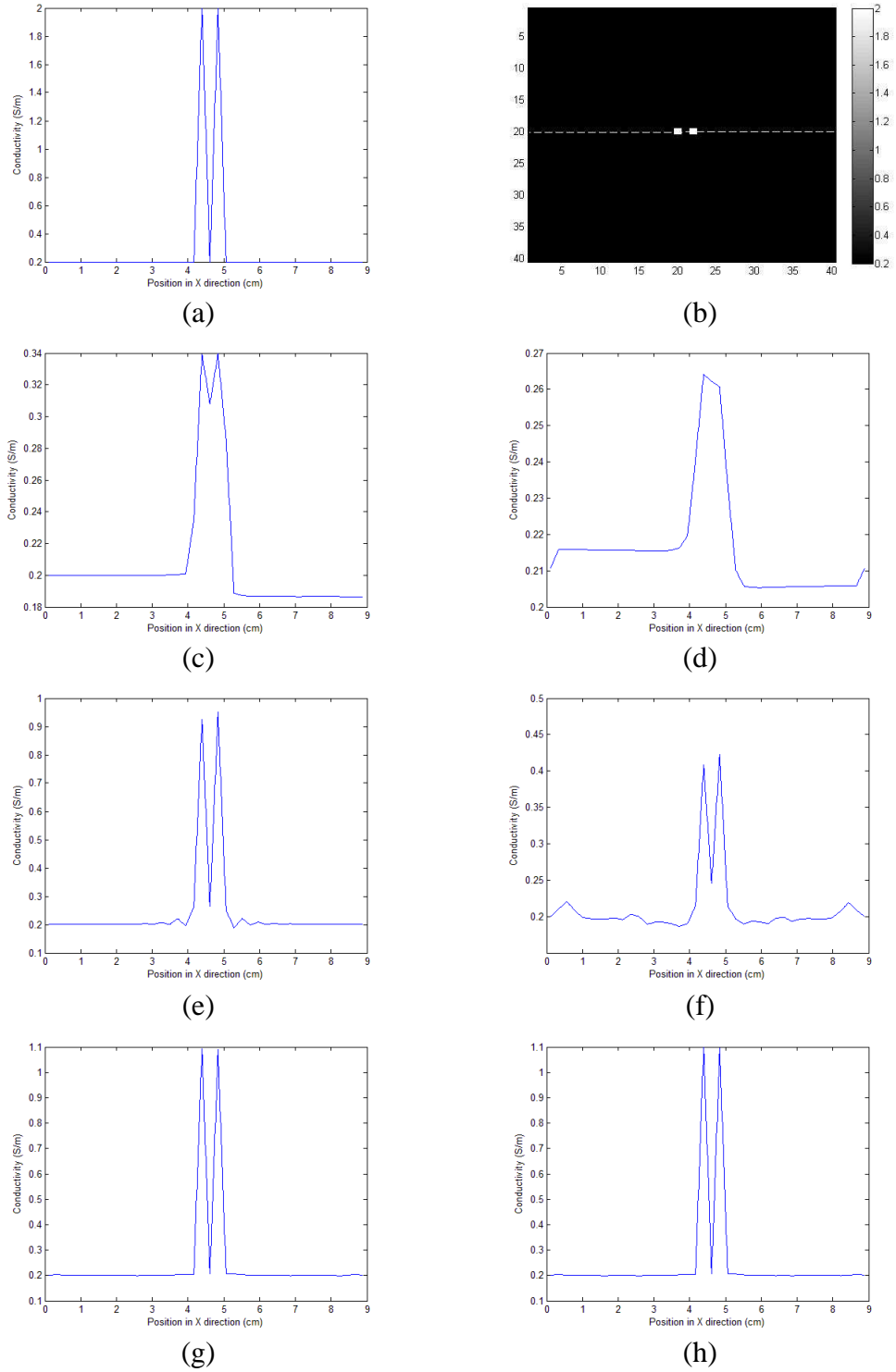


Figure 4.13 Image Profiles for Conductive Case a) Original FWHM, b) Original conductivity distribution with cross-section, c) Integration along Cartesian Grid Lines, d) Integration along Equipotential Lines, e) Solution as a Linear Equation System, f) Equipotential-Projection, g) J-Substitution, h) Hybrid

Hybrid and J-substitution algorithms have FWHM values equal to the ideal case which make them superior to other algorithms in case of spatial resolution. Results for these algorithms are obtained after three iterations where they reached their minimum errors.

For the cases of Integration along Cartesian Grid Lines and Integration along Equipotential Lines, the two impulsive elements are combined to a single element. Since these algorithms reconstruct conductivity distribution by integration, effect of impulsive elements are spread to the pixel between which makes it impossible to be recognized.

Solution as a Linear Equation System and Equipotential-Projection algorithms have a worse performance in spatial resolution than Hybrid and J-substitution algorithms but still are able to reconstruct the pixel between with some error.

Another criterion for comparison is the reconstructed value of impulsive elements which have 2 S/m conductivity value. None of the algorithms can reconstruct impulsive elements with their true values. Hybrid and J-Substitution algorithms have reconstruction value of 1.1 S/m for impulsive elements whereas Solution as a Linear Equation system has a slightly worse performance by reconstructing impulsive elements with 0.9 S/m. Other algorithms have reconstruction values less than 0.5 S/m.

As explained in Section 4.2.2, model 2 has 10 different cases. The first case is when two impulsive elements have only one pixel between. Then, at each case two impulsive elements are separated to see the effect of position over FWHM. In the 10<sup>th</sup> case, two impulsive elements are 6.075 cm apart from each other. In Figure 4.14, FWHM values of reconstructed distributions with each algorithm with respect to position are shown.

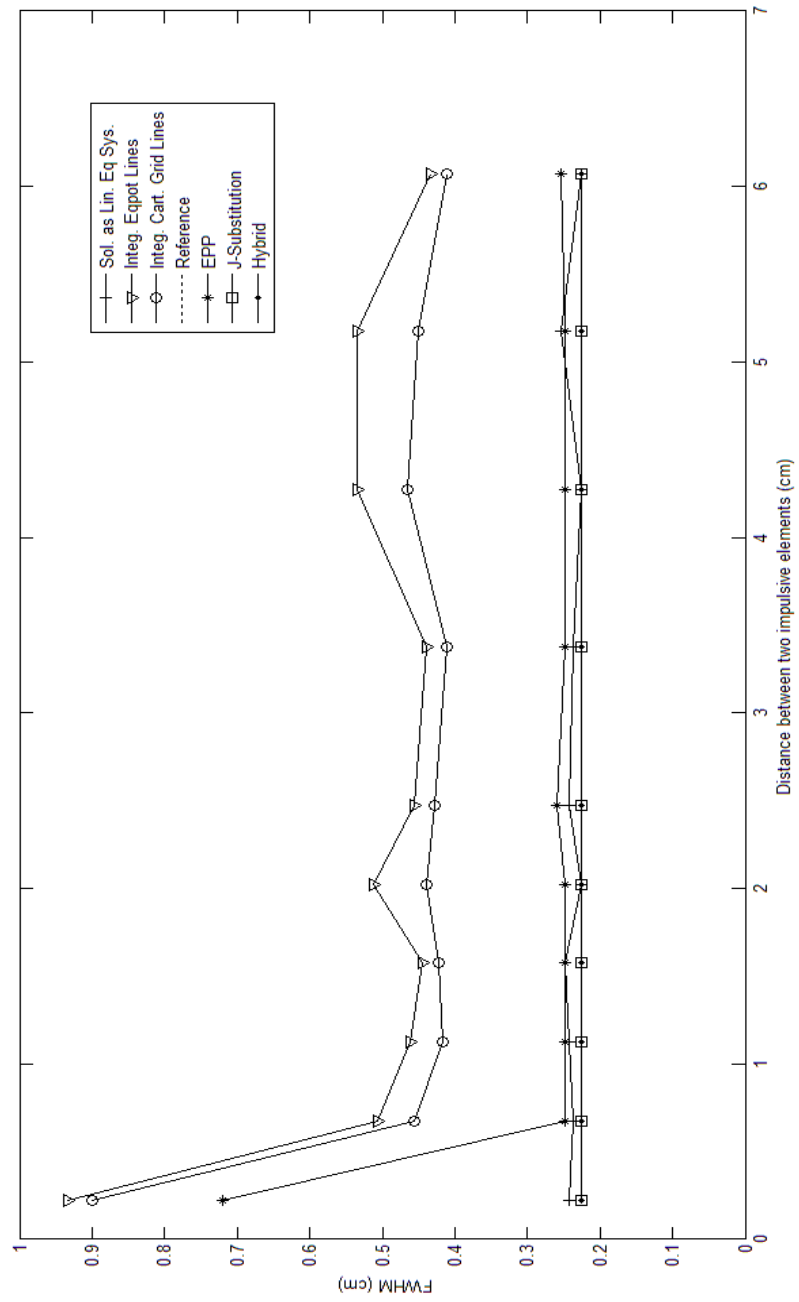


Figure 4.14 FWHM Values with respect to Position, Conductive Case

J-Substitution and Hybrid algorithms continued their superior performance when distance between impulsive elements is increased. Actually, they have 0.225 cm FWHM value, same as reference, for all cases. As a result, these algorithms can reconstruct impulsive elements independent from their positions even if they are near the electrodes.

Solution as a Linear Equation System and Equipotential-Projection algorithms have a slightly worse performance with changing distance between impulsive elements. Their FWHM values range from 0.225 cm to 0.26 cm which is still 15 % different from reference values. Equipotential-Projection algorithm reconstructed conductivity distribution with FWHM of 0.72 cm for the first case when two impulsive elements are closest to each other which show its inability to distinguish two impulsive elements.

Integration along Equipotential Lines and Integration along Cartesian Grid Lines algorithms suffer from the nature of integration. In the first case they both have FWHM of 0.9 cm. Then, in the second case, FWHM reduces to 0.5 cm and is fixed to the range from 0.45 cm to 0.55 cm with changing distance between two impulsive elements. In the case of Integration along Cartesian Grid Lines, conductivity gradient is integrated over FOV and abrupt changes are distributed to the neighbor pixels. However, current gradients which result from conductivity distribution are integrated and effects of impulsive elements are spread to neighbor pixels for Integration along Equipotential Lines.

To conclude, if FWHM values for the first case are excluded, all algorithms' FWHM values are independent from position.

The change of reconstructed values of impulsive elements with respect to position is also investigated and illustrated in Figure 4.15.

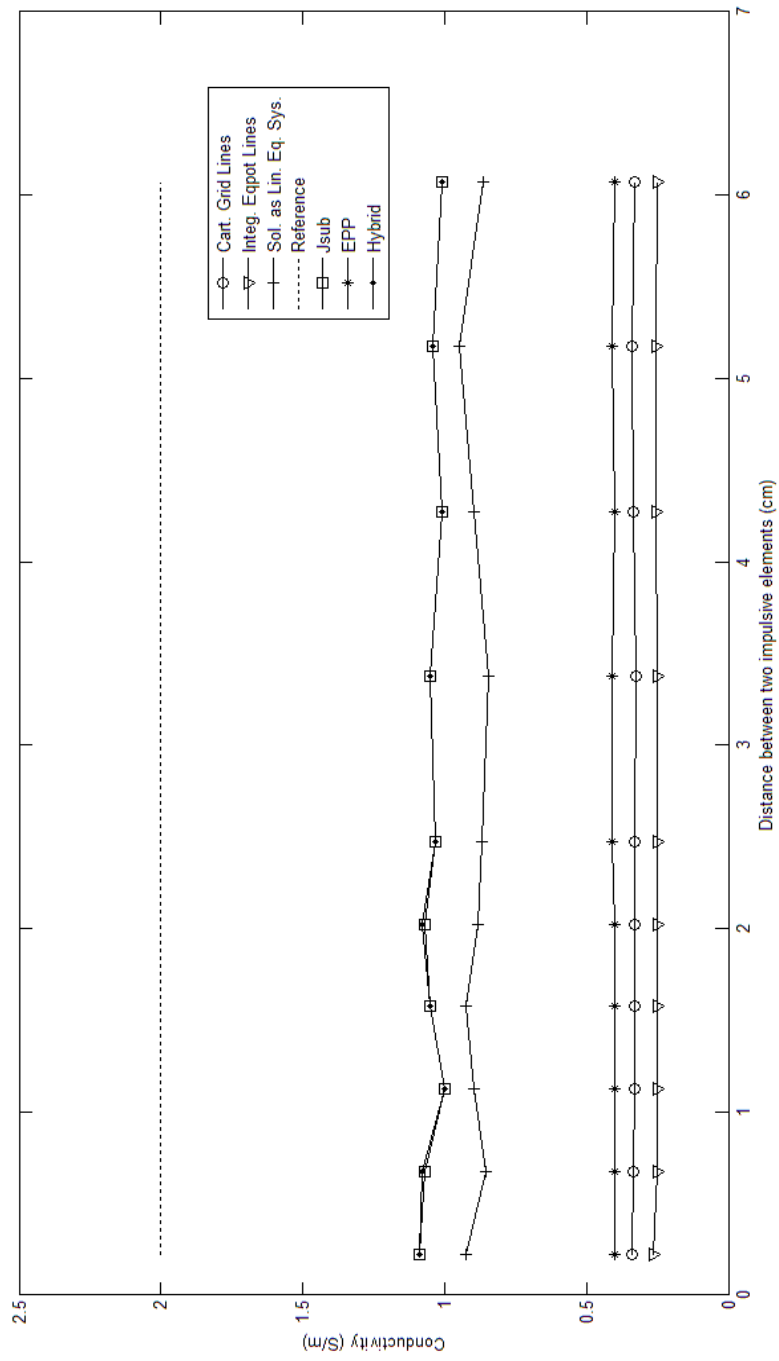


Figure 4.15 Reconstructed Values of Impulsive Elements with respect to Position, Conductive Case

None of the algorithms reconstructed the high-contrast elements with their true value, 2 S/m. J-Substitution and Hybrid algorithms have reconstruction value of 1.1 S/m which is the best performance but still with 45% error. Solution as a Linear Equation System reconstructed high-contrast elements within the range of 0.9 S/m. 0.4 S/m, 0.33 S/m and 0.25 S/m are reconstructed conductivity values for high-contrast elements for Equipotential-Projection, Integration along Cartesian Grid Lines and Integration along Equipotential Lines, respectively.

Another important result that can be deduced from Figure 4.15 is the independence of reconstructed values for high-contrast elements from position.

#### **4.5.2.3 Resistive case**

The geometry of 10 cases and positions of impulsive elements are the same as the conductive case but conductivity of impulsive elements are reduced to 0.02 S/m for the resistive case.

The ideal FWHM for the first case where impulsive elements are at the center of FOV and closest to each other and original conductivity distribution are illustrated in Figure 4.16. Also, cross-section plots of reconstructed images at the line of impulsive elements with all algorithms are also shown in Figure 4.16.

FWHM of J-Substitution and Hybrid algorithms are identical and equal to 0.2363 cm. Since FWHM of ideal case is 0.225 cm, these algorithms have an error of 5%. Results for these two algorithms are obtained after 3 iterations which turned out the minimum error. Although these algorithms are not as successful as they are in the conductive case, they still are ahead of other algorithms in terms of spatial resolution in the conductive case.

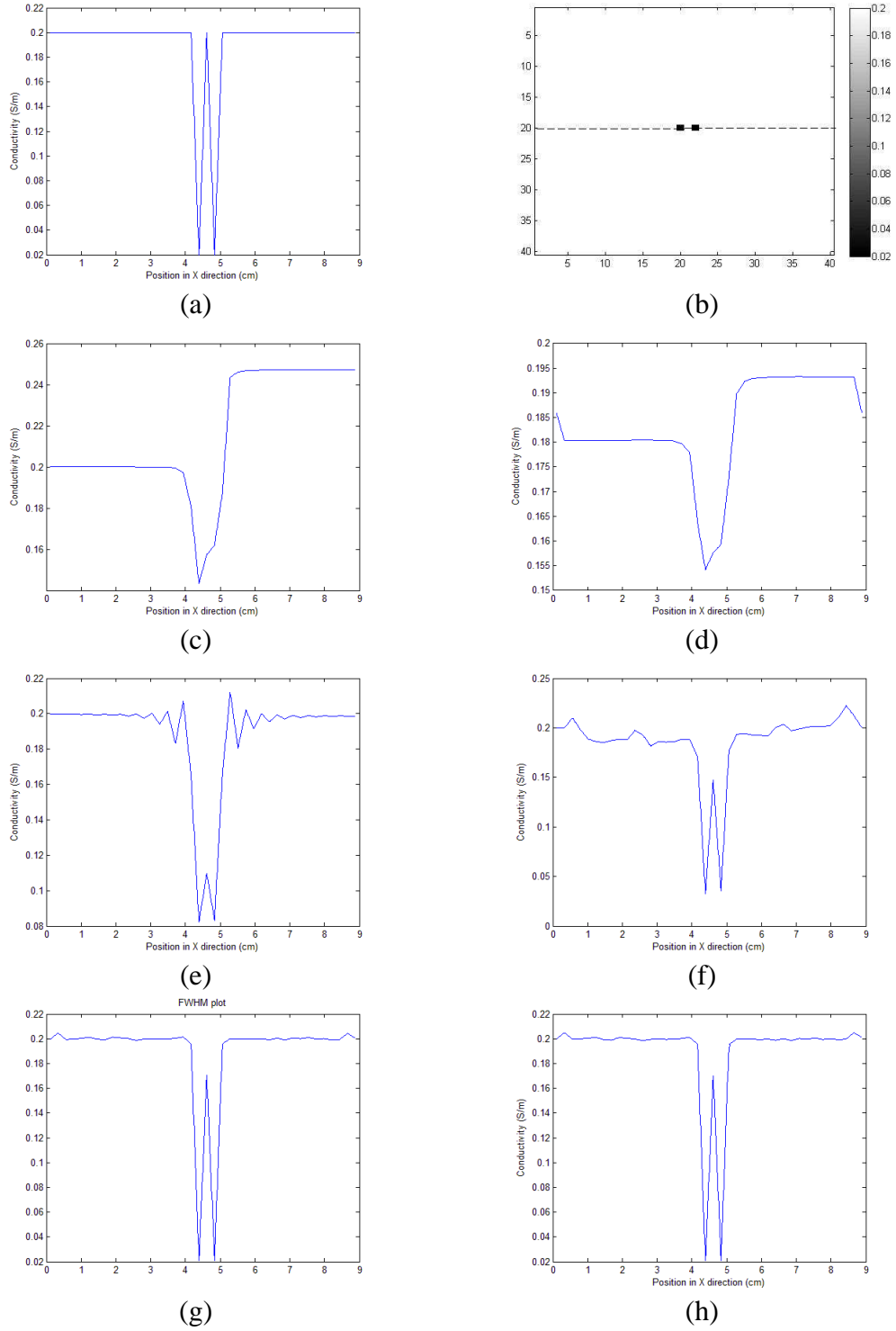


Figure 4.16 Image Profiles for Resistive Case a) Original FWHM, b) Original conductivity distribution with cross-section, c) Integration along Cartesian Grid Lines, d) Integration along Equipotential Lines, e) Solution as a Linear Equation System, f) Equipotential-Projection, g) J-Substitution, h) Hybrid

Integration along Cartesian Grid Lines and Integration along Equipotential Lines algorithms are again unsuccessful in reconstructing the pixel between. Moreover, the pixels which are not in the neighborhood of impulsive elements are reconstructed with relatively big errors. The reason is that effect of impulsive elements is carried until the end of FOV.

Solution as a Linear Equation System has a poorer performance with FWHM of 0.81 cm considering it is able to reconstruct the pixel between for the conductive case. In the resistive case, impulsive elements and the pixel between are emerged to a single element and can not be differentiated from each other.

In the case of Equipotential-Projection algorithm, FWHM is 0.79 cm but it is still possible to recognize the pixel between with some error.

When reconstructed values of impulsive elements for that case are considered, J-Substitution and Hybrid algorithms reconstructed impulsive elements with their true values, that is 0.02 S/m. After them, Equipotential-Projection algorithm comes with a reconstruction value of 0.0328 S/m. 0.0823 S/m is the reconstruction value of Solution as a Linear Equation System whereas Integration along Cartesian Grid Lines and Integration along Equipotential Lines have reconstruction values greater than 0.15 cm which coincides to more than 700% error.

FWHM values of reconstructed conductivity distributions for all algorithms with respect to position are illustrated in Figure 4.17.

Performances of J-Substitution and Hybrid algorithms are identical and have percentage error of 13% in the worst case with FWHM of 0.2542 cm. It is important to note that these two algorithms have slightly more error in the case of FWHM when their performance in the conductive case is considered. Nevertheless, they are still better than other algorithms.

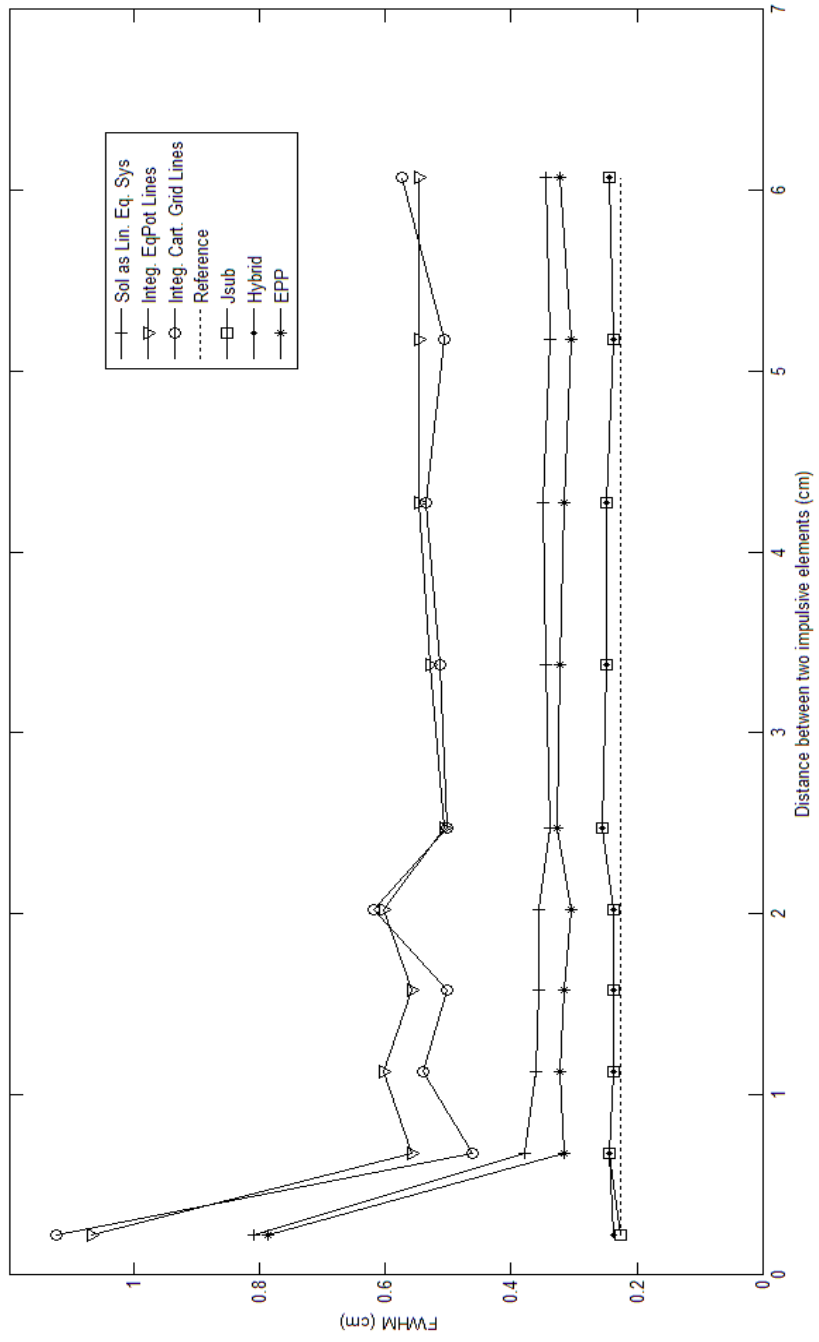


Figure 4.17 FWHM Values with respect to Position, Resistive Case

Although Solution as a Linear Equation System and Equipotential-Projection algorithms have FWHM of 0.81 cm and 0.79 in the first case, respectively, their FWHM values are fixed to 0.315-0.38 range with increasing distance between impulsive elements.

As in the conductive case, Integration along Equipotential Lines and Integration along Cartesian Grid Lines algorithms have the worst performance with FWHM values around 0.55 cm and 150% error.

Reconstructed values of impulsive elements with respect to position are illustrated in Figure 4.18.

As can be seen in Figure 4.18, only J-Substitution and Hybrid algorithms succeeded in reconstructing true values of impulsive elements with 5% error in the worst case. Equipotential-Projection algorithm has reconstruction value of 0.35 S/m and 75% error whereas Solution as a Linear Equation System has 0.8 S/m reconstruction value and 300% error. The other algorithms have reconstruction error for impulsive elements more than 700%.

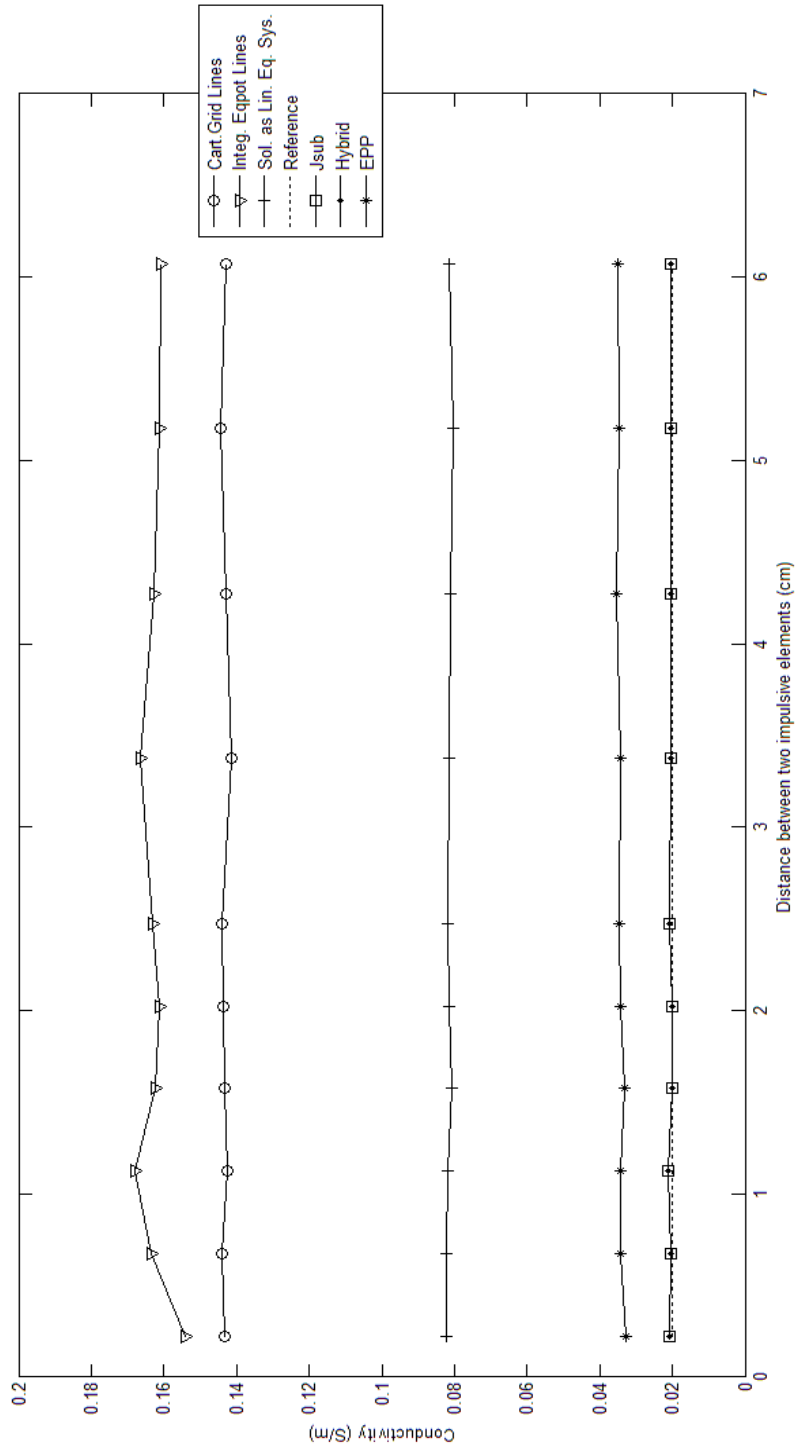


Figure 4.18 Reconstructed Values of Impulsive Elements with respect to Position, Resistive Case

#### **4.5.2.4 Reasons behind these performances**

J-Substitution and Hybrid algorithms have identical FWHM and reconstruction values for both conductive and resistive cases. They are superior to other algorithms when all comparison criteria are considered. In the conductive case, their FWHM values are equal to ideal case but reconstructed values for impulsive elements are not true whereas FWHM values are different from the ideal case and impulsive elements are reconstructed with their true values in the resistive case.

Integration along Equipotential Lines and Integration along Cartesian Grid Lines algorithms can not reconstruct the pixel between both for conductive and resistive cases. Although FWHM values are in the range of 1 cm for the first case and both algorithms, their FWHM values are fixed to values around 0.5 cm. Moreover, reconstructed values of impulsive elements have the biggest error percentage compared to other algorithms. Integration along Equipotential Lines algorithm reconstructs conductivity distribution for four times for a single current injection pattern. Due to the nature of the algorithm, it can reconstruct conductivity distribution with equipotential lines starting from only one side of the phantom. For two current injection patterns, eight conductivity distributions are found and their average is taken. Some big errors especially near the impulsive elements can not be corrected with averaging.

Integration along Cartesian Grid Lines algorithm has slightly better results than Integration along Equipotential Lines because it uses the information of two current injection patterns in a single step. It calculates conductivity gradient in FOV with a single matrix inversion and makes use of this gradient to calculate conductivity distribution. Nevertheless, effect of integration is still noticeable from the results shown above.

It is a good point to compare Equipotential-Projection and Integration along Equipotential Lines algorithms since both algorithms make use of equipotential lines. In the case Equipotential-Projection algorithm, equipotential lines originated from four sides of the phantom are used together which helps the calculation of potential

and conductivity distribution with less error which can be also seen in Figure 4.14, Figure 4.15, Figure 4.17 and Figure 4.18 above.

Solution as a Linear equation system has mid-level performance, 3<sup>rd</sup> for conductive case and 4<sup>th</sup> for resistive case.

### **4.5.3 Simulation Results for Model 3**

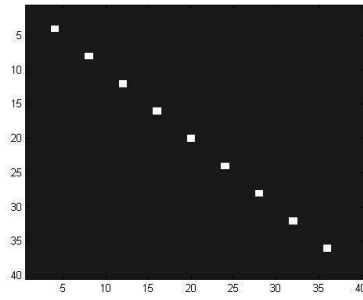
As explained earlier, simulation model 3 is constructed to see position dependency and impulsive response of reconstruction algorithms in a single simulation. Its geometry consists of nine impulsive elements with sizes of a single pixel distributed from left up corner to right bottom corner.

There are two cases as other simulation models, a conductive and a resistive case. Conductive case includes 2 S/m impulsive elements with 0.2 S/m background. On the other hand, impulsive elements in resistive case are assigned 0.02 S/m conductivity with background again set to 0.2 S/m.

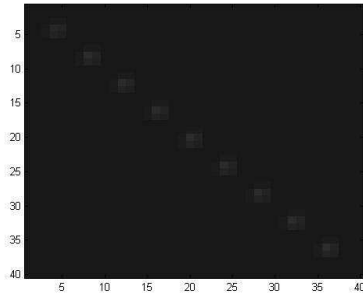
In Figure 4.19, original and reconstructed images with all six algorithms for conductive case are shown. All images have the same gray scale.

Some of the results obtained with model 2 can also be seen here, especially for Integration along Cartesian Grid Lines algorithm. It failed in reconstructing impulsive elements with their true values as impulsive elements can be barely distinguished from background. Actually, impulsive elements are reconstructed with conductivity values around 0.35 S/m. Moreover, due to integration effect, neighbor pixels of impulsive elements are affected and diverged from their true values. However, this algorithm is position independent.

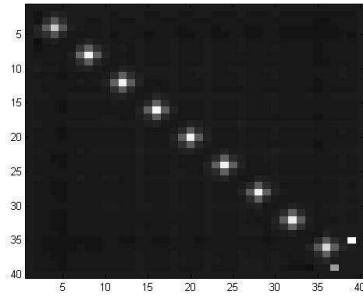
Artifacts based on integration are more obvious with Integration along Equipotential Lines as these artifacts are spread to background in the form of erroneous lines. However, it succeeded in reconstruction of all impulsive elements as average value of impulsive elements is 1.9 S/m which corresponds to 5% error. So, Integration along Equipotential Lines algorithm is a position independent algorithm.



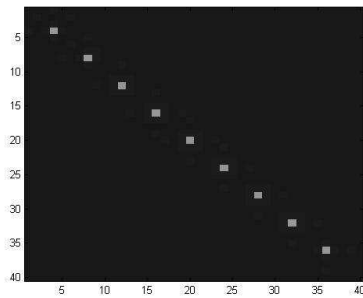
(a)



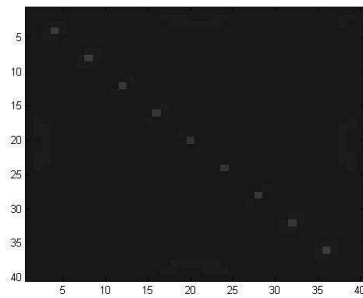
(b)



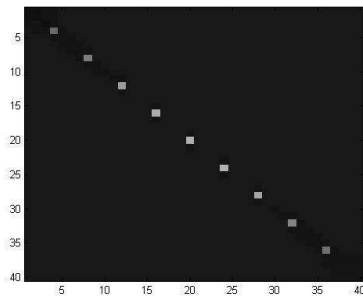
(c)



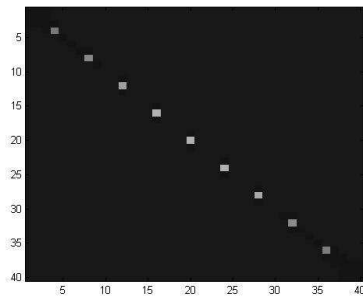
(d)



(e)



(f)



(g)

Figure 4.19 Reconstructed Images for Model 3 Conductive Case a) Original Distribution, b) Integration along Cartesian Grid Lines, c) Integration along Equipotential Lines, d) Solution as a Linear Equation System, e) Equipotential-Projection, f) J-Substitution, g) Hybrid

Solution as a Linear Equation System algorithm also proved to be independent from position because all impulsive elements are reconstructed with 1.2 S/m conductivity. Also, typical grid effect of this algorithm is also seen with simulation model 3.

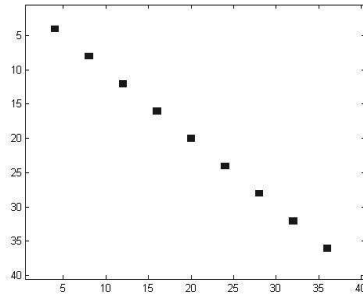
Equipotential-Projection algorithm is also position independent as can be seen in Figure 4.19e. Moreover, it reconstructed impulsive elements with conductivity values around 0.45 S/m which is the worst performance after Integration along Cartesian Grid Lines algorithm.

J-substitution and Hybrid algorithms have a similar performance with simulation model 2. They both are position independent. They reconstructed impulsive elements near the corners of FOV with bigger errors, since current is applied with small electrodes and current density information is limited in these areas. However, they managed to reconstruct impulsive elements in the middle of FOV with 1.4 S/m conductivity value. As a result, these two algorithms are position independent and their reconstructed images turn out to be undistorted along with Solution as a Linear Equation System algorithm in a perceptual manner.

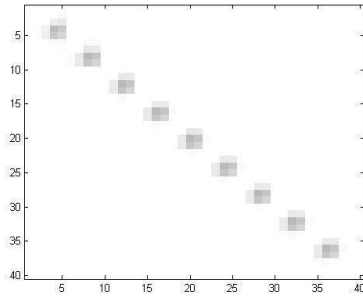
The other analysis with simulation model 2 is the resistive case. Original conductivity distribution and simulation results are shown in Figure 4.20.

With resistive impulsive elements, Integration along Cartesian Grid Lines algorithm can not reconstruct them with their true values as they have reconstruction values around 0.14 S/m. Nevertheless, it also proved to be position independent for resistive case.

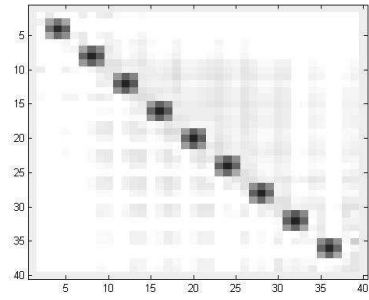
Integration artifact of Integration along Equipotential Lines algorithm continues for resistive case. Since result of this algorithm constitutes of averaging of four reconstructed conductivity distributions for equipotential lines originated from four boundaries, integration artifact is seen in all surrounding pixels of impulsive pixels. But it is position independent for resistive case, too.



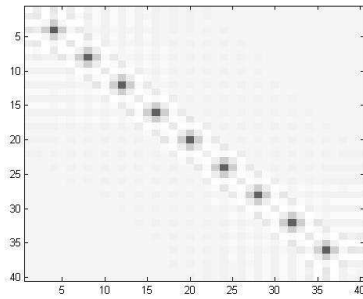
(a)



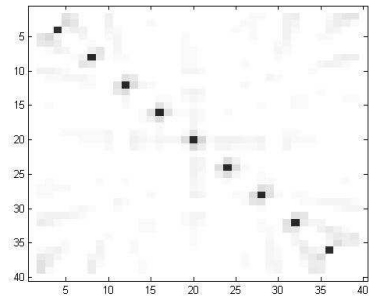
(b)



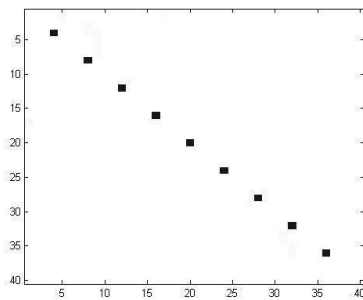
(c)



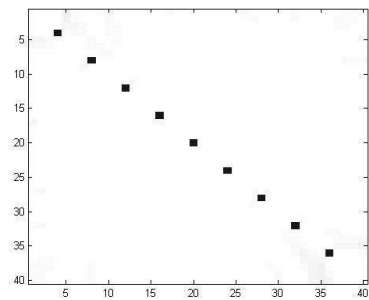
(d)



(e)



(f)



(g)

Figure 4.20 Reconstructed Images for Model 3 Resistive Case a) Original Distribution, b) Integration along Cartesian Grid Lines, c) Integration along Equipotential Lines, d) Solution as a Linear Equation System, e) Equipotential-Projection, f) J-Substitution, g) Hybrid

Solution as a Linear Equation System algorithm's grid effect is also present for resistive case and can be clearly seen in Figure 4.20d. Moreover, this artifact is increasing in corners of FOV for resistive case. This algorithm is also independent from position for resistive impulsive elements.

There appears to be more background errors for Equipotential-Projection algorithm than errors in conductive case which get bigger in corners of FOV since current density is lower in these areas. However, it is still position independent as in conductive case.

J-substitution and Hybrid algorithm reconstructed impulsive elements and background with least errors and sharp boundaries than other algorithms with the exception that Hybrid algorithm can not correct erroneous lines in the corners from Equipotential-Projection algorithm. Both algorithms are also position independent as in conductive case.

In conclusion, all algorithms are independent from position in FOV both for conductive and resistive impulsive elements. However, some of the algorithms failed in reconstructing impulsive elements with their true values and defining element boundaries sharply.

#### **4.5.4 Simulation Results for Model 4**

##### **4.5.4.1 Numerical accuracy with changing conductivity contrast**

This section is allocated for results obtained by simulation of reconstruction algorithms with model 4. As explained in Section 4.2.4, model 4 is formed by a single square in the middle of the phantom. Its conductivity changes in each simulation. For conductive case, background conductivity is fixed to 0.2 S/m and conductivity of square is changed from 0.2 to 2 with an increase 0.2 S/m at each step. On the other hand, resistive case includes 0.2 S/m conductivity for the background and square conductivity diminishes to 0.02 S/m at 10 steps starting again from 0.2 S/m.

Three different analyses will be employed for comparison of reconstruction algorithms in this section. These are general error, square error and average conductivity value of square. All analyses are designed to see the change of these parameters with changing conductivity contrast.

#### **4.5.4.2 Conductive case**

In Figure 4.21, general errors for all reconstruction algorithms are plotted against changing square conductivity. All algorithms except Integration along Cartesian Grid Lines algorithm converge to some percentage error.

Among three algorithms with the best performance, Hybrid algorithm has 5.2% error when square conductivity is 2 S/m. Then, J-Substitution and Equipotential-Projection algorithms have general reconstruction error of 8.1% and 9%, respectively. Results for J-substitution and Hybrid algorithm are obtained after three iterations where they reached their minimum error. It is important to note the difference between Hybrid and J-Substitution algorithms since they usually have identical or similar results with other comparison criteria. Hybrid algorithm takes the results of Equipotential-Projection algorithm, which is still close to J-substitution algorithm, and diminishes general error from 9% to 5.2%. This can be seen as an optimization for cases where conductivity contrast becomes larger.

For the cases of Integration along Equipotential Lines and Solution as a Linear Equation System, general error converges to 47% and 32%, respectively.

Although all algorithms converge to some error, Integration along Cartesian Grid Lines algorithm diverges and general error becomes larger as conductivity contrast between background and square increases.

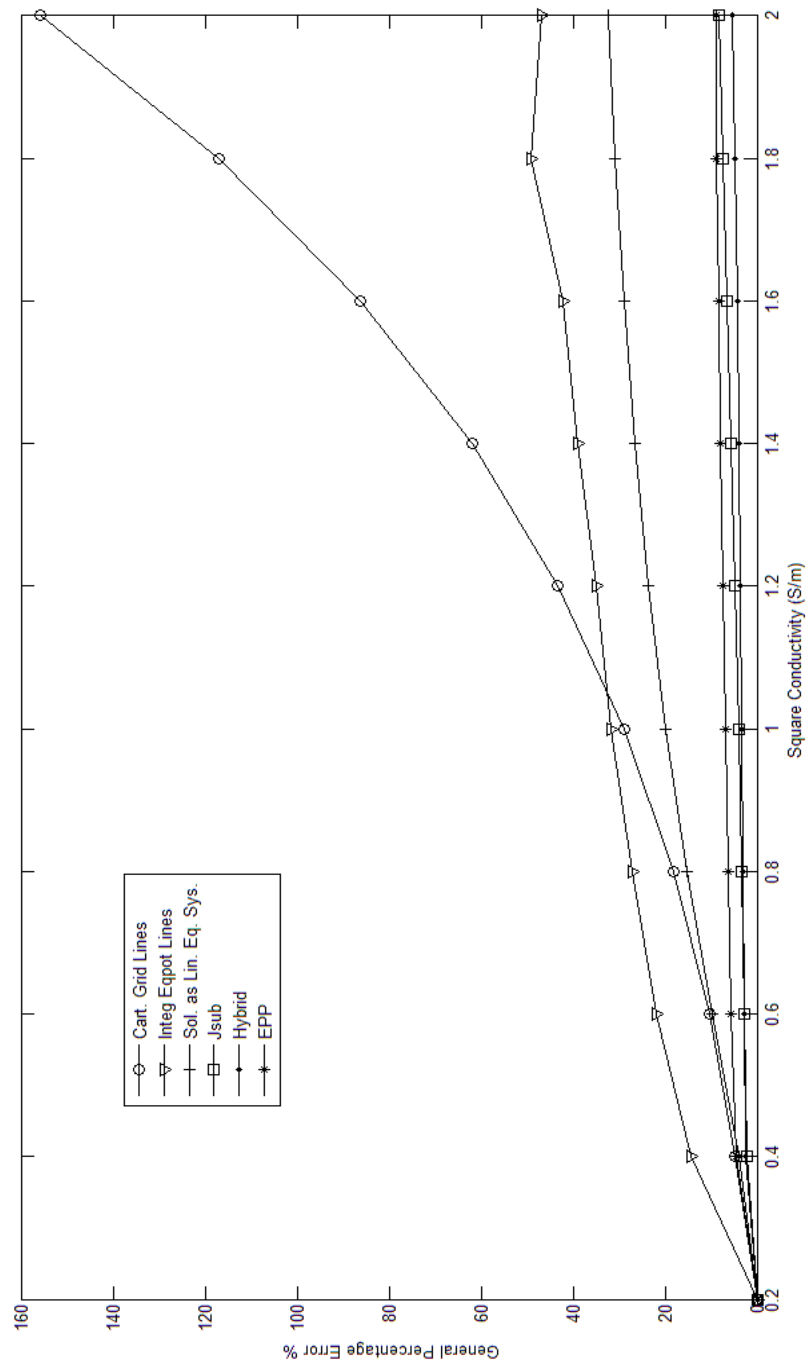


Figure 4.21 General Errors with Changing Conductivity Contrast, Conductive Case

Next analysis consists of error percentage of square element with respect to changing conductivity. Figure 4.22 illustrates plots of square percentage error when conductivity of square element is increased from 0.2 S/m to 2 S/m stepwise.

Hybrid algorithm continues its superior performance over other reconstruction algorithms with a percentage error of 16% when conductivity contrast is 10, 0.2 S/m for the background and 2 S/m for the square. Optimization effect of Hybrid algorithm is more obvious when square error is considered.

J-Substitution, Equipotential-Projection and Solution as a Linear Equation System algorithms converge to percentage error of 27% for square element. Moreover, Integration along Equipotential Lines has a similar characteristic as in the case of general error, but this time with 64% error. On the other hand, Integration along Cartesian Grid Lines again failed in that analysis since it diverges with increasing conductivity contrast.

There is a similar phenomenon for all reconstruction algorithms. Their percentage errors for square elements are bigger than general percentage errors. So, square elements are reconstructed with more error than background.

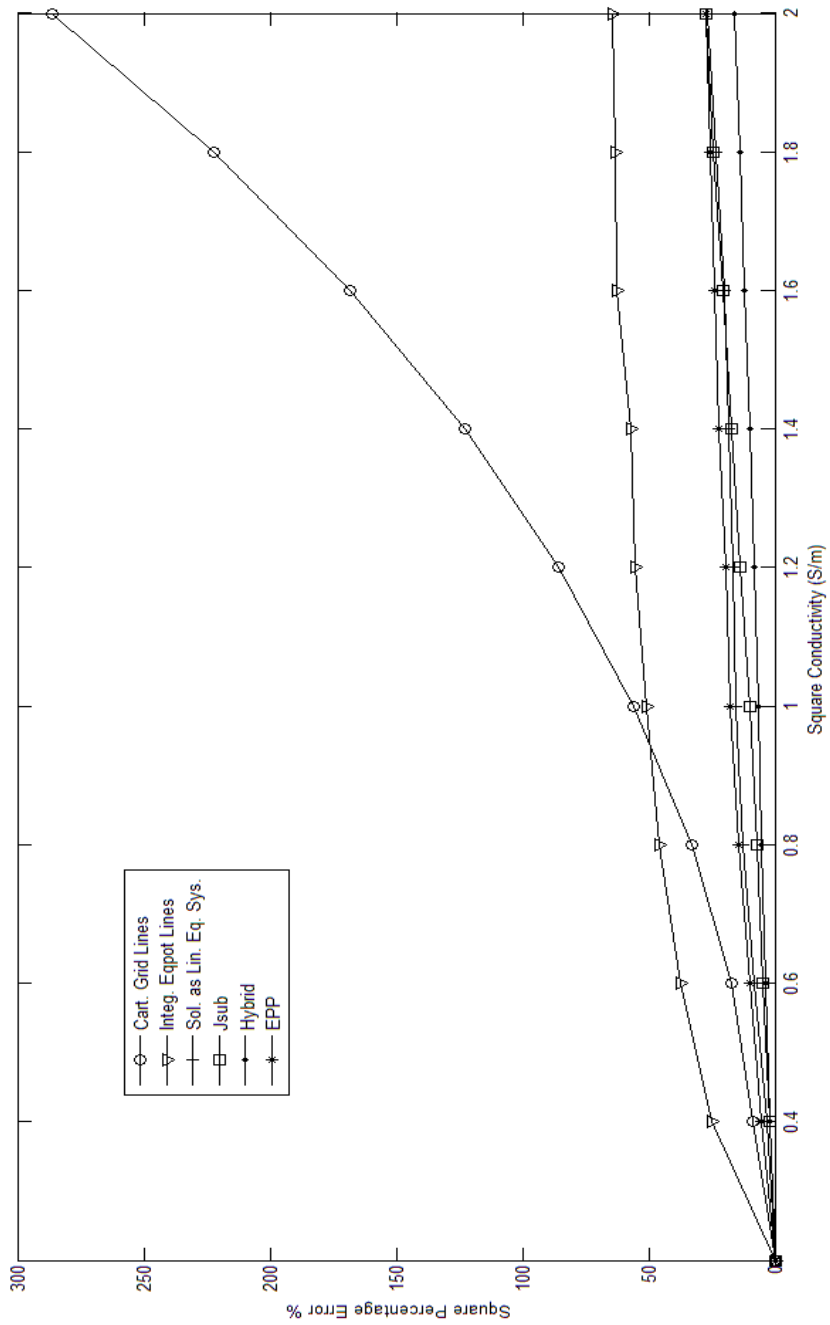


Figure 4.22 Square Errors with Changing Conductivity Contrast, Conductive Case

Last analysis for conductive case is change of average conductivity value of square element with conductivity contrast. Figure 4.23 shows plots of average conductivity values for reconstructed square elements. Figure 4.24 is the zoomed version of Figure 4.23, so relation between algorithms except Integration along Cartesian Grid Lines can be seen clearly. Moreover, reconstructed conductivity distributions for the conductive case where square conductivity is set to 2 S/m are shown in Figure 4.25 to give a perceptual idea.

When Figure 4.25 and Figure 4.23 are analyzed together, source of errors for Integration along Cartesian Grid Lines and Integration along Equipotential Lines algorithms are clearly seen. Even boundaries of square element are not definite. In the case of Integration along Cartesian Grid Lines algorithm, pixels of square elements are diverged to values around 10 S/m and boundary is still not definite. On the other hand, effect of boundary elements are spread to background for Integration along Equipotential Lines.

Although average conductivity values of Solution as a Linear Equation System and Equipotential-Projection algorithms are around 1.6 S/m, reconstructed images are distorted in a perceptual manner. Reconstructed conductivity values of pixels are in the range from 1.2 S/m to 3 S/m. Moreover, relatively big general error for Solution as a Linear Equation System comes from artifact seen in square element which continues in the background.

For the case of J-substitution algorithm, if corners of square element are not considered, reconstructed values of pixels are in the range of 1.2 S/m to 1.6 S/m. On the other hand, Hybrid algorithm has a range of 1.4 S/m to 1.8 S/m. So, in a perceptual manner, square elements are more homogeneous with respect to other algorithms. Moreover, these algorithms are successful in specifying boundaries of square clearly.

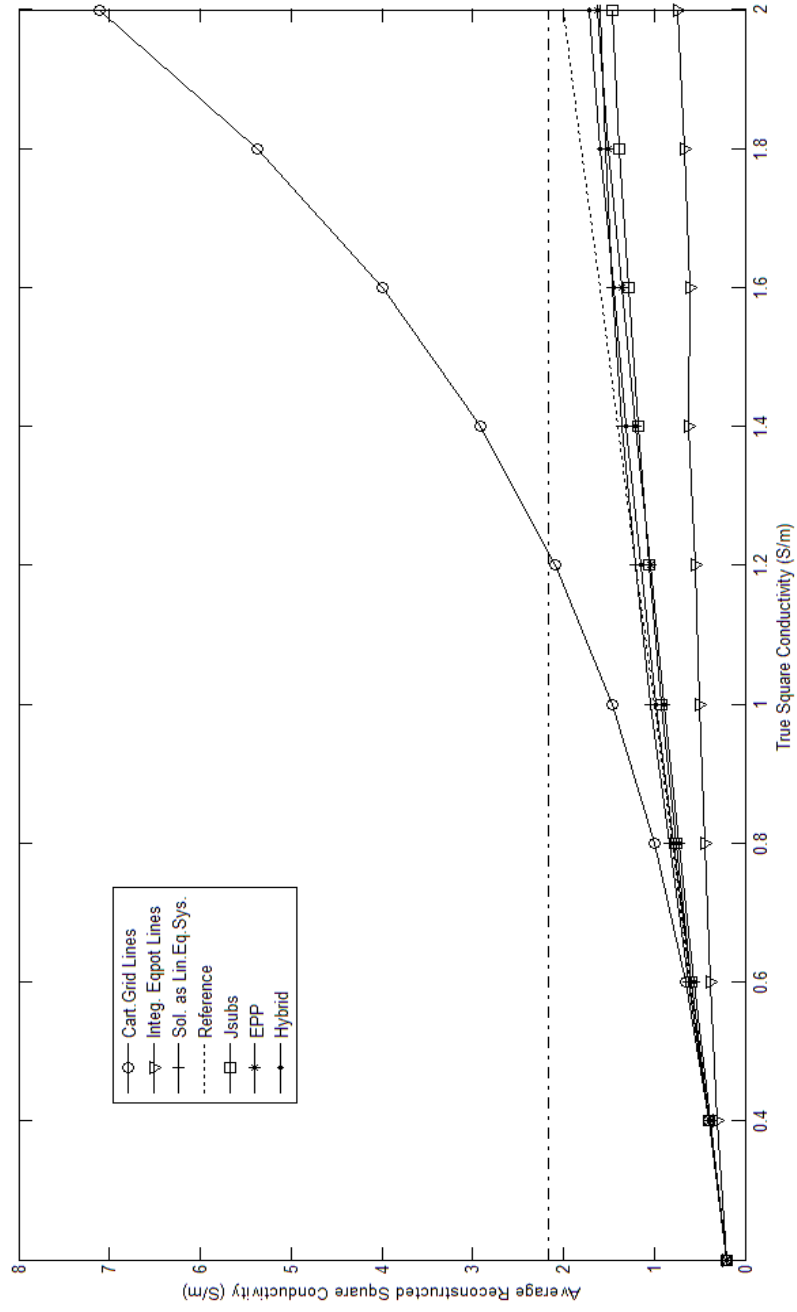


Figure 4.23 Average Conductivity Value of Square with Changing Conductivity Contrast, Conductive Case

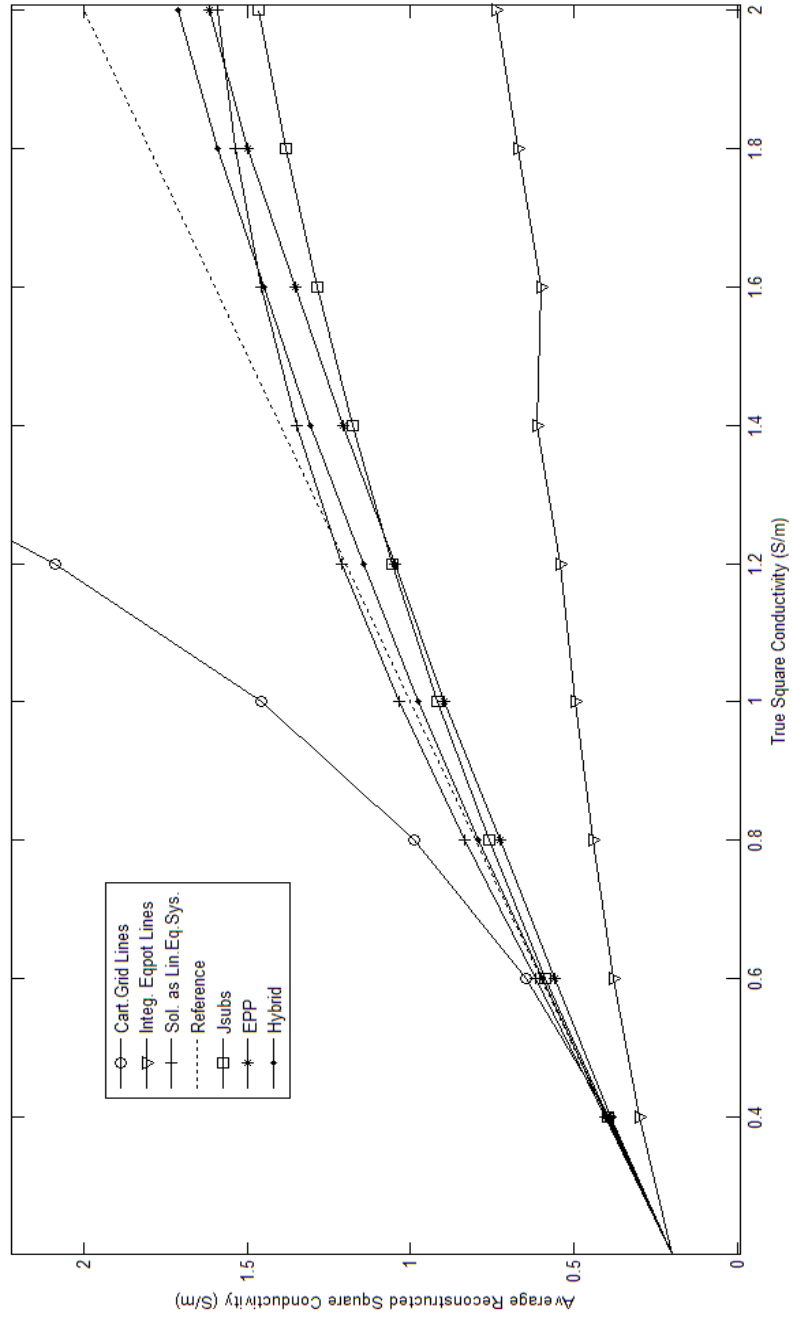
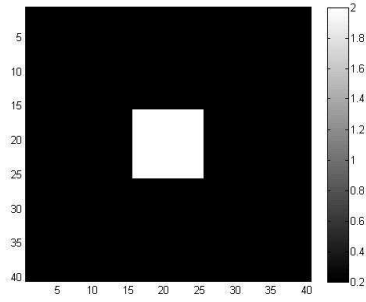
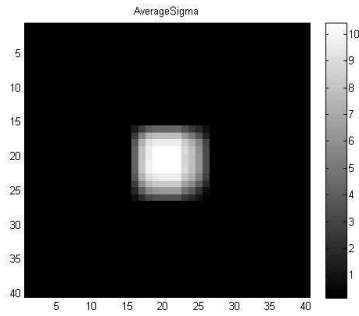


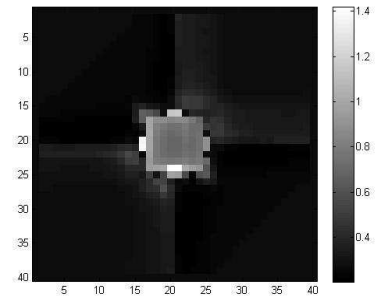
Figure 4.24 Average Conductivity Value of Square with Changing Conductivity Contrast , Conductive Case, Zoomed Version



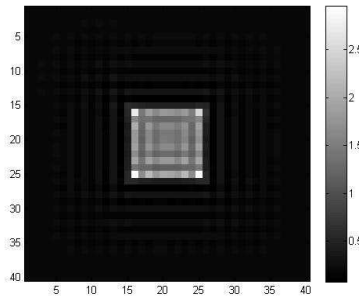
(a)



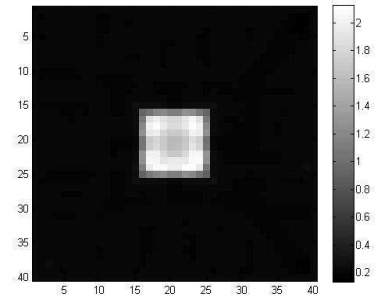
(b)



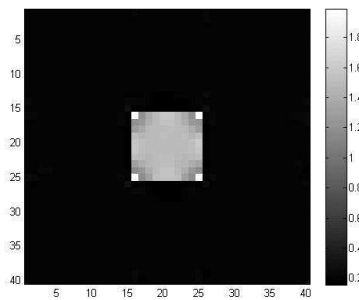
(c)



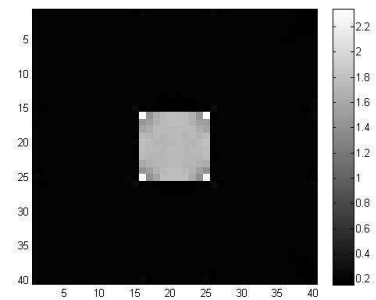
(d)



(e)



(f)



(g)

Figure 4.25 Reconstructed Conductivity Distributions for Model 4 Conductive Case a) Original Distribution, b) Integration along Cartesian Grid Lines, c) Integration along Equipotential Lines, d) Solution as a Linear Equation System, e) Equipotential-Projection, f) J-Substitution, g) Hybrid

#### 4.5.4.3 Resistive case

In Figure 4.26, general errors with respect to square conductivity are plotted for all algorithms. Integration along Equipotential Lines, Integration along Cartesian Grid Lines and solution as a Linear Equation System algorithms diverge whereas other algorithms have an increase in general error when square conductivity reduces but converges to some error.

Divergence of Integration along Equipotential Lines is more obvious as it reaches 80% error for the case where square conductivity has its minimum value, 0.02 S/m. On the other hand, Integration along Cartesian Grid Lines and Solution as a Linear Equation System algorithms have 35% general error for that simulation. All algorithms except Integration along Equipotential Lines algorithm have similar general errors until square conductivity reduces to half of background conductivity, that is for conductivity values greater than 0.1 S/m. After that point, Integration along Cartesian Grid Lines and Solution as a Linear Equation System algorithms start to diverge as square conductivity diminishes to 0.02 S/m.

Among three convergent algorithms, which are Hybrid, J-Substitution and Equipotential- Projection algorithms, Hybrid algorithm has smallest general error of 4.5% when square conductivity is set to 0.02 S/m. Then, Equipotential- Projection and J-substitution algorithms follow Hybrid algorithm with 6.3% and 7.6% general error, respectively. Application of Hybrid algorithm with the result of Equipotential- Projection algorithm reduced general error when conductivity value of square element is lower than 0.07 S/m. This result can be seen better in Figure 4.27 which is zoomed version of Figure 4.26 for general error values less than 10%.

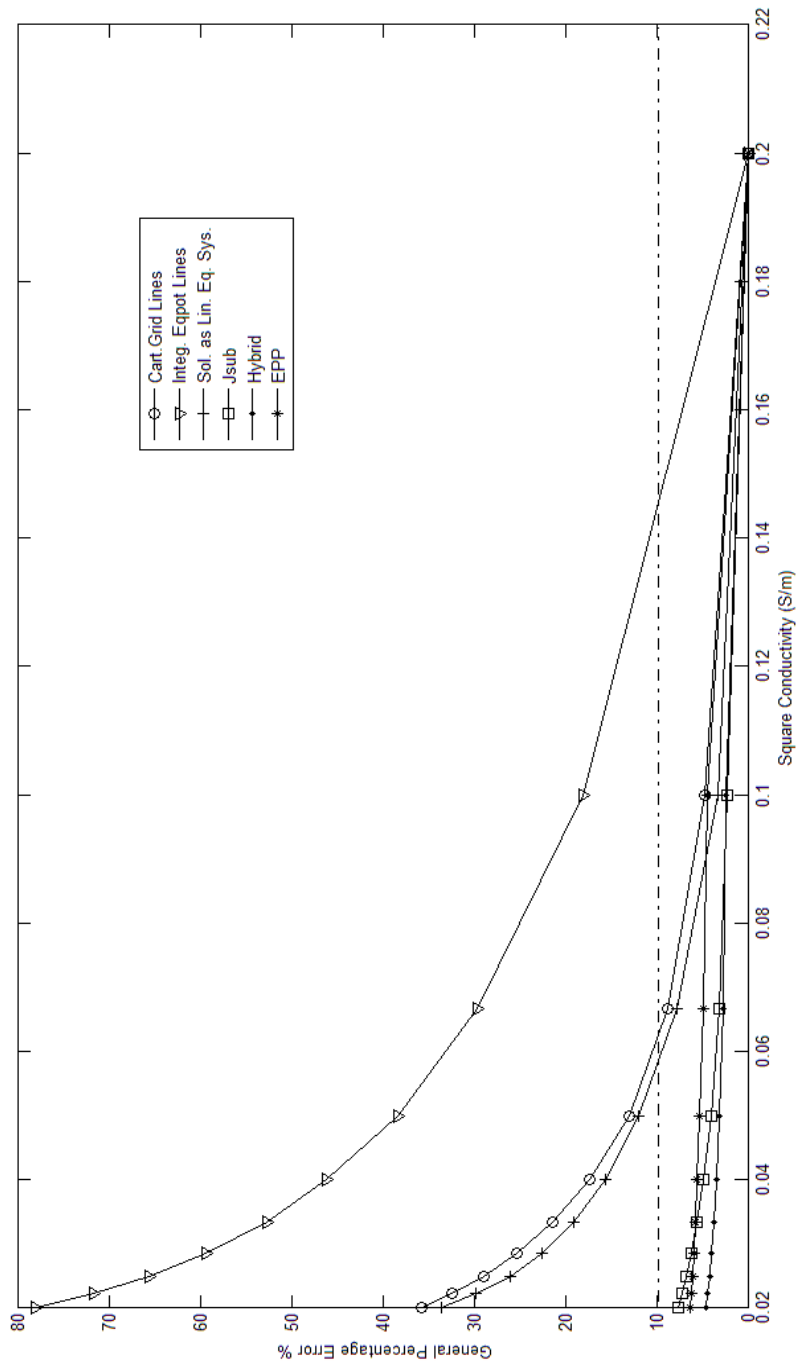


Figure 4.26 General Errors with Changing Conductivity Contrast, Resistive Case

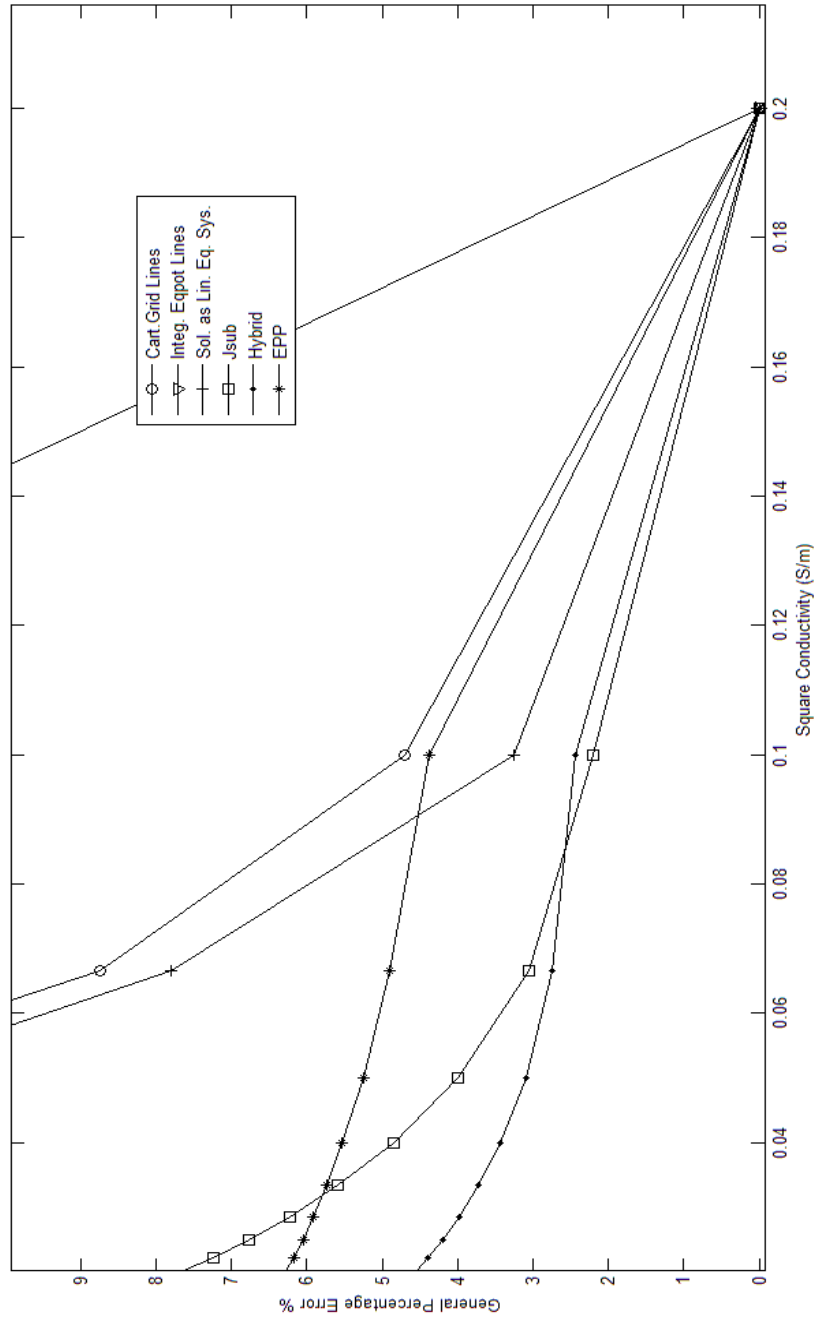


Figure 4.27 General Errors with Changing Conductivity Contrast, Resistive Case, Zoomed Version

Next analysis consists of change of square element error with respect to conductivity contrast. Figure 4.28 illustrates errors for square elements when conductivity contrast between square and background diminishes from 1 to 1/10. Moreover, Figure 4.29 is the zoomed version of Figure 4.28 which marks the relation between convergent algorithms.

As shown in Figure 4.28, errors of square elements become larger with increasing conductivity contrast for Integration along Equipotential Lines, Integration along Cartesian Grid Lines and Solution as a Linear Equation System algorithms.

The optimization effect of Hybrid algorithm over J-Substitution algorithm continues for square element. When square conductivity is 0.02 S/m, Hybrid algorithm has 2.6% error whereas J-substitution algorithm reconstructs square element with an error of 5.6%.

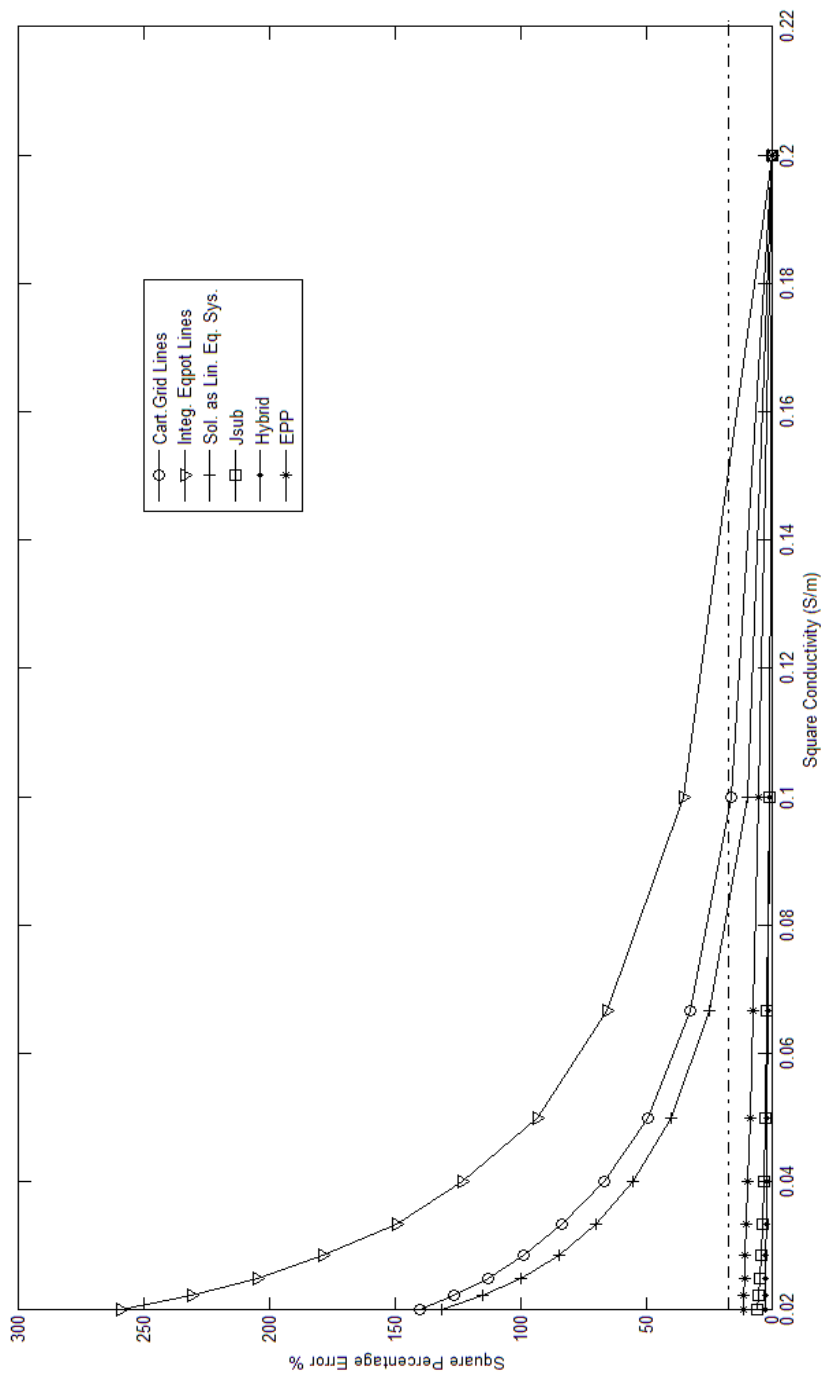


Figure 4.28 Square Errors with Changing Conductivity Contrast, Resistive Case

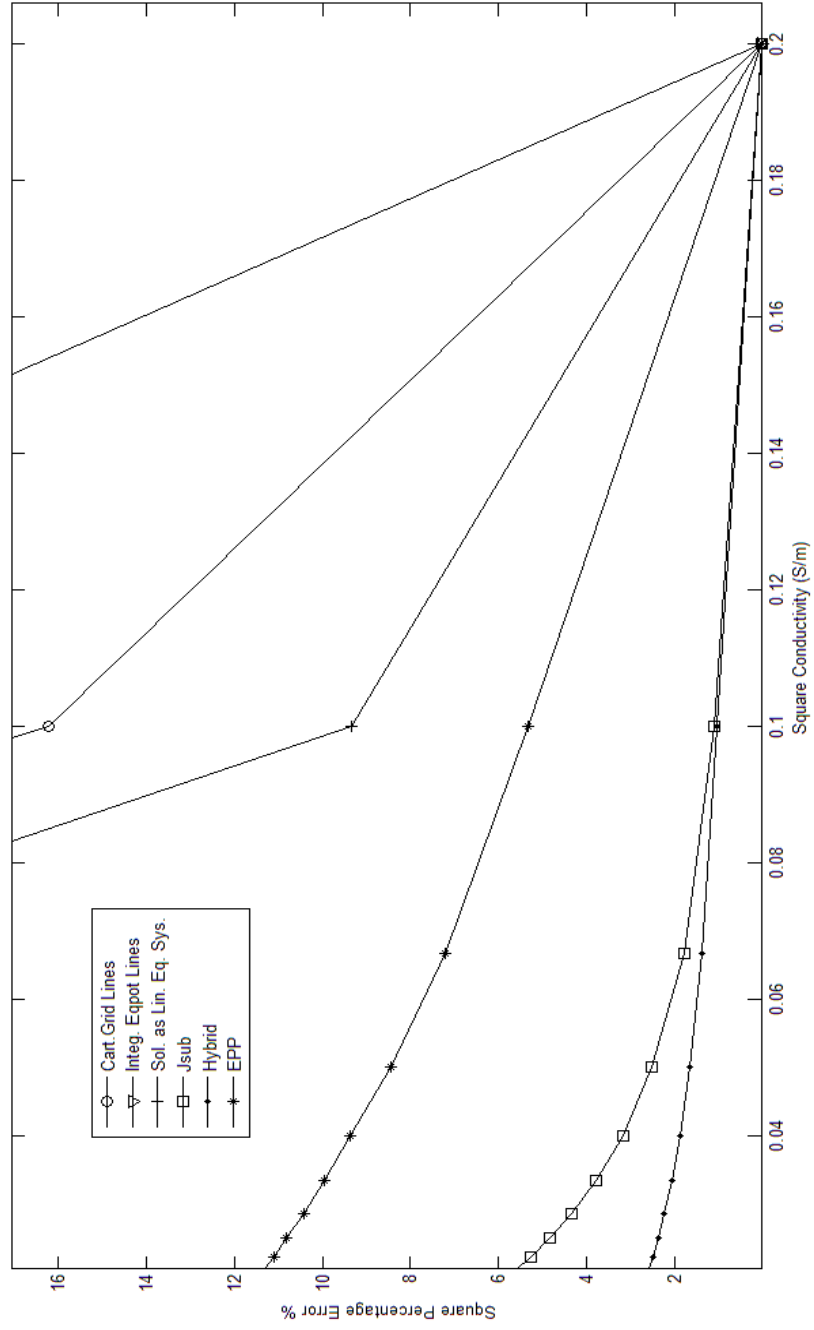


Figure 4.29 Square Errors with Changing Conductivity Contrast, Resistive Case, Zoomed Version

Reconstructed average value for square elements is another comparison criterion which are illustrated in Figure 4.30. Moreover, reconstructed conductivity distributions for the case of square conductivity set to 0.02 S/m are plotted to give a perceptual idea.

All algorithms except Integration along Equipotential Lines algorithm reconstructed square element with its true average values. The key point is that this result can be deceptive for some of the algorithms.

If Figure 4.28 and Figure 4.31 are considered together, it can be seen that Integration along Cartesian Grid Lines and Solution as a Linear Equation System algorithms have around 140% error for square element. But average reconstructed square element conductivity values are close to true values. Although, these algorithms do not reconstruct each square element with its true value, they manage to have average values in the range of true square conductivity. This phenomenon can be clearly seen in Figure 4.31d which contains conductivity values over 0.1 S/m and less than 0.01 S/m together inside square element which in fact has 0.02 S/m conductivity.

Equipotential-Projection, J-Substitution and Hybrid algorithms have square element errors less than 12% and reconstructed average square conductivity in the range of true values. These results imply that these algorithms reconstruct each square element with minimum error. There are no extreme reconstructed values for square elements. Moreover, homogenous structure of square elements in Figure 4.31f and Figure 4.31g prove that result.

In a perceptual manner, J-Substitution and Hybrid algorithms defined boundaries of square element better than Equipotential-Projection algorithm. Nevertheless, these algorithms have miscalculated values at corners of square element which tend to distort background.

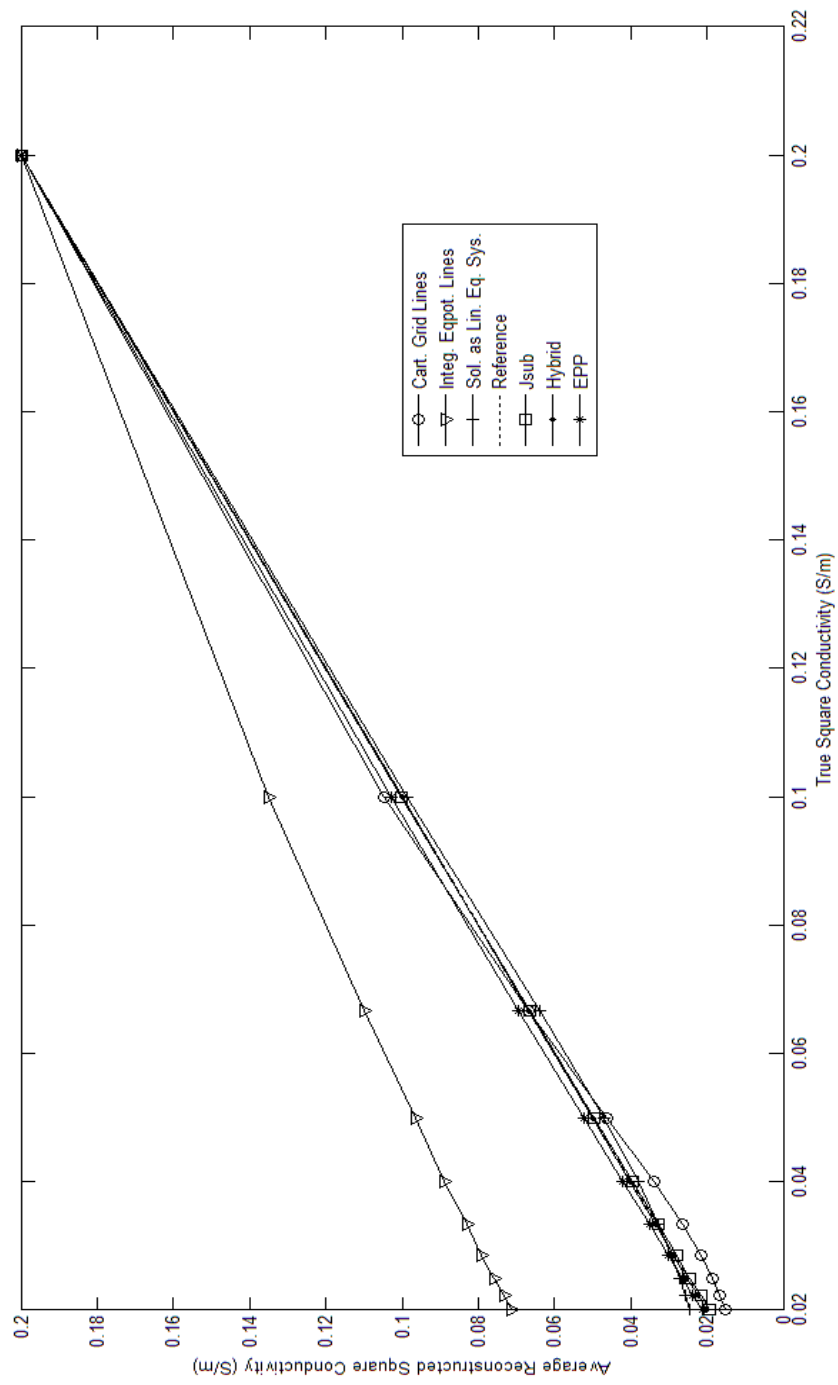
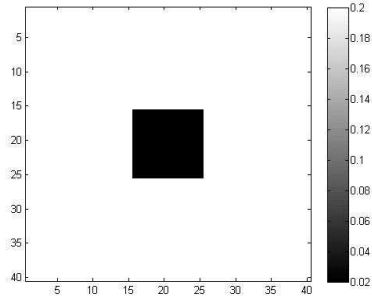
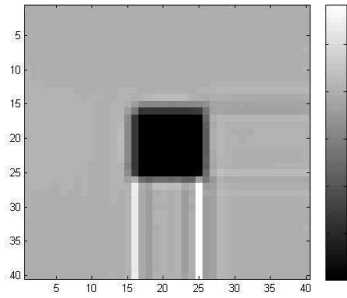


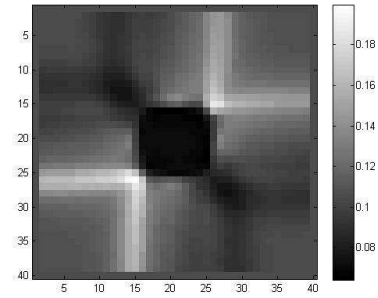
Figure 4.30 Average Conductivity Value of Square with Changing Conductivity Contrast , Resistive Case



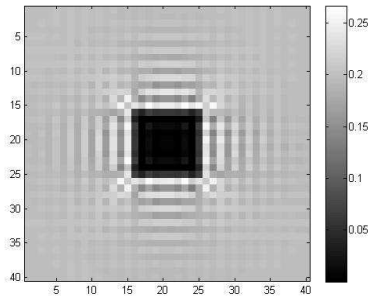
(a)



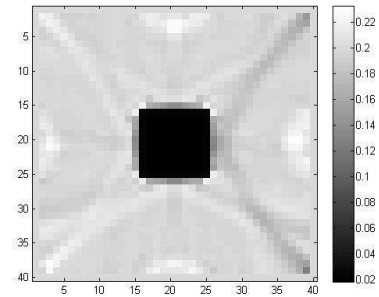
(b)



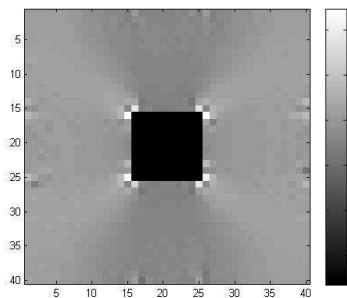
(c)



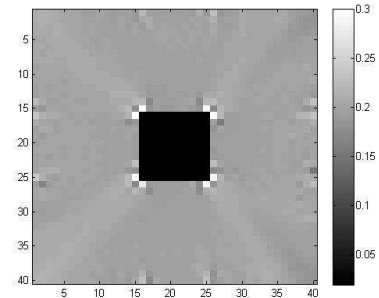
(d)



(e)



(f)



(g)

Figure 4.31 Reconstructed Conductivity Distributions for Model 4 Resistive Case a) Original Distribution, b) Integration along Cartesian Grid Lines, c) Integration along Equipotential Lines, d) Solution as a Linear Equation System, e) Equipotential-Projection, f) J-Substitution, g) Hybrid

#### **4.5.5 Simulation Results for Thorax Phantom**

Last phantom used for simulation is thorax phantom whose conductivity distribution is shown in Figure 4.32a. This analysis enables to see performance of reconstruction algorithms with a complex geometry and true tissue conductivities. As explained earlier tissue conductivities vary [32]. There are extremely resistive areas like bone structures and extreme conductive tissues like spinal cord. Simulation of thorax phantom gives an idea on applying reconstruction algorithms to real experiments.

Simulation study of thorax phantom with reconstruction algorithms is also carried out with noisy data. Two noise levels are employed as in simulations with model 1, SNR 30 and SNR 13. Moreover, percentage errors of all tissue regions and overall error are calculated for each reconstruction algorithm and noise level which helps to make a numerical analysis.

Reconstructed images and original conductivity distribution for noise free case are illustrated in Figure 4.32. It is important to note that all images have the same gray scale of Figure 4.32a.

Integration along Equipotential Lines algorithm can not reconstruct thorax phantom because most of the equipotential lines initiated from a boundary can not reach to another boundary and are eliminated for this reason. Remaining equipotential lines do not have enough information to reconstruct conductivity distribution. So, Integration along Equipotential Lines algorithm is excluded from thorax phantom simulations.

Errors for spinal cord region are between 97% and 100% for all algorithms. Spinal cord is covered by bone and there is too little amount of current going inside bone which eventually forces reconstructed values of spinal cord to be similar to bone conductivity. As a result, they are close to zero and 100% error. This conclusion is valid for algorithms.

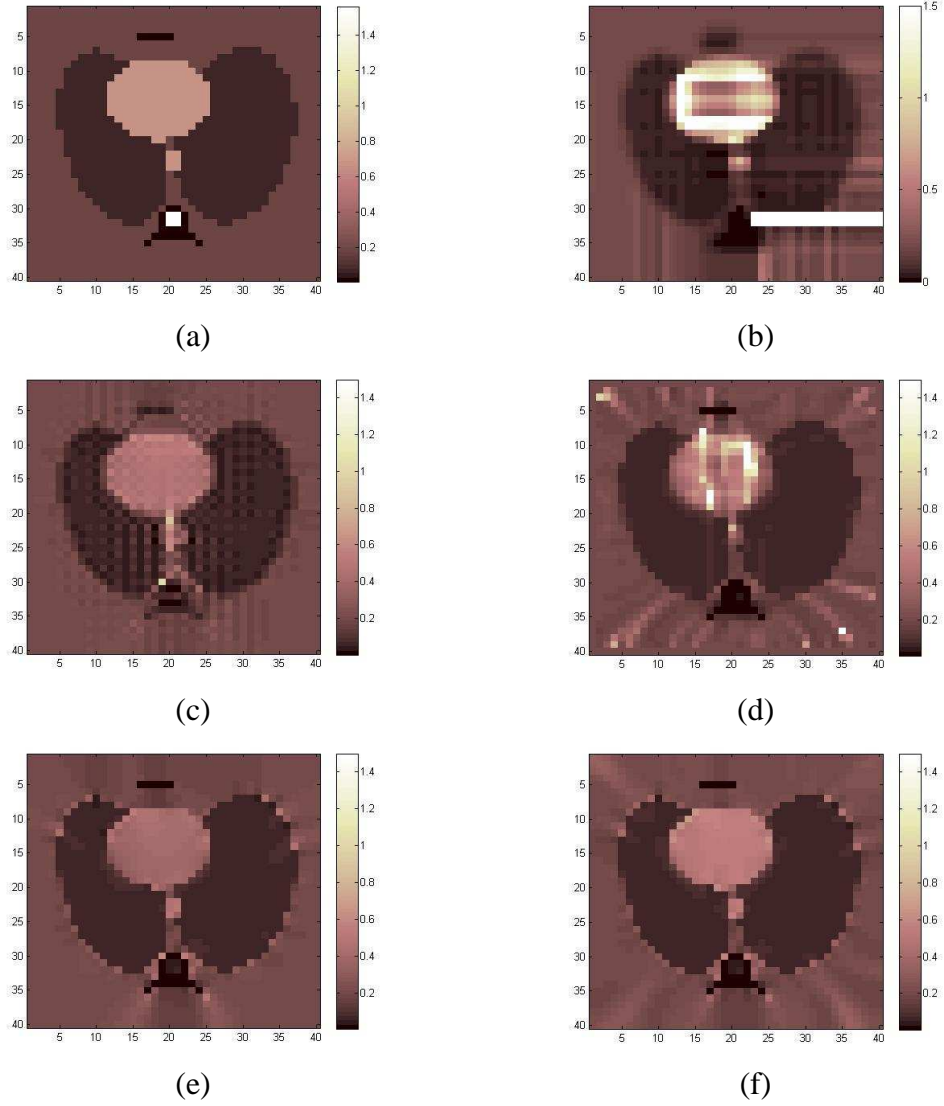


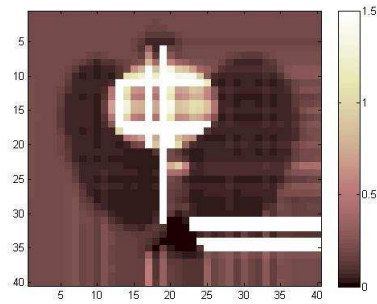
Figure 4.32 Reconstructed Images for Thorax Phantom Noise-free case a) Original Distribution, b) Integration along Cartesian Grid Lines, c) Solution as a Linear Equation System, d) Equipotential-Projection, e) J-Substitution, f) Hybrid

There are many miscalculated pixels for the case of Integration along Cartesian Grid Lines which suppresses and distorts the image. The reason behind those pixels is the boundary between the most conductive element, spinal cord, and the most resistive element, bone. Basic idea of this algorithm is integrating conductivity gradient through FOV and conductivity gradient reaches its maximum at that boundary. Therefore, errors on that boundary are carried to right for noise free case.

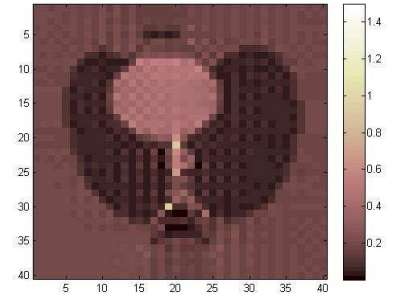
Relatively high error values for lung region and background are due to that phenomenon because error lines go through lung and background. Also, general error is affected since most of the image is formed by lung and background. Regions where these errors are not seen have moderate percentage errors, like 85% for heart and 51% for aorta.

With addition of noise, percentage errors for all regions are increased dramatically because errors due to sternum region and background boundary also spread to the image. Also, bone being the most resistive element includes the lowest current density and is affected the most from noise. Perceptually, images are more distorted and suppressed than noise free case which can be seen in Figure 4.33a and Figure 4.34a

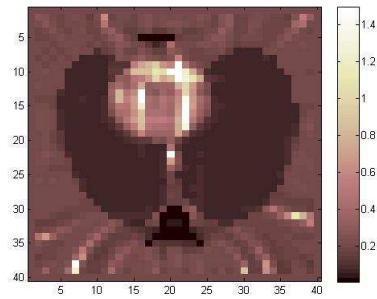
Figure 4.32c, Figure 4.33b and Figure 4.34b show reconstructed images with Solution as a Linear Equation System algorithm for noise free, SNR 30 and SNR 13 cases, respectively. Perceptually, all elements are distinguished from each other although object boundaries are not sharp. This algorithm reconstructed background with least error along with J-substitution and Hybrid algorithm. Moreover, percentage errors for heart region are lower than all algorithms except Hybrid algorithm. Although background error is around 25%, general error reaches to 140% for SNR 13. Relatively high general error is due to percentage error of bone element which has more than 1000% error for SNR 13. As Lorca [22] made it clear that Solution as a Linear Equation system algorithm includes information from four neighbor pixels for solution of a single pixel. Therefore, information for bone structure around spinal cord comes from spinal cord and forces the algorithm to calculate conductivity of bone element inaccurately.



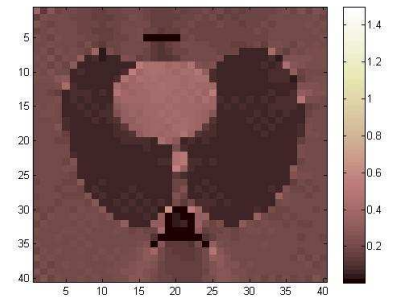
(a)



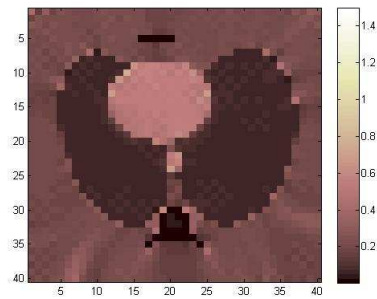
(b)



(c)



(d)



(e)

Figure 4.33 Reconstructed Images for Thorax Phantom with SNR 30 a) Integration along Cartesian Grid Lines, b) Solution as a Linear Equation System, c) Equipotential-Projection, d) J-Substitution, e) Hybrid

Addition of noise increases percentage errors of all regions but there is no other growing artifact rather than typical grid artifact.

Equipotential-Projection algorithm's results have the sharpest boundaries between all elements and all elements are separated clearly. However, artifacts in the form of erroneous lines starting from corners and continuing inside FOV and miscalculated pixels in heart region distort reconstructed images. It has a lower general error than Solution as a Linear Equation System algorithm but percentage error of background is higher due to erroneous lines in FOV.

Simulations with SNR 30 and SNR 13 have gradually increased errors for all elements as expected. Also, reconstructed images with noisy data are not distorted with respect to noise free case.

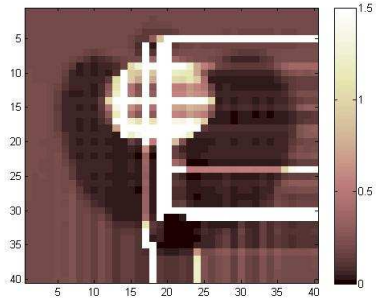
Simulation and comparison of J-Substitution and Hybrid algorithm with thorax is done in a previous study by Boyacıoğlu and Eyüboğlu [24]. Similar results are obtained in this thesis. First of all, general and lung region errors for J-Substitution are slightly lower than Hybrid algorithm. The main reason behind that is initiating Hybrid algorithm with filtered result of Equipotential-Projection algorithm. As explained above, there are erroneous lines starting from miscalculated potentials at boundaries and projected inside with equipotential lines for Equipotential-Projection algorithm. Applying a low-pass filter to the result of Equipotential-Projection algorithm reduces these artifacts but can not clear off altogether. These artifacts can be seen in Figure 4.32f, Figure 4.33e and Figure 4.34e. On the other hand, J-substitution algorithm is initiated with a homogeneous distribution which actually has a conductivity value 0.2 S/m, equal to background conductivity. As a result, background pixels are reconstructed with less error without deviation, that is they already have their true values.

There is a clear optimization for heart and aorta region errors with Hybrid algorithm with respect to J-Substitution algorithm. This improvement also shows its effect in general error. Although it is expected for Hybrid algorithm to have a higher general

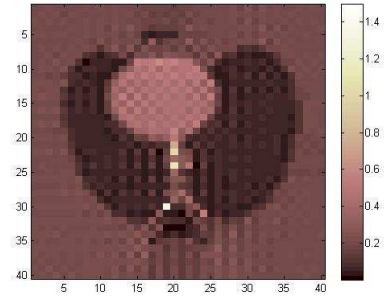
error than J-substitution algorithm, they have similar error general errors thanks to superior performance of Hybrid algorithm in heart region.

Dramatic increase in bone region error, especially for SNR 13, for both algorithms is related with relatively low current density in that region since added noise affects these areas more. Increase in noise level forces the images to distort but object boundaries are still sharp.

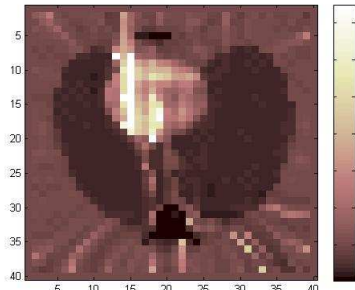
In conclusion, Hybrid algorithm reconstructs elements at the centre of the FOV, heart region in thorax phantom, better than J-Substitution algorithm. Nevertheless, these two algorithms reconstructed images with the least errors both for noise free and noisy cases. Furthermore, they produced sharper boundaries and images for noisy cases are not distorted as much as other algorithms perceptually.



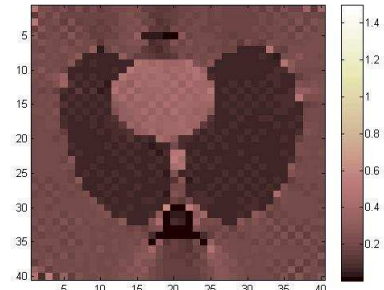
(a)



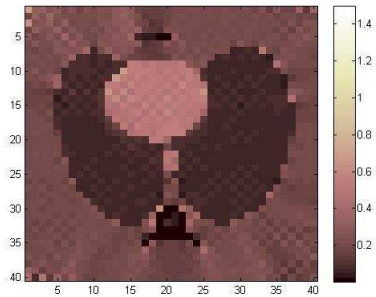
(b)



(c)



(d)



(e)

Figure 4.34 Reconstructed Images for Thorax Phantom with SNR 13 a) Integration along Cartesian Grid Lines, b) Solution as a Linear Equation System, c) Equipotential-Projection, d) J-Substitution, e) Hybrid

Table 4.3 General and Regional Percentage Errors for Simulations with Thorax Phantom

	<b>Lung (%)</b>	<b>Heart (%)</b>	<b>Bone (%)</b>	<b>CSF (%)</b>	<b>Aorta (%)</b>	<b>Background (%)</b>	<b>Total error (%)</b>
<b>Integration along Cartesian Grid Lines</b>							
<b>Noise-free</b>	9.17*10 <sup>8</sup>	85.04	736.48	100	51.45	8.15*10 <sup>8</sup>	8.08*10 <sup>8</sup>
<b>SNR 30</b>	5.17*10 <sup>8</sup>	2.78*10 <sup>3</sup>	6.47*10 <sup>3</sup>	99.99	49.54	4.52*10 <sup>8</sup>	4.52*10 <sup>8</sup>
<b>SNR 13</b>	5.78*10 <sup>10</sup>	9.69*10 <sup>4</sup>	2.53*10 <sup>5</sup>	99.99	423.37	4.6*10 <sup>18</sup>	3.45*10 <sup>18</sup>
<b>Solution as a Linear Equation System</b>							
<b>Noise-free</b>	57.98	30.34	969	96.47	37.76	24.31	122.7
<b>SNR 30</b>	54.25	34.6	920	97.22	39.88	24.23	116.63
<b>SNR 13</b>	64.12	34.48	1117	96.69	57	27.9	141.03
<b>Equipotential-Projection</b>							
<b>Noise-free</b>	17.71	70.71	125.93	98.23	55.04	58.1	51.84
<b>SNR 30</b>	20.65	161.43	153.44	98	119.75	48.34	63.47
<b>SNR 13</b>	88.61	99.29	241.98	98.55	69.12	57.76	78.66
<b>J-Substitution</b>							
<b>Noise-free</b>	12.1	40.93	60.89	97.31	31.66	21.13	22.8
<b>SNR 30</b>	13.53	41.35	77.43	97.72	31.32	22.04	24.29
<b>SNR 13</b>	17.66	42.56	214.41	97.04	31.23	26.19	36.45
<b>Hybrid</b>							
<b>Noise-free</b>	16.67	22.03	54.3	97.45	25.86	23.5	22.65
<b>SNR 30</b>	19.3	21.48	77.47	97.9	21.62	23.57	24.24
<b>SNR 13</b>	22.34	23.64	245	97.23	30.3	28.95	39.69

## 4.5.6 Experimental Data

### 4.5.6.1 Experiment 1

Experimental data is collected as explained in Section 2.5, Section 4.2.6 and Appendix A. For experiment 1, conductivity values of background, circle and square elements are 0.2, 0.4 and 0.1 S/m. Since, simulations include two current injection profiles, experimental data is collected both for vertical and horizontal current injection profiles. As a result, every slice is imaged twice, one for vertical and one for horizontal current injection. Governing equations for calculation of  $J_x$  and  $J_y$  can be seen in Equation (4.3) and (4.4), respectively.

$$J_x = \frac{1}{\mu_0} \left( \frac{\partial B_z}{\partial y} - \frac{\partial B_y}{\partial z} \right) \quad (4.3)$$

$$J_y = \frac{1}{\mu_0} \left( \frac{\partial B_x}{\partial z} - \frac{\partial B_z}{\partial x} \right) \quad (4.4)$$

where  $\mu_0$  is the permeability of free-space.

First,  $B_z$  is obtained. Here, slice selection gradient is in  $z$  direction. Two phase images are taken for both current injection profiles, which are with positive and negative current injection for every slice. Phase images of  $z$  slice for vertical current injection can be seen in Figure 4.35 and Figure 4.36. Then, these phase images are masked to remove recessed electrodes. Masked phase images are unwrapped, and  $B_z$  is calculated as explained in Section 2.5.  $B_z$  images for vertical and horizontal current injection profiles can be seen in Figure 4.37 and Figure 4.38, respectively.

Next step is the calculation of derivatives of  $B_z$  with respect to  $x$  and  $y$  directions for both vertical and horizontal current injection patterns using Sobel operators which are illustrated in Figure 4.39, Figure 4.40, Figure 4.41 and Figure 4.42, respectively.

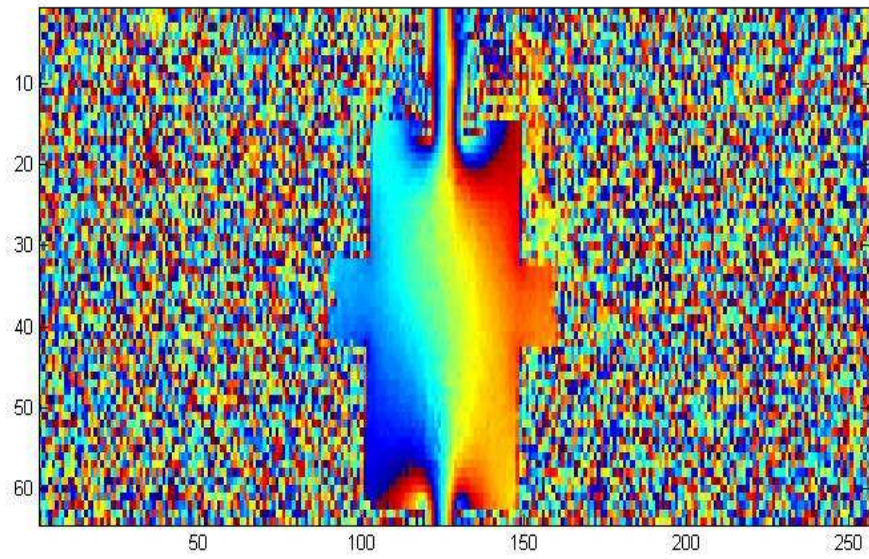


Figure 4.35 Phase image of  $z$  slice for vertical and negative current injection.

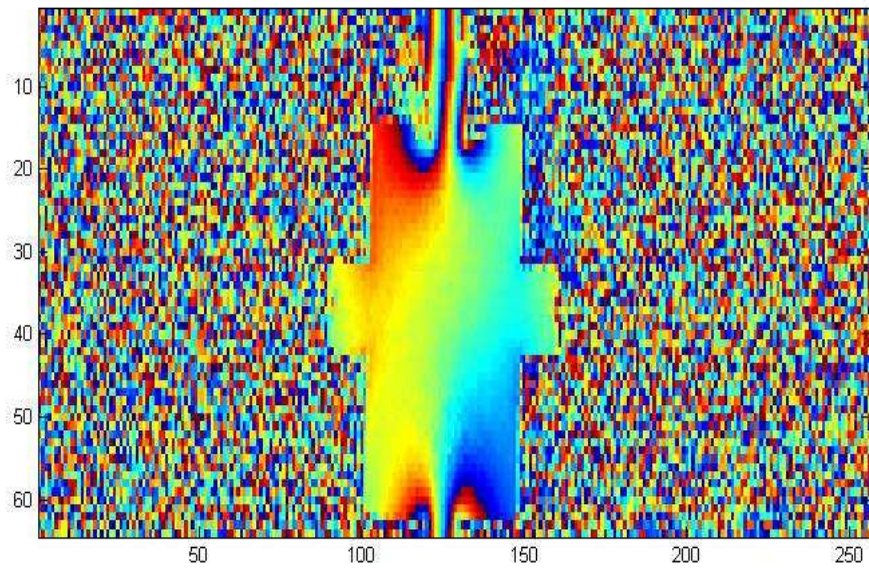


Figure 4.36 Phase image of  $z$  slice for vertical and positive current injection.

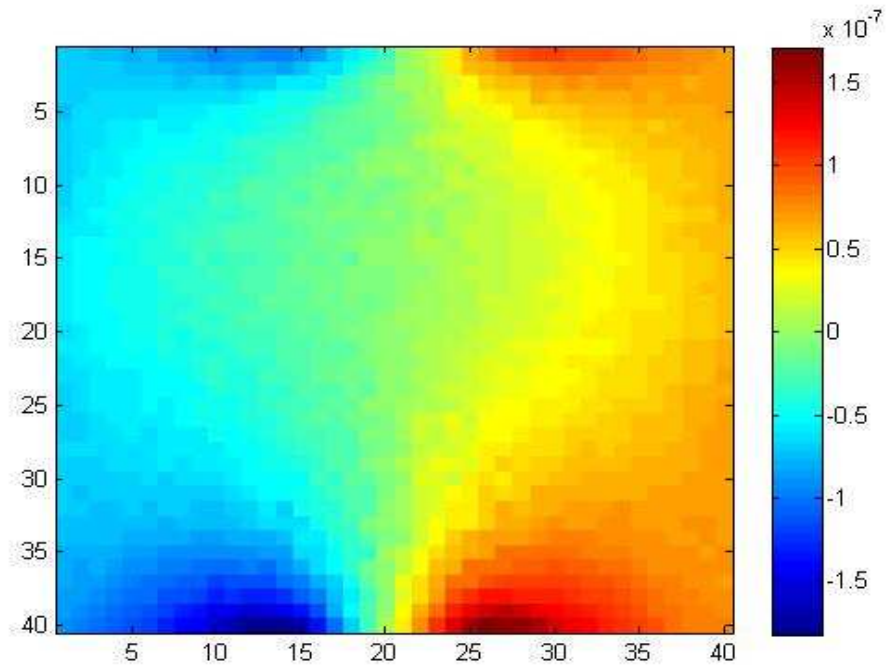


Figure 4.37  $B_z$  image for vertical current injection, in units of Tesla

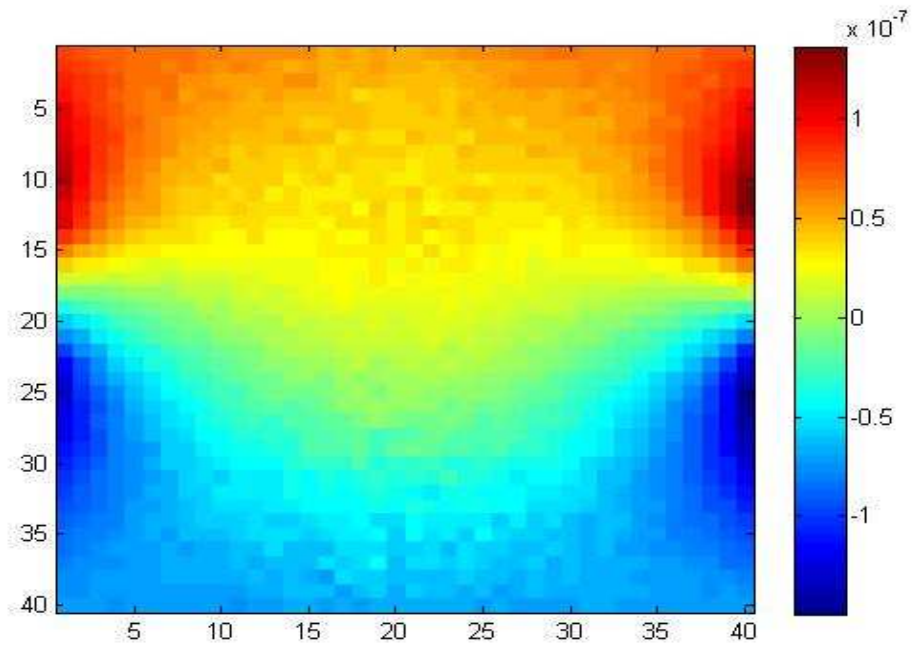


Figure 4.38  $B_z$  image for horizontal current injection, in units of Tesla.

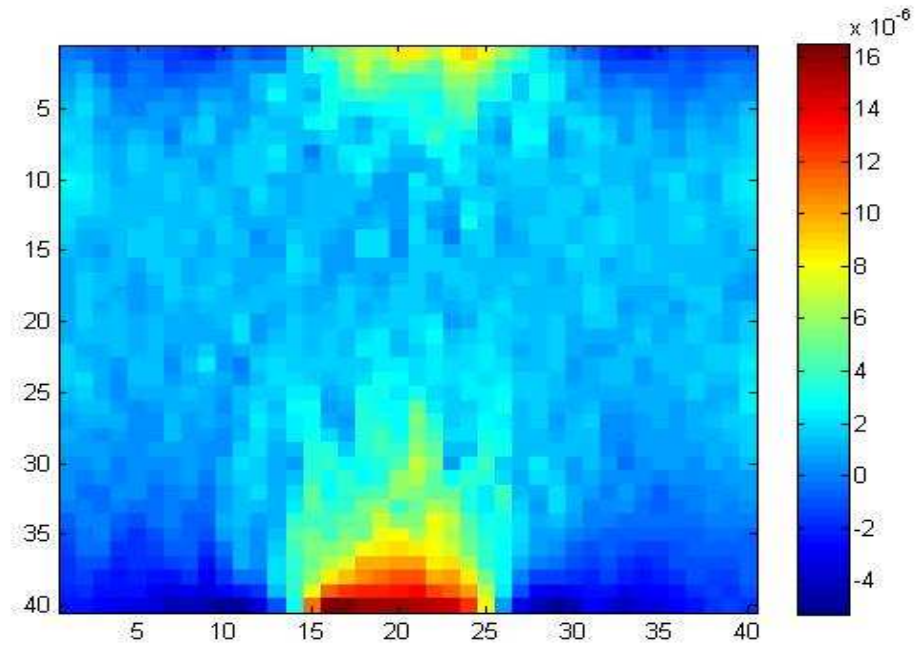


Figure 4.39 Derivative of  $B_z$  (T/m) with respect to  $x$  direction for vertical current injection

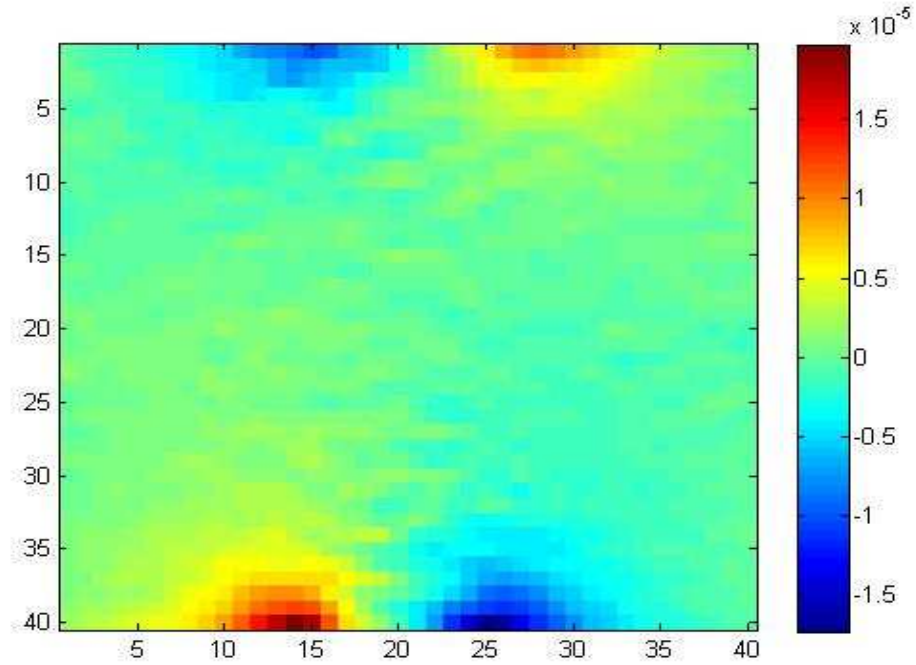


Figure 4.40 Derivative of  $B_z$  (T/m) with respect to  $y$  direction for vertical current injection

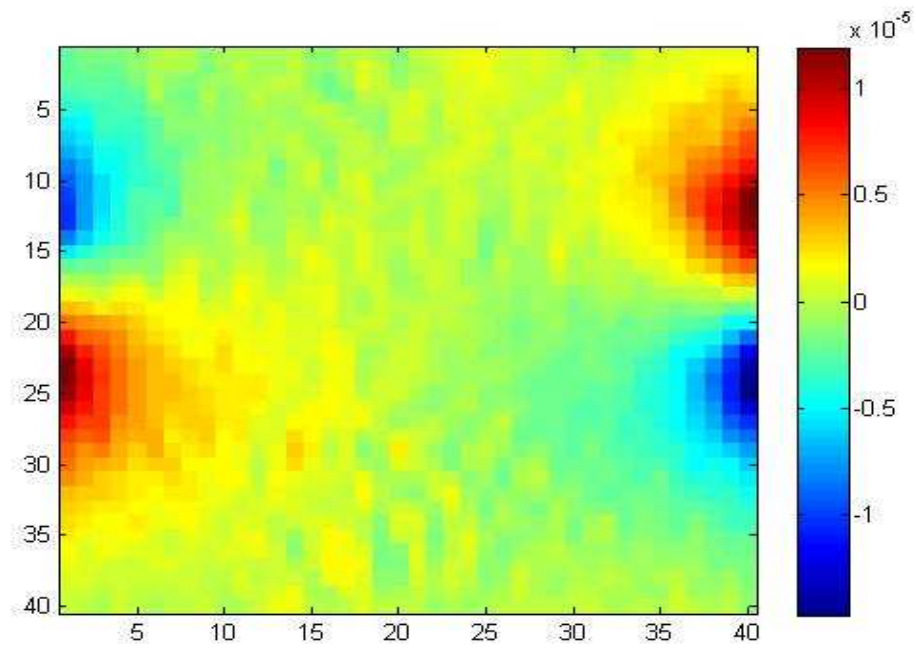


Figure 4.41 Derivative of  $B_z$  (T/m) with respect to  $x$  direction for horizontal current injection

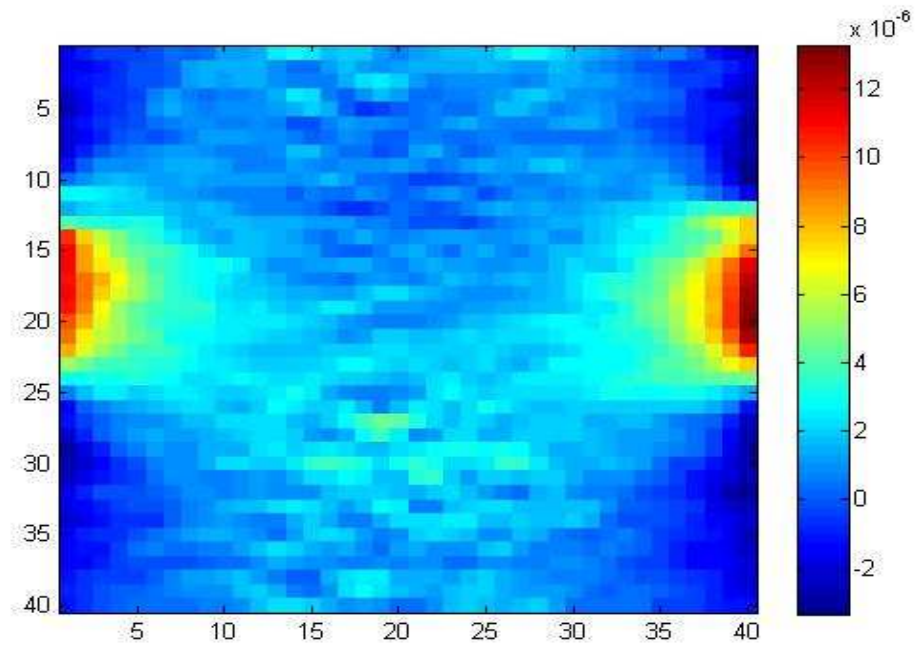


Figure 4.42 Derivative of  $B_z$  (T/m) with respect to  $y$  direction for horizontal current injection

To calculate  $J_x$ , derivative of  $B_y$  with respect to  $z$  direction is also needed. So, experimental phantom is oriented inside RF coil in a way such that  $y$  direction of the phantom is in the  $B_0$  direction. In that case, slice selection gradient is in  $y$  direction. Then, two off-slices in  $z$  direction are imaged. They are masked and unwrapped. After magnetic field is calculated for both off-slices, derivative of  $B_y$  with respect to  $z$  direction is calculated with forward difference.  $\frac{\partial B_y}{\partial z}$  is illustrated in Figure 4.43 and Figure 4.44 for vertical and horizontal current injection profiles, respectively.

The same procedure is applied for calculation of  $\frac{\partial B_x}{\partial z}$  which is shown in Figure 4.45 and Figure 4.46, for vertical and horizontal current injection profiles, respectively.

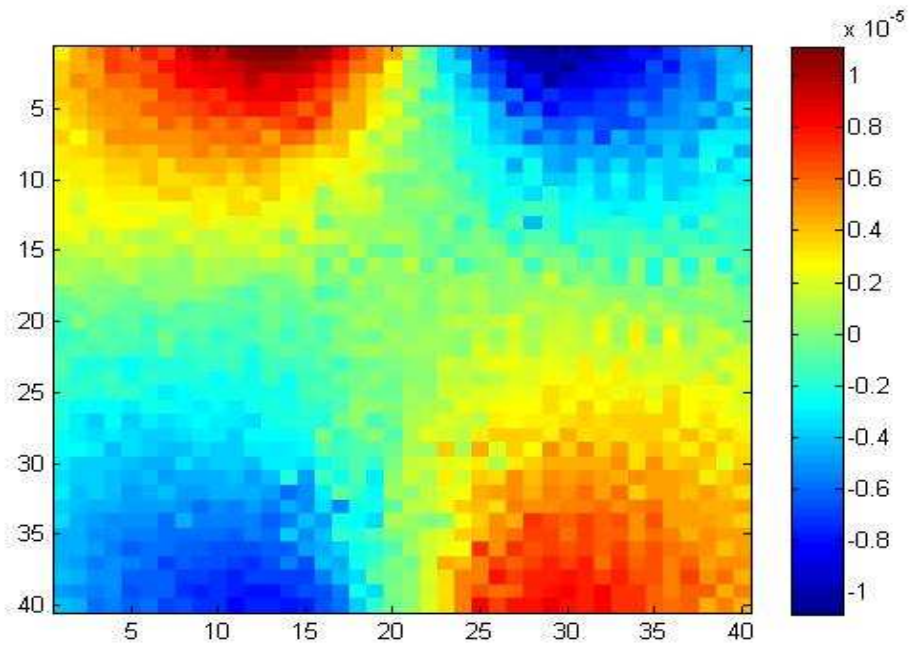


Figure 4.43  $\frac{\partial B_y}{\partial z}$  (T/m) image for vertical current injection

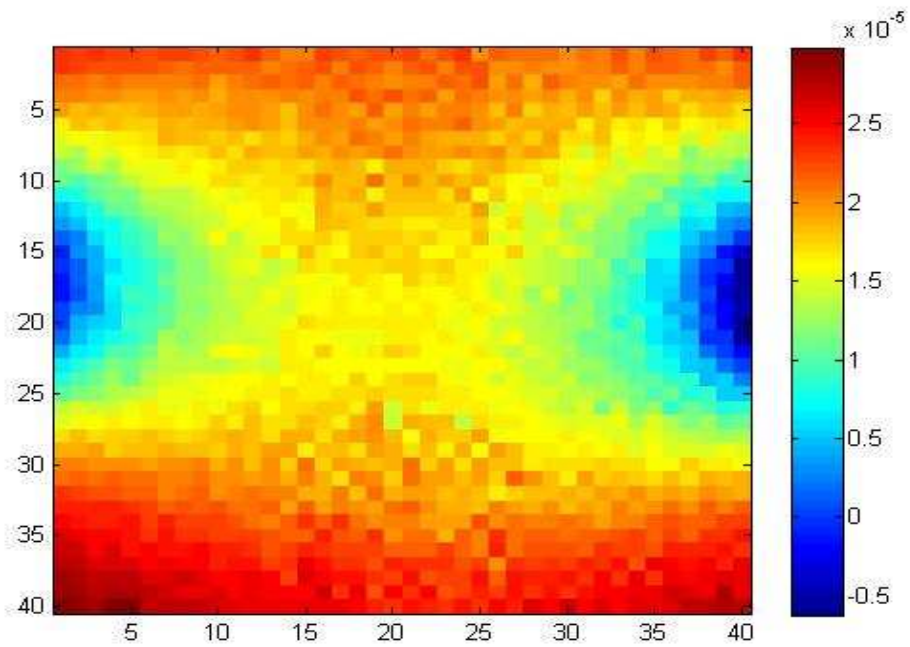


Figure 4.44  $\frac{\partial B_y}{\partial z}$  (T/m) image for horizontal current injection

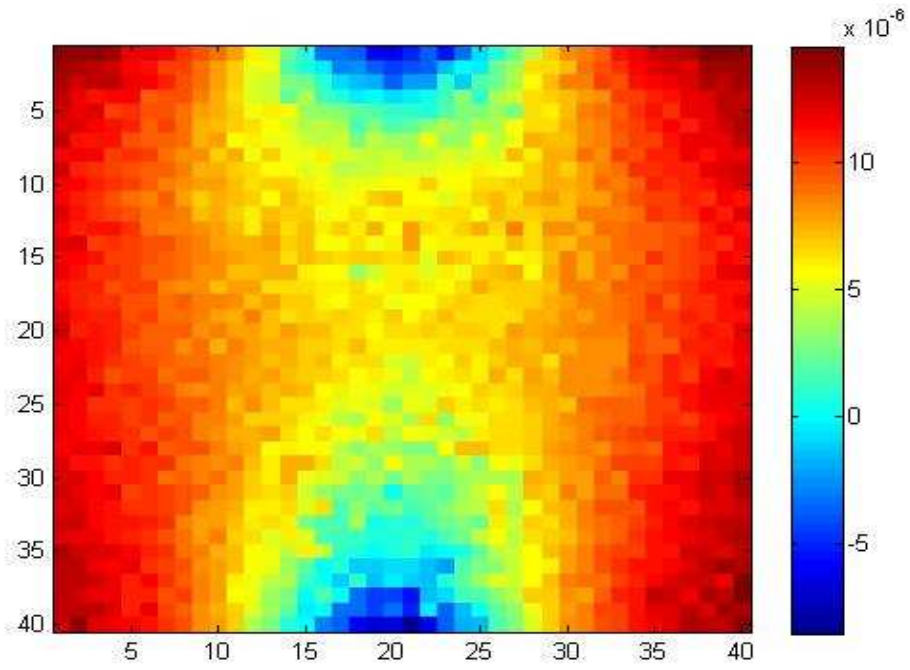


Figure 4.45  $\frac{\partial B_x}{\partial z}$  (T/m) image for vertical current injection

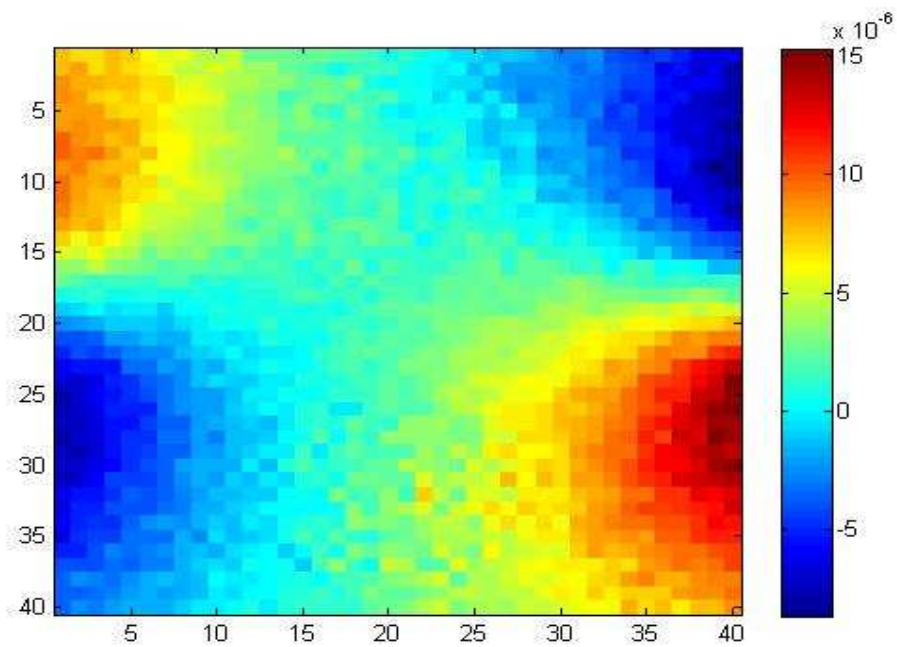


Figure 4.46  $\frac{\partial B_x}{\partial z}$  (T/m) image for horizontal current injection

$J_x$  and  $J_y$  are calculated with Equation (4.3) and (4.4), respectively. Figure 4.47 and Figure 4.48 includes current density distributions for vertical current injection in  $x$  and  $y$  directions, respectively. Moreover, current density distributions of horizontal current injection are shown in Figure 4.49 and Figure 4.50. Next step is the calculation of total current density,  $J$ , with Equation (4.5).

$$J = \sqrt{J_x^2 + J_y^2} \quad (4.5)$$

Total current density distributions for vertical and horizontal current injection are shown in Figure 4.51 and Figure 4.52, respectively. Also, arrow plots of current densities of vertical and horizontal current injection are shown in Figure 4.53 and Figure 4.54, respectively, to give an idea about the path and magnitude of current density distributions.

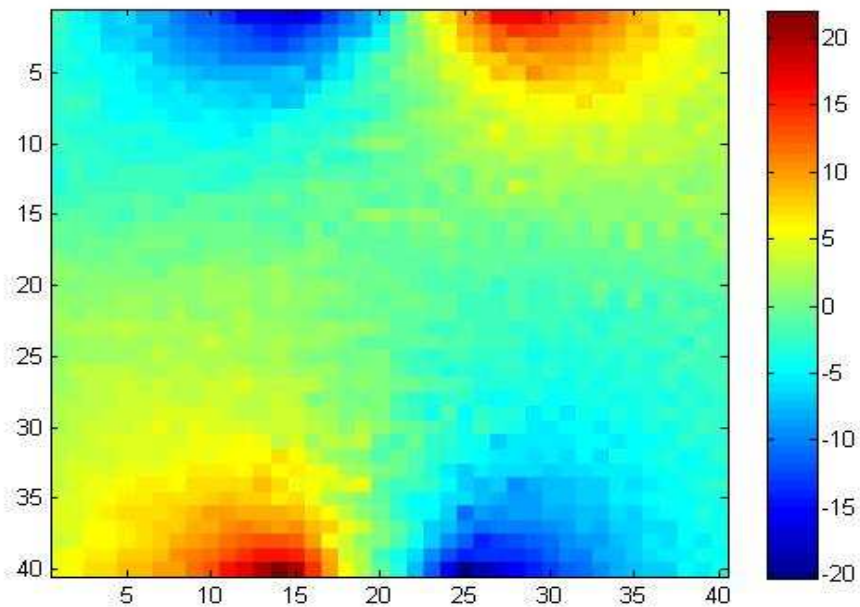


Figure 4.47  $J_x$  ( $A/m^2$ ) image for vertical current injection

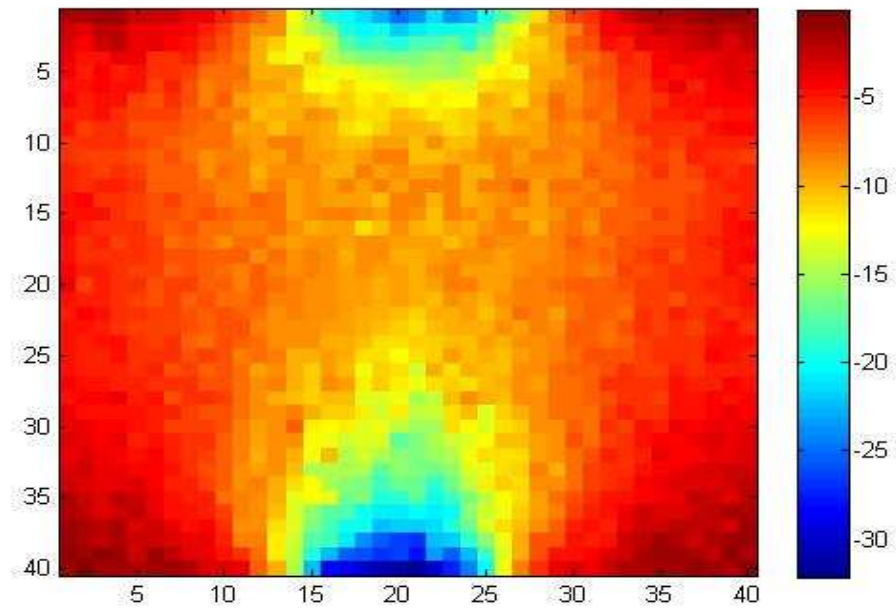


Figure 4.48  $J_y$  ( $A/m^2$ ) image for vertical current injection

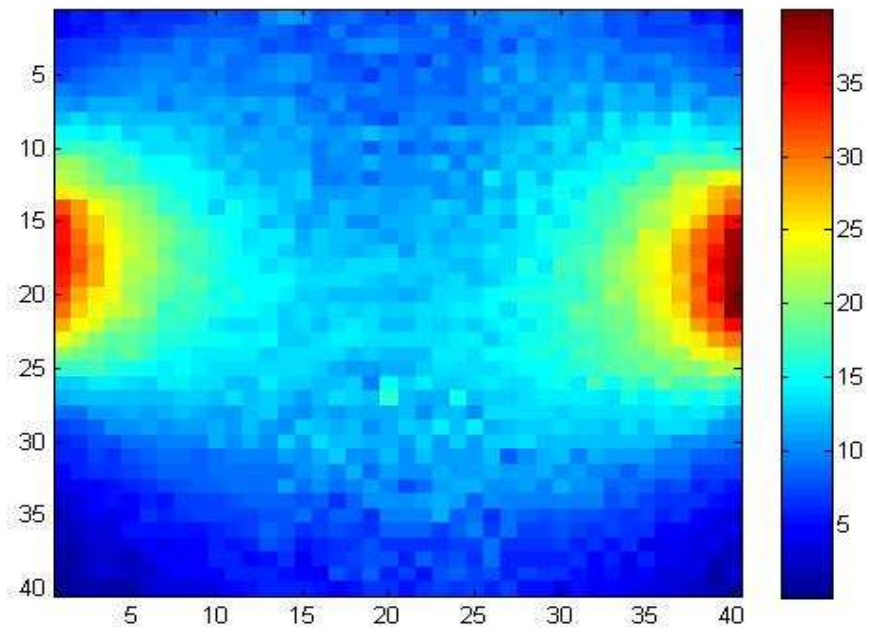


Figure 4.49  $J_x$  ( $A/m^2$ ) image for horizontal current injection

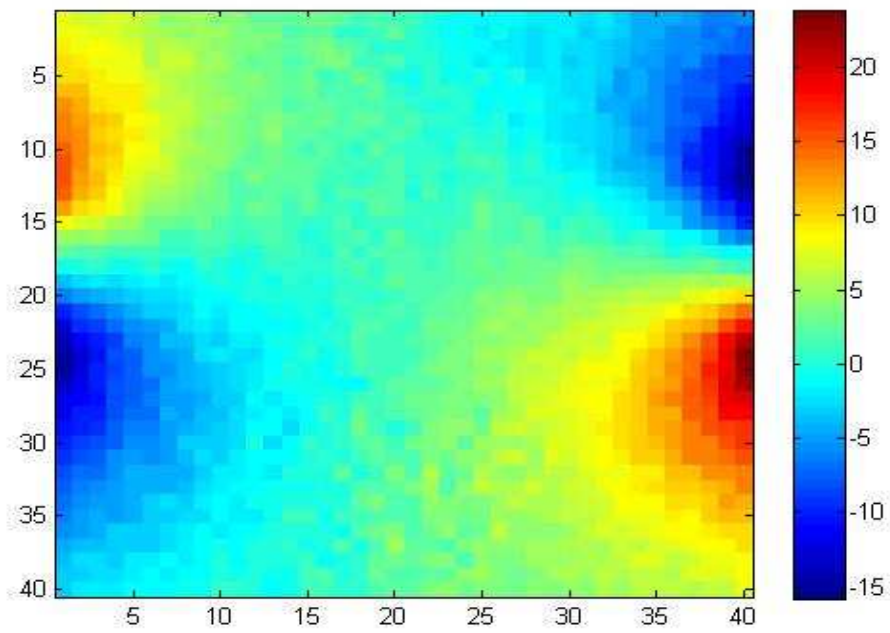


Figure 4.50  $J_y$  ( $A/m^2$ ) image for horizontal current injection

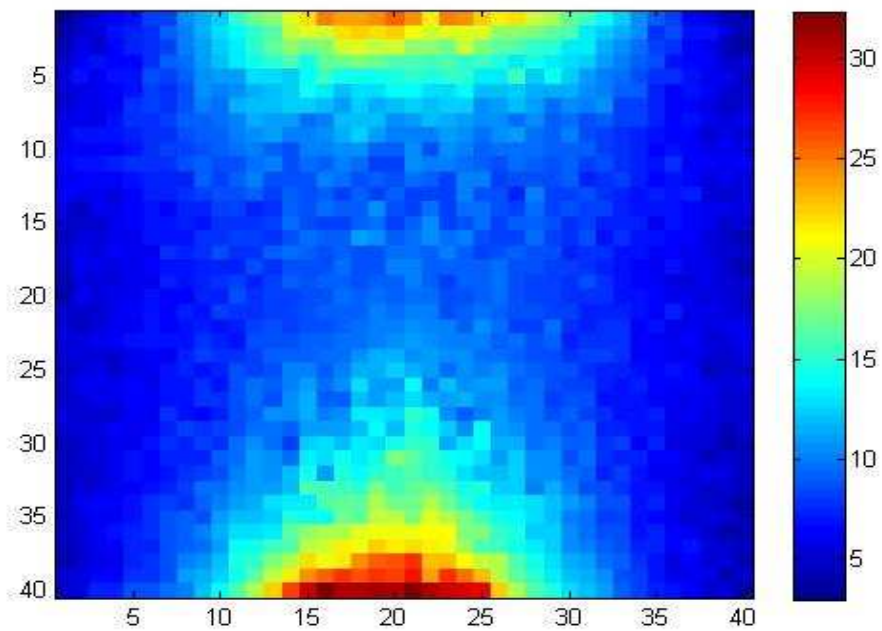


Figure 4.51  $J$  ( $A/m^2$ ) image for vertical current injection

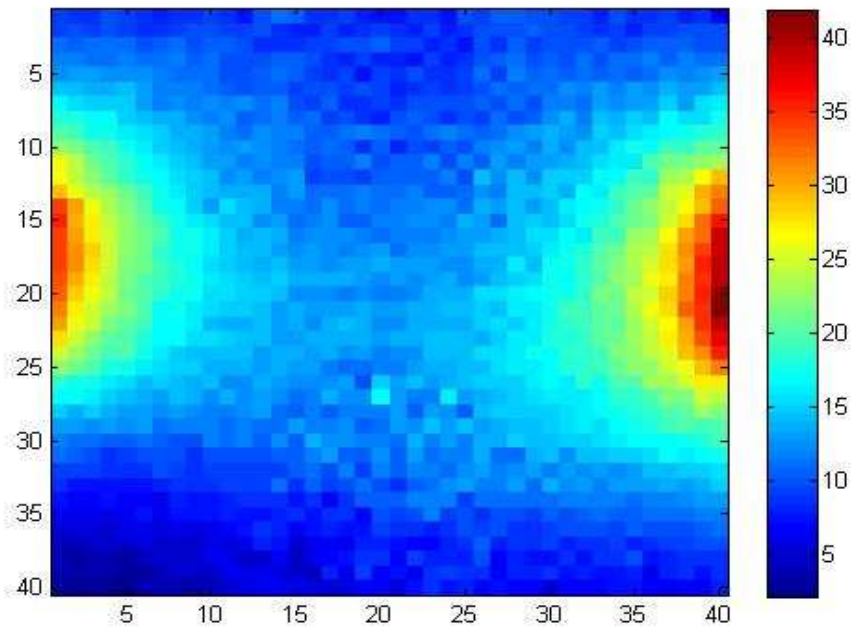


Figure 4.52  $J$  ( $A/m^2$ ) image for horizontal current injection

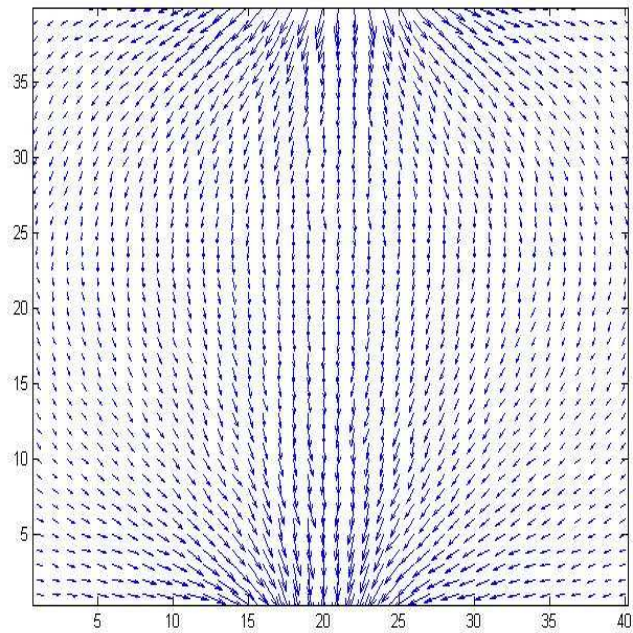


Figure 4.53 Arrow Plot for Current Density Distribution of Vertical Current Injection

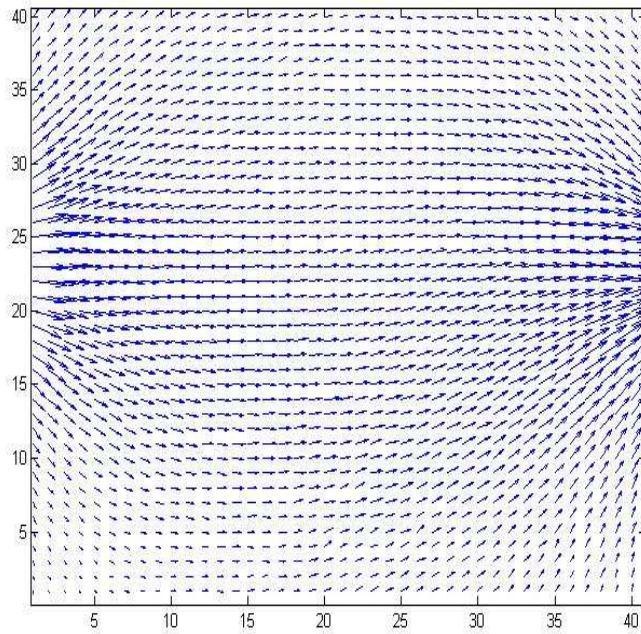
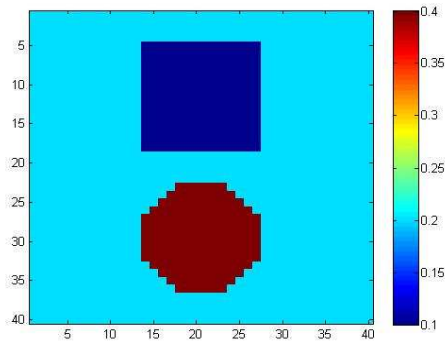
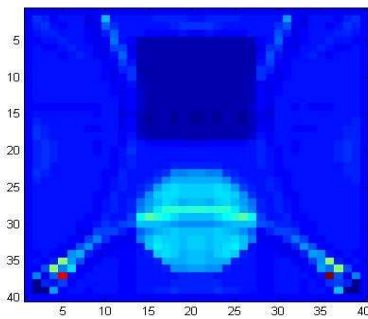


Figure 4.54 Arrow Plot for Current Density Distribution of Horizontal Current Injection

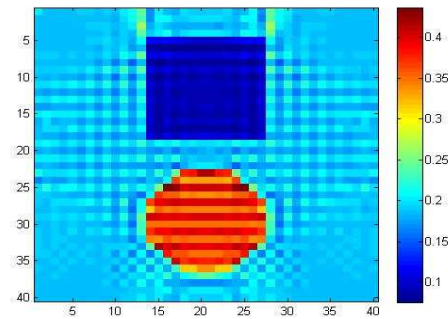
After current density distributions,  $J_x$ ,  $J_y$  and  $J$ , for both current injection patterns are obtained reconstruction algorithms are fed with these experimental data. First, reconstructed images obtained with simulation data will be given to be able to make a comparison between experimental and simulation results. Figure 4.55 illustrates original conductivity distribution and reconstructed images with simulation with experiment 1 parameters. Similar artifacts and performances continue. Equipotential-Projection and solution as a Linear Equation System algorithms have their typical erroneous lines and grid artifact, respectively. However, for both algorithms circle and square elements are separated from background and have sharp boundaries. J-Substitution and Hybrid algorithms are still superior and Hybrid algorithm suffer from the erroneous lines of Equipotential-Projection algorithm.



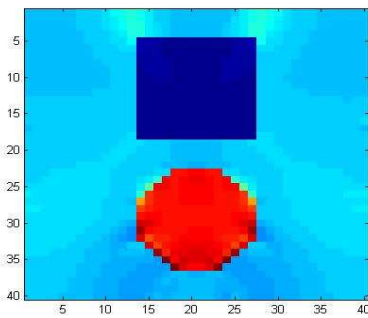
(a)



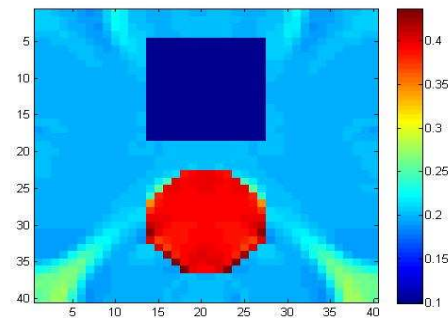
(b)



(c)



(d)



(e)

Figure 4.55 Reconstructed Images with Simulated Data for Experiment 1, a) Original Distribution, b) Equipotential-Projection, c) Solution as a Linear Equation System, d) J-Substitution (3 iteration), e) Hybrid (3 iteration)

Result obtained with Equipotential-Projection for data of experiment 1 is shown in Figure 4.56. Moreover, low-pass filtered version of the result of Equipotential-Projection algorithm is shown in Figure 4.57. Square element which is more resistive than background is slightly distinguished although its boundaries are not clear. On the other hand, circle element's boundaries can be recognized. However, there are erroneous lines distorting the reconstructed image which are initiated from corners of FOV. Origins of these artifacts can be seen in Figure 4.58 and Figure 4.59 which include the conductivity distributions reconstructed with only vertical and horizontal current injections, respectively. When filtered conductivity distribution in Figure 4.57 is analyzed, boundaries of square element are clearer than the original reconstructed conductivity distribution.

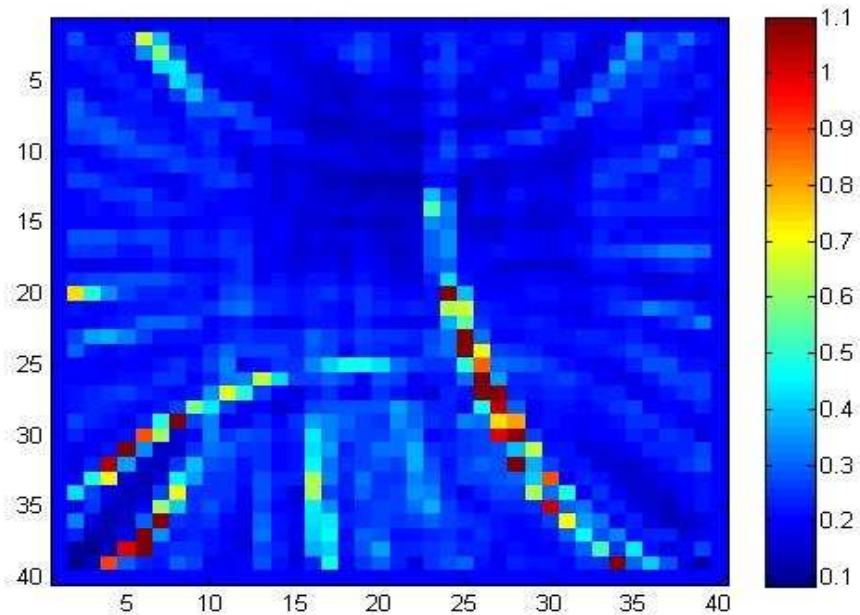


Figure 4.56 Reconstructed Conductivity (S/m) for Experimental Data with Equipotential-Projection Algorithm

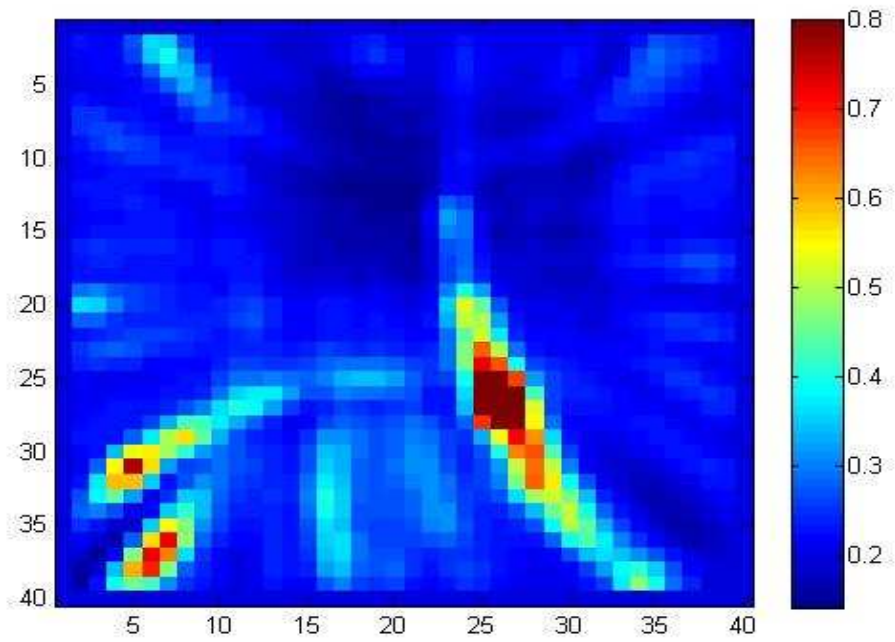


Figure 4.57 Filtered Version of Reconstructed Conductivity (S/m) with Equipotential-Projection Algorithm

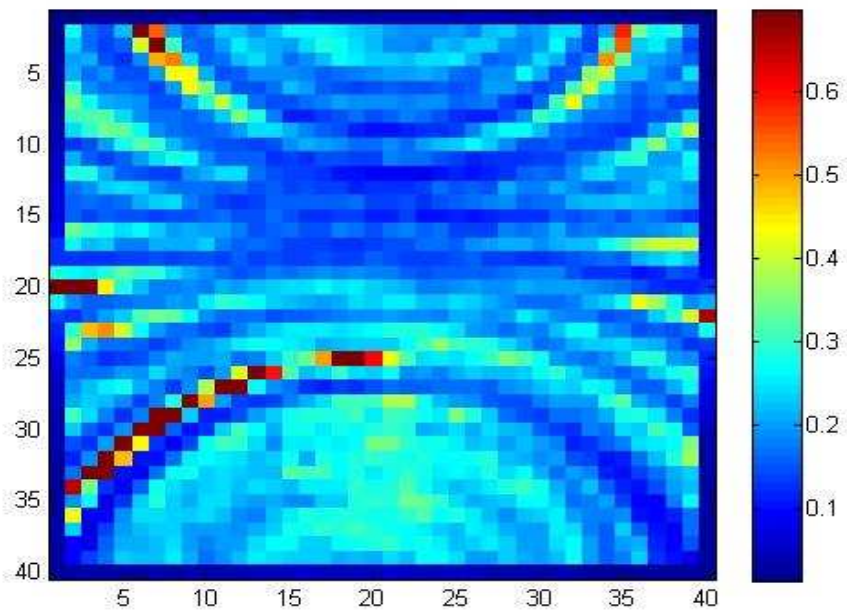


Figure 4.58 Reconstructed Conductivity (S/m) for Experimental Data of Vertical Current Injection with Equipotential-Projection Algorithm

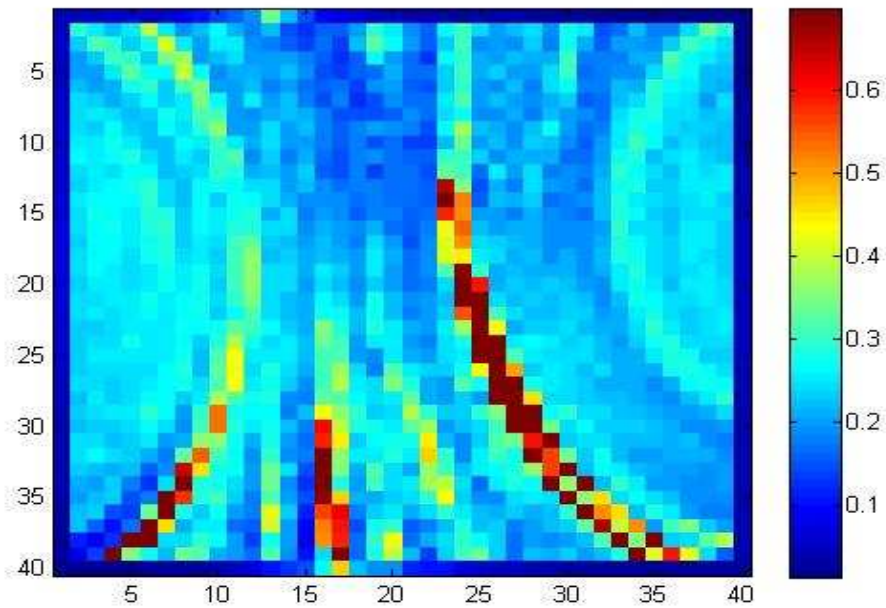


Figure 4.59 Reconstructed Conductivity (S/m) for Experimental Data of Horizontal Current Injection with Equipotential-Projection Algorithm

Filtered conductivity distribution of Equipotential-Projection algorithm is set as the initial conductivity distribution for Hybrid algorithm. Result obtained with Hybrid algorithm for experimental data is shown in Figure 4.60. Since corners of FOV contain lower amount of current density with respect to other regions, effect of noise becomes dominant in these regions. The same conclusion is deduced from simulation results. When result of Hybrid algorithm is compared with result of Equipotential-Projection algorithm, square element can not be reconstructed. However, circle element is separated from background with Hybrid algorithm.

J-Substitution algorithm has a similar performance as Hybrid algorithm with the difference that erroneous lines are not seen in the reconstructed conductivity distribution. Reconstructed conductivity with J-substitution algorithm is shown in Figure 4.61

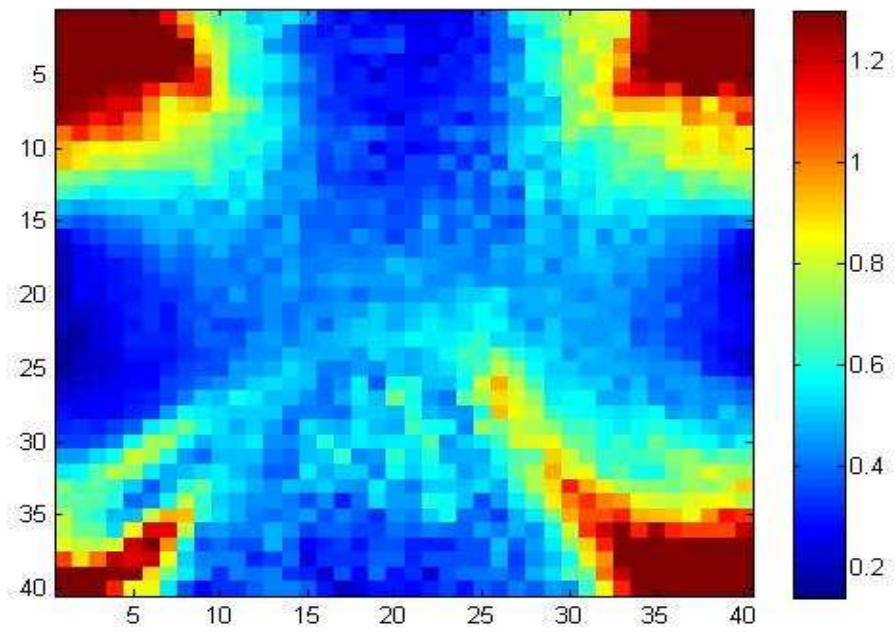


Figure 4.60 Reconstructed Conductivity Distribution (S/m) with Hybrid Algorithm

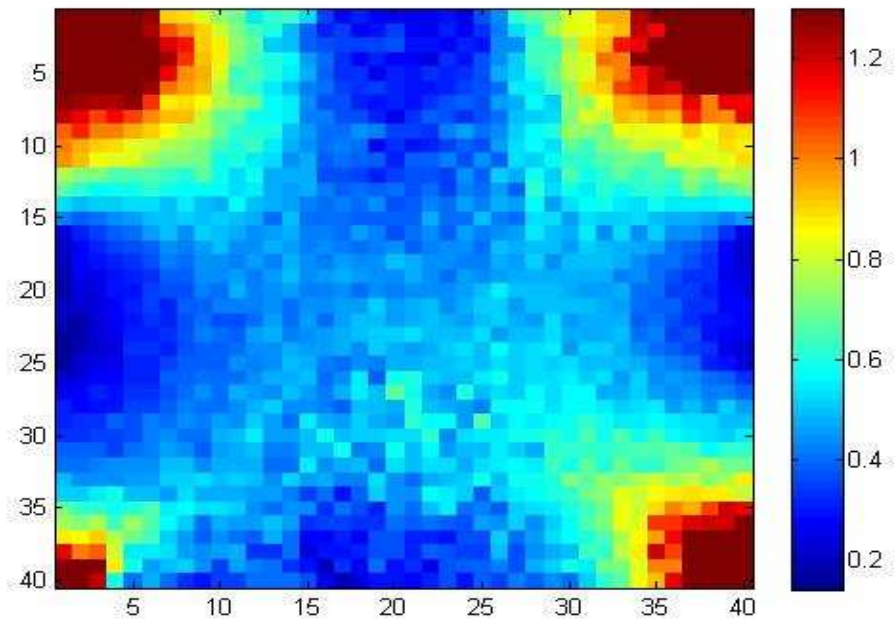


Figure 4.61 Reconstructed Conductivity Distribution (S/m) with J-Substitution Algorithm

Solution as a Linear Equation System algorithm is also fed with experimental data and its result can be seen in Figure 4.62. Solution as a Linear Equation System algorithm has the best performance perceptually with data of experiment 1 since it reconstructed both square and circle elements although boundaries are not clear. Simulation results showed that this algorithm was robust to noise and it is proven here, too. In the simulation results, Solution as a Linear Equation System algorithm has relatively higher percentage errors with simulations of models with high conductivity contrast. However, experimental phantom's conductivity contrast value is two both for resistive square and conductive circle element.

Integration along Equipotential Lines and Integration along Cartesian Grid Lines algorithms failed to reconstruct conductivity distribution with experimental data. They can not reconstruct conductivity distribution with simulations of SNR 13 noise level, either.

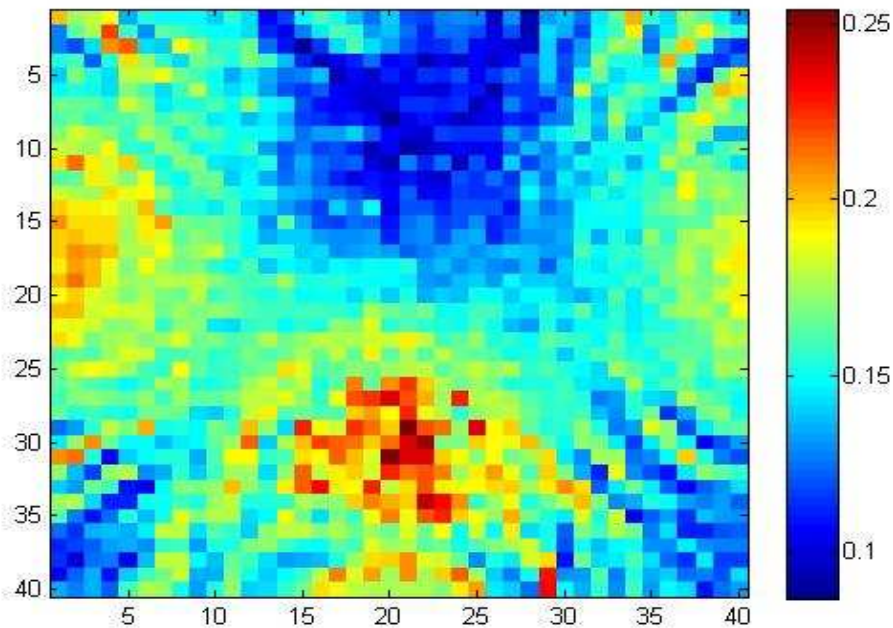


Figure 4.62 Reconstructed Conductivity Distribution (S/m) with Solution as a Linear Equation System Algorithm

In conclusion, Equipotential-Projection and Solution as a Linear Equation System algorithms reconstructed conductivity distribution partially. On the other hand, J-Substitution and Hybrid algorithm suffer from relatively high noise effect especially at the corners of FOV. Integration along Cartesian Grid Lines and Integration along Equipotential Lines algorithms can not reconstruct conductivity distribution with experimental data. When experimental and simulation results are compared for all algorithms, another experiment with a higher conductivity contrast is essential since none of the algorithms reconstructed both elements clearly.

#### **4.5.6.2 Experiment 2**

Another experiment is conducted to see the effect of conductivity contrast on reconstructed images. In this experiment, phantom geometry is kept the same while conductivity of the circle element is increased to 1.9 S/m and the square element is designed as a pure insulator. In Figure 4.63 and Figure 4.64,  $J_x$  and  $J_y$  components of vertical current injection pattern can be seen. Moreover,  $J_x$  and  $J_y$  of horizontal current injection are also shown in Figure 4.65 and Figure 4.66. Arrow plot illustration of both current injection patterns can be seen in Figure 4.67.

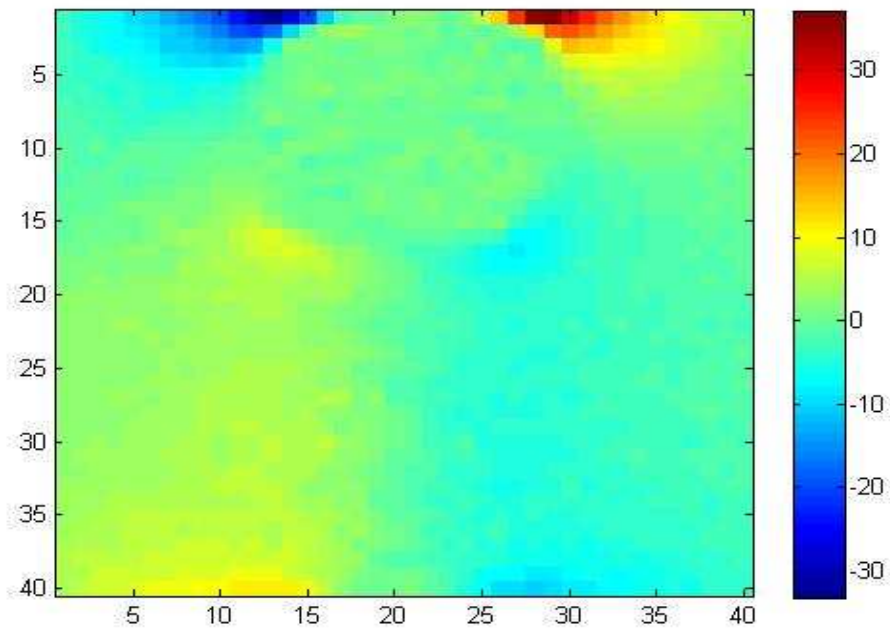


Figure 4.63  $J_x$  ( $A/m^2$ ) Image For Vertical Current Injection, Experiment 2

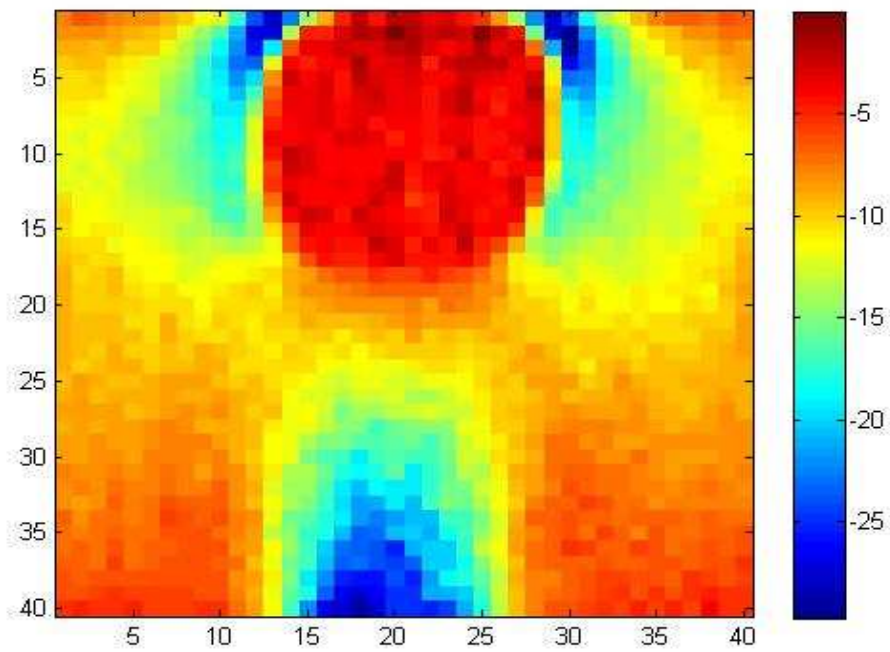


Figure 4.64  $J_y$  ( $A/m^2$ ) Image For Vertical Current Injection, Experiment 2

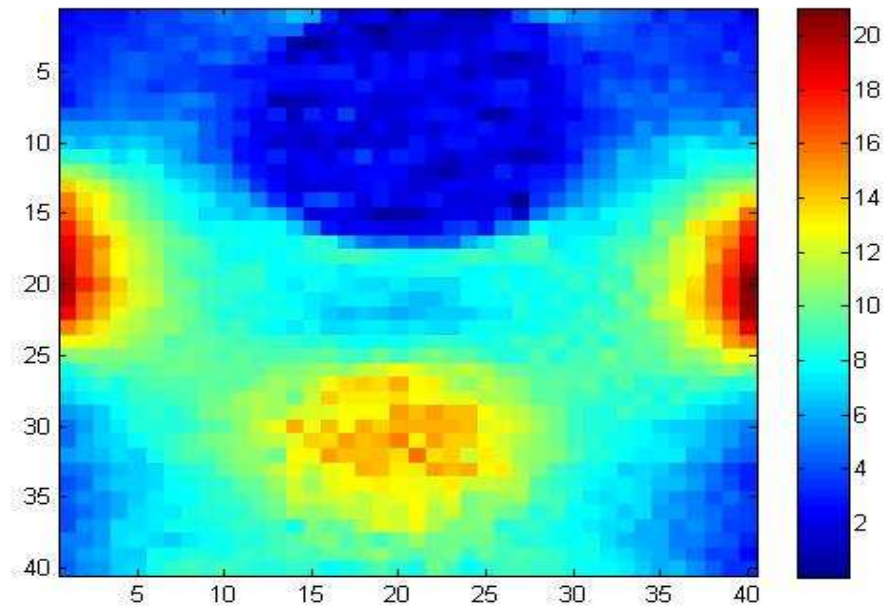


Figure 4.65  $J_x$  ( $A/m^2$ ) Image For Horizontal Current Injection, Experiment 2

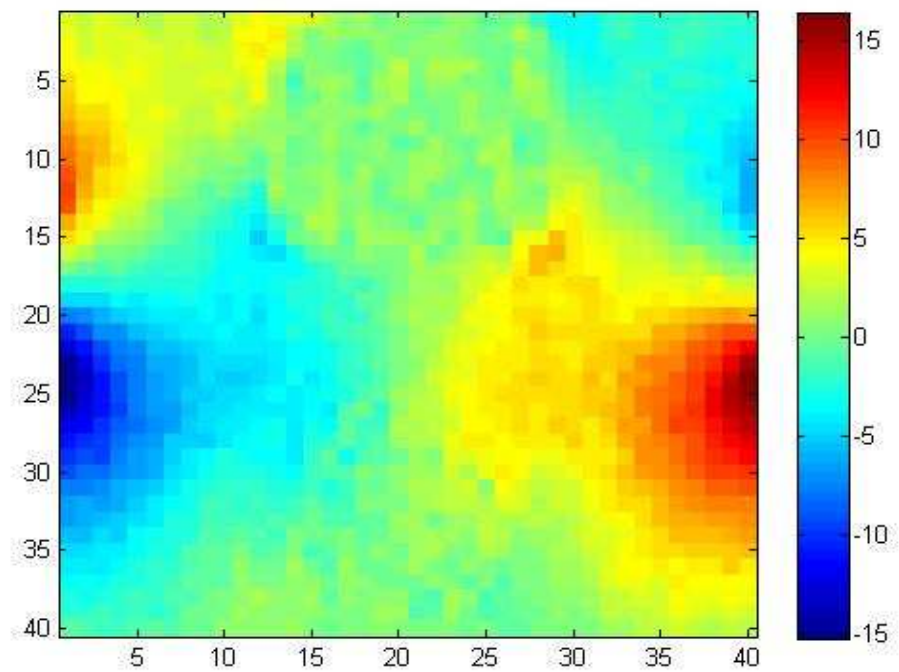
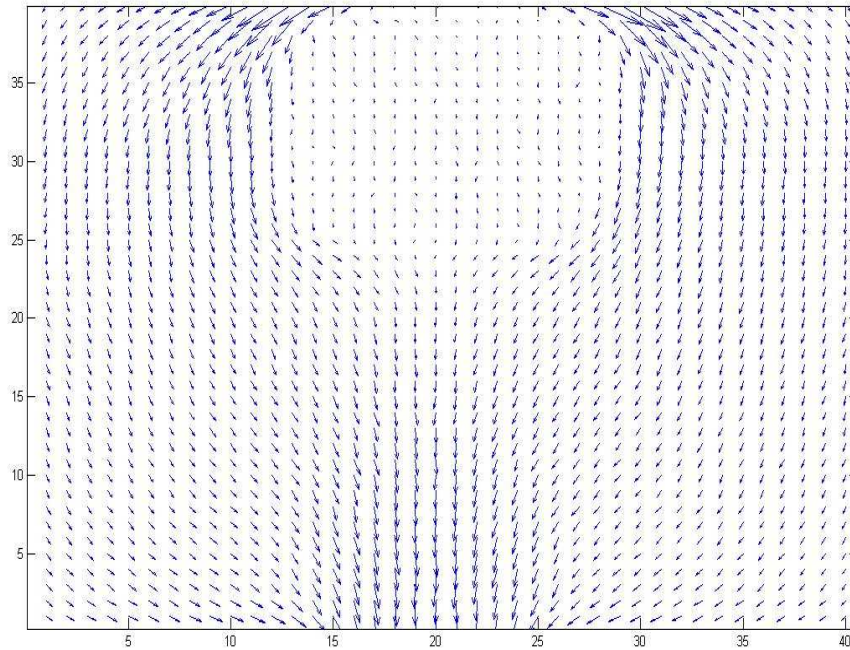
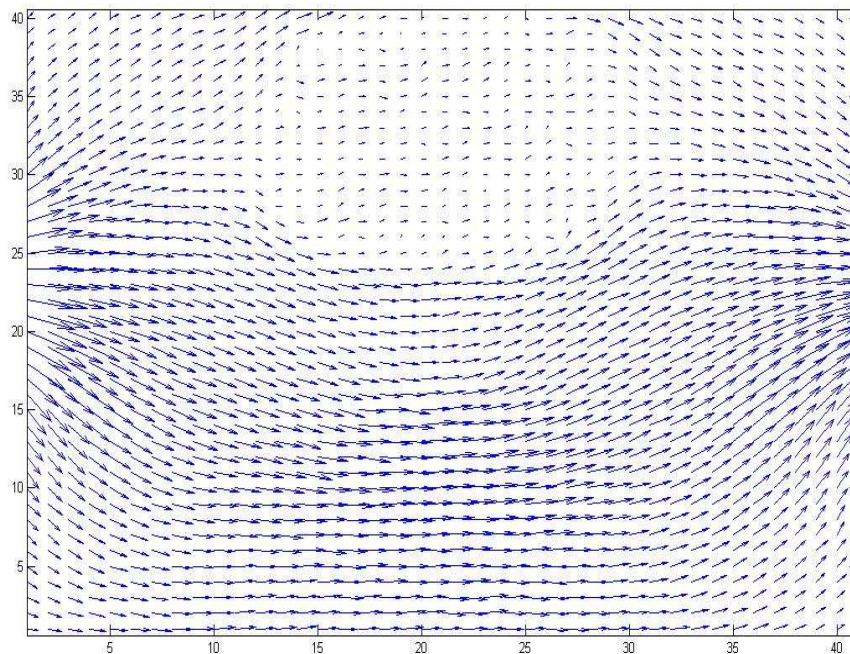


Figure 4.66  $J_y$  ( $A/m^2$ ) Image For Horizontal Current Injection, Experiment 2



(a)



(b)

Figure 4.67 Arrow Plots for current density a) Vertical Injection, b)Horizontal Injection

As can be seen in Figure 4.67, both objects are distinguishable even with current density plots. However, square object which almost has zero conductivity is more distinguishable than circle object. This result is proved also by reconstructed images.

First, simulation results obtained with experimental phantom parameters are given. Original and reconstructed conductivity distributions are given in Figure 4.68.

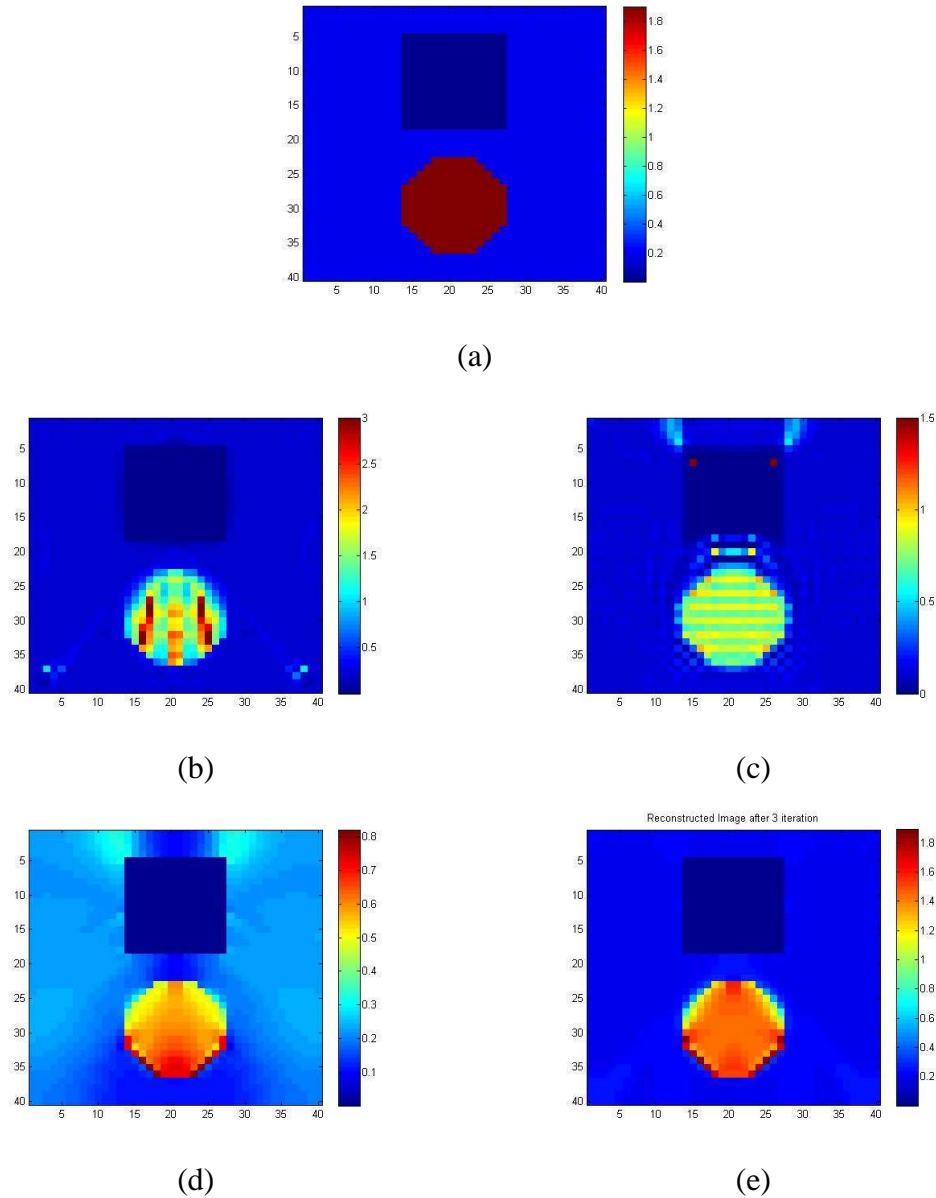
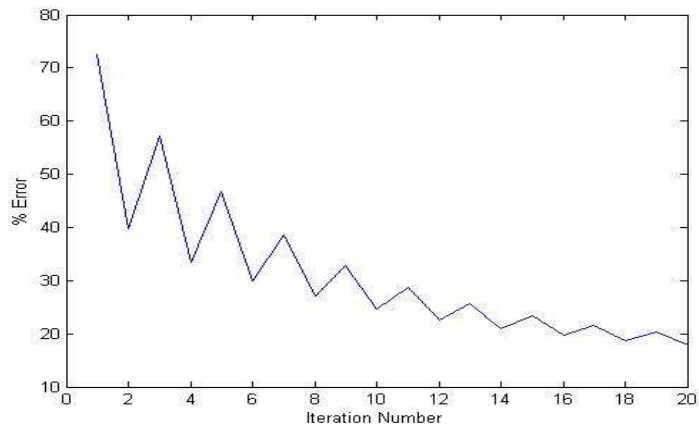
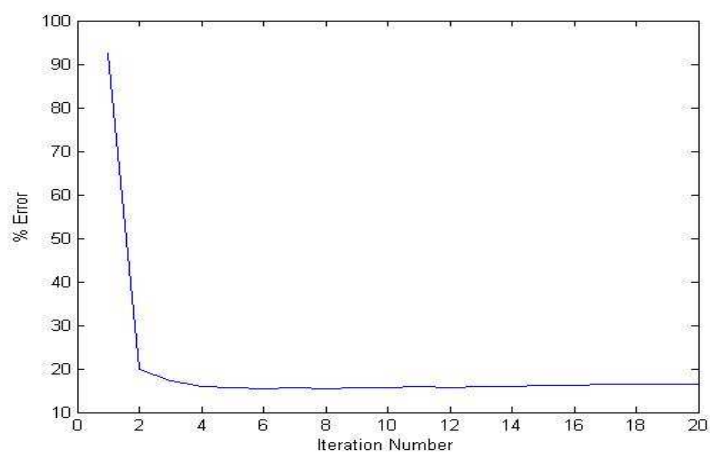


Figure 4.68 Reconstructed Images with Simulated Data for Experiment 2, a) Original Distribution, b) Equipotential-Projection, c) Solution as a Linear Equation System, d) J-Substitution (3 iteration), e) Hybrid (3 iteration)

According to these results, all reconstruction algorithms except Solution as a Linear Equation System succeeded in reconstructing the resistive square element. Although, boundaries of square element are visible for the result of Solution as a Linear Equation System algorithm, two extreme pixels with relatively high conductivity values distort image and increase error percentage dramatically. Moreover, typical grid artifact of Solution as a Linear Equation System algorithm is present here, too. Another important point is the relation between J-substitution and Hybrid algorithms. Hybrid algorithm has already reached to an optimum result where as J-substitution algorithm still needs to be iterated after three iterations. This phenomenon is also seen in Figure 4.69 where general error percentages with respect to iteration number are shown.



(a)



(b)

Figure 4.69 General Percentage Errors of a) J-Substitution, b) Hybrid algorithm

It is clear that, J-Substitution reaches the optimum error percentage value (%20) after 10 iterations, as Hybrid algorithm quickly converged to that value in a single iteration. This result is also another proof of optimization effect of Hybrid algorithm over J-Substitution algorithm.

Reconstructed conductivity distributions obtained with data of experiment 2 are given in Figure 4.70, Figure 4.71, Figure 4.72 and Figure 4.73. If results of experiment one and two are compared, some similarities will be realized. J-Substitution and Hybrid algorithms still have problems in FOV corners due to low amount of current and domination of noise, so these regions diverge to extreme values. Second, all algorithms are better in reconstructing resistive square element which is also expected. Third, Equipotential-Projection algorithm still has problems in reconstructing conductive circle element.

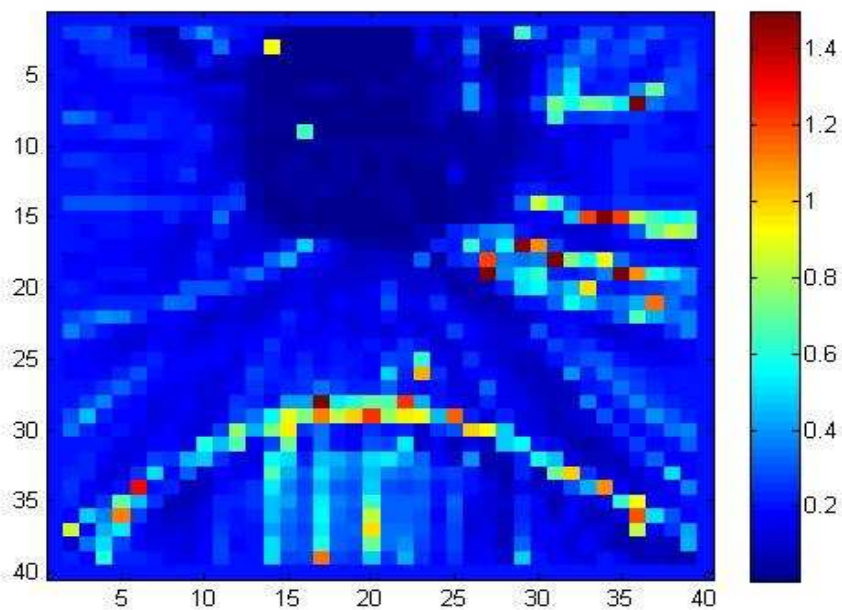


Figure 4.70 Reconstructed Image (S/m) with Equipotential-Projection Alg., Experiment 2

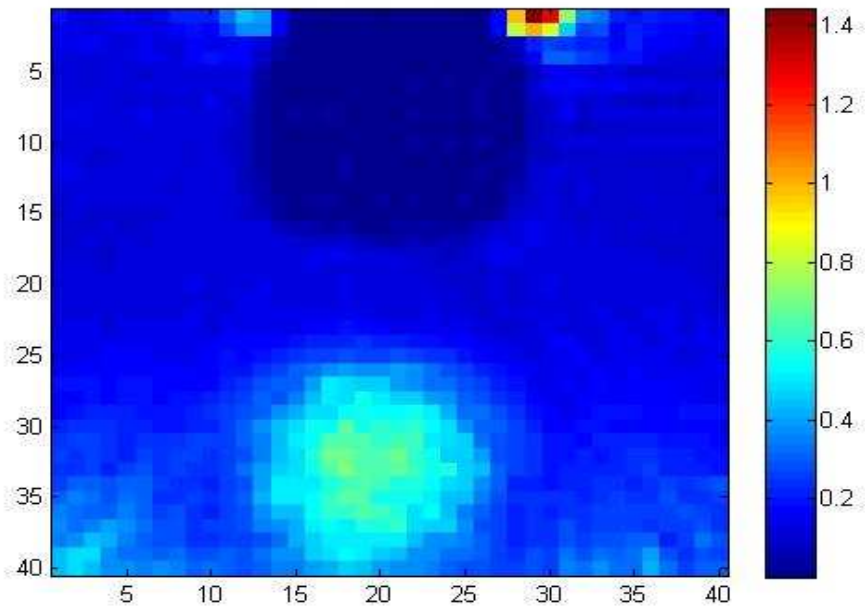


Figure 4.71 Reconstructed Image (S/m) with Solution as a Lin. Eq. Sys. Alg., Experiment 2

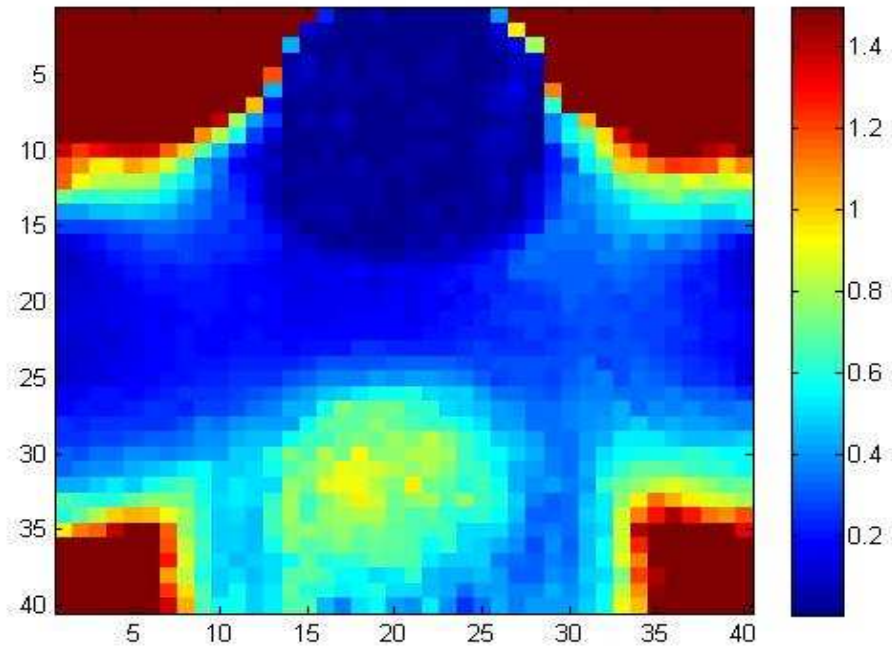


Figure 4.72 Reconstructed Image (S/m) with J-Substitution Alg., Experiment 2

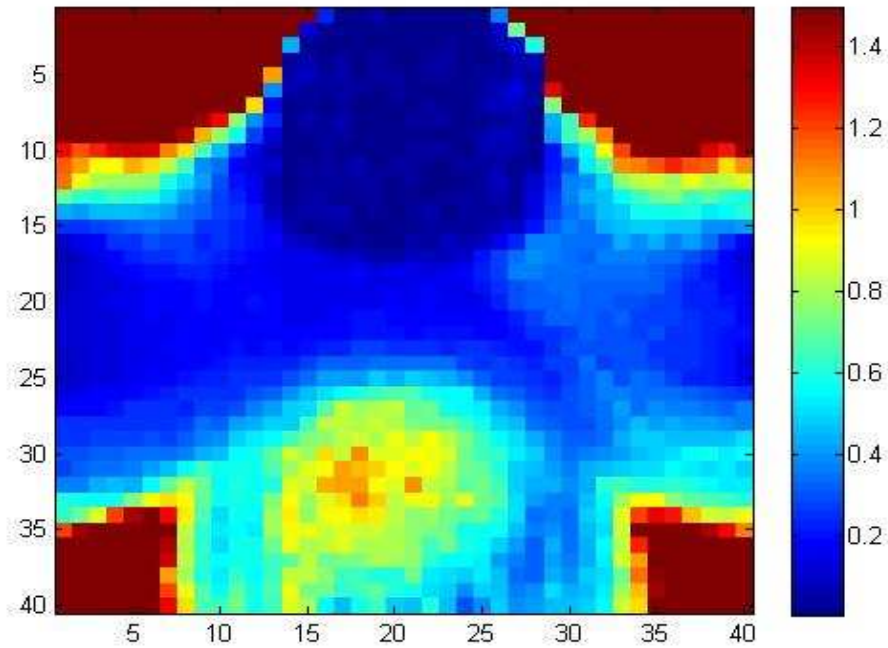


Figure 4.73 Reconstructed Image (S/m) with Hybrid Alg., Experiment 2

If corners of FOV are not considered, Solution as a Linear Equation System, J-Substitution and Hybrid algorithms have perceptually similar reconstructed images. Both circle and square elements are clearly distinguished. Table 4.4 shows error percentages of circle element in reconstructed images. Hybrid algorithm here continued its superior performance over J-substitution and other algorithms. Moreover, Solution as a Linear Equation System algorithm has a worse performance than J-substitution and Hybrid algorithms as conductivity contrast increases. Error percentage of square element is not considered since all algorithms fail to reconstruct this region with almost zero conductivity.

Table 4.4 Circle Element Error Percentages of Reconstructed Images

	<b>Sol. Lin. Eq. Sys.</b>	<b>EPP</b>	<b>J-substitution</b>	<b>Hybrid</b>
<b>Circle Element Error Percentage (%)</b>	77%	80%	69%	64%

## CHAPTER 5

### CONCLUSIONS AND FUTURE WORK

#### 5.1 Conclusions

In a previous study, Lorca [22] implemented and compared five J-based and a B-based MREIT reconstruction algorithms. The motivation of his thesis is to compare the algorithms with the same phantom. Moreover, he studied the effect of different noise levels. However, his study is based on a simulation with a rather simple phantom. Lorca stated in his thesis the future work possibilities which are simulations with different phantoms to compare performance of algorithms with different criteria. These criteria are position dependency, spatial resolution, electrode size, reconstruction time and perceptual analysis. So, in this thesis, J-based reconstruction algorithms are compared with five different simulation phantoms with the criteria mentioned above. Moreover, a novel J-based reconstruction algorithm is proposed which is a combination of Equipotential-Projection and J-Substitution algorithms.

Implemented J-based reconstruction algorithms are Integration along Equipotential Lines [19], Integration along Cartesian Grid Lines [19], Solution as a Linear Equation System [19], Equipotential-Projection [21], J-Substitution [20] and Hybrid algorithms [24]. Moreover, these algorithms are optimized with slight modifications to increase their performance. Regional and total reconstruction errors are calculated for each algorithm to make a numerical analysis.

Five different simulation phantoms are designed for simulation of reconstruction algorithms. The first model is explained in Section 4.2.1. Its purpose is to see the overall performance of reconstruction algorithms with two big square and circle elements. Also, it includes two impulsive elements.

Integration along Equipotential Lines algorithm has the worst performance with model 1 with respect to other algorithms. Errors are mainly due to element boundaries which are spread to the image with integration. However, using equipotential lines originated from four boundaries decreased total error dramatically. The other reason of errors is that some areas are not covered by equipotential lines leading to miscalculation of conductivity in these areas. Noise-free case yielded 64% error for Integration along Equipotential Lines algorithm and simulations with SNR 30 noise level produced 230% error. Moreover, with SNR 13, Integration along Equipotential Lines algorithm can not reconstruct conductivity distribution.

Integration along Cartesian Grid Lines algorithm also uses integration but it has a main advantage over Integration along Equipotential Lines algorithm such that it uses the information of two current injection patterns in a single step. Moreover, two integration strategies are employed for integration and their average is taken which enhances the performance of Integration along Cartesian Grid Lines algorithm. Elements of conductivity distribution reconstructed with Integration along Cartesian Grid Lines algorithm do not have sharp boundaries but still are definite. Addition of noise to current density data affected resistive elements more since current tends to flow outside of these elements. As a result, errors of these regions increased dramatically and spread to background with integration which distorts the reconstructed image. Integration along Cartesian Grid Lines algorithm has 21%, 26.8% and 83% total errors for noise-free, SNR 30 and SNR 13 cases, respectively.

Solution as a Linear Equation System algorithm also uses information from two current injection patterns and does not employ integration which result in a superior performance than Integration along Cartesian Grid Lines and Integration along Equipotential Lines algorithms. However, there is a typical grid artifact because to calculate the conductivity value of a single pixel, Solution as a Linear Equation System algorithm uses information only from four neighbor pixels. Element boundaries are sharper than Integration along Cartesian Grid Lines and Integration along Equipotential Lines algorithms. Moreover, Solution as a Linear Equation

System algorithm is robust noise producing 12.7%, 12.6% and 18.5% total errors for noise-free, SNR 30 and SNR 13 cases, respectively.

Equipotential-Projection algorithm uses equipotential lines started from four boundaries together. It reconstructs conductivity distribution with sharp boundaries but have erroneous lines originating from corners of FOV with SNR 13 noise level leading to distortion of reconstructed image.

J-Substitution and Hybrid algorithm produced the sharpest boundaries and perceptually better reconstructed images. Hybrid algorithm has a slightly better performance than J-Substitution algorithm in noise-free case as it has only 3% total error. But, addition of noise affected the performance of Hybrid algorithm because of the erroneous lines from the result of Equipotential-Projection algorithm.

Model 2 is used for spatial resolution analysis with calculation of FWHM values. Two cases, conductive and resistive, are used for simulation.

In the conductive case, J-Substitution and Hybrid algorithms have FWHM values of 0.225 cm which is equal to ideal case even when impulsive elements are closest to each other. On the other hand, Integration along Cartesian Grid Lines and Integration along Equipotential Lines algorithms produced FWHM values around 0.45 cm. Equipotential-Projection and Solution as a Linear Equation System algorithms have slightly bigger FWHM values than J-Substitution and Hybrid algorithms as they produced FWHM of 0.25 cm. Moreover, all algorithms' FWHM values are independent from distance between two impulsive elements.

In the resistive case, J-Substitution and Hybrid algorithms have FWHM around 0.235 cm which has 5% error with respect to ideal case. As in the conductive case, Cartesian Grid Lines and Integration along Equipotential Lines algorithms has the worst performance with FWHM around 0.55 cm. Equipotential-Projection and Solution as a Linear Equation System algorithms have FWHM values around 0.35 cm. All algorithms have FWHM values independent from distance between two impulsive elements in the resistive case.

Model 3 is designed to see the position dependency of reconstruction algorithms which has a resistive and conductive case. Simulation results show that all algorithms are independent from position both for conductive and resistive cases but some algorithms can not reconstruct impulsive elements with their true values and define element boundaries sharply.

Simulations with model 4 reveal the numerical accuracy of reconstruction algorithms with changing conductivity contrast. The conductivity of square element in the center of FOV is increased and decreased gradually for conductive and resistive cases, respectively. In the conductive case, when conductivity contrast is increased general error is increased for all algorithms. However, all algorithms except Integration along Cartesian grid Lines algorithm converge to an error value. When square conductivity is 2 S/m, general errors are 5.2%, 8.1%, 9%, 32% and 47% for Hybrid, J-Substitution, Equipotential-Projection, Solution as a Linear Equation System and Integration along Cartesian Grid Lines algorithms, respectively.

When error percentage of square is considered, all algorithms' error values increase but converge to some value except Integration along Cartesian Grid Lines algorithm in the conductive case.

For the resistive case, Integration along Cartesian Grid Lines, Integration along Equipotential Lines and Solution as a Linear Equation System algorithms have divergence characteristics for general error when conductivity contrast is increased. They reach to general errors of 80% for Integration along Equipotential Lines and 35% for Integration along Cartesian Grid Lines and Solution as a Linear Equation System algorithms when square element has a conductivity contrast of 1/10 with respect to background conductivity. For that case, Hybrid, J-substitution and Equipotential-Projection algorithms converge to general errors of 4.5%, 7.6% and 6.3%, respectively. Here, optimization effect of Hybrid algorithm over J-Substitution algorithm is more obvious.

The above conclusions still apply when square error is considered. As conductivity contrast increases Integration along Cartesian Grid Lines, Integration along

Equipotential Lines and Solution as a Linear Equation System algorithms diverge whereas Hybrid, J-substitution and Equipotential-Projection algorithms converge to square errors of 2.5%, 5.6% and 11%, respectively.

The last simulation phantom is the thorax phantom with a complex geometry and true tissue conductivities. Thorax phantom is also used with noisy data simulations of SNR 30 and SNR 13. Moreover, regional and total errors are calculated for each reconstruction algorithm to make a numerical analysis.

Integration along Equipotential Lines algorithm failed in reconstructing conductivity distribution even in the noise-free case. Most of the equipotential lines can not make it to another boundary and are eliminated. The remaining equipotential lines are not sufficient to reconstruct an image.

All algorithms reconstructed spinal cord region inside bone structure with around 100% error, because current can not get into bone structure and forces spinal cord inside to be reconstructed with conductivity value of bone.

Integration along Cartesian Grid Lines algorithm has the largest regional and total error values because it is based on integration of conductivity gradient. The conductivity gradient reaches to its maximum values at the boundary between bone element and other regions. So, errors from these regions are distributed to other elements and especially to the background. Moreover, addition of noise affected these areas the most due to relatively low current density and increased both regional and total errors dramatically.

For the case Solution as a Linear Equation System algorithm, all elements are separated from each other but the boundaries are not sharp. Regional error for bone element is increased much more than other regions because of the low current density. Moreover, typical grid artifact is also present with thorax phantom simulations.

Equipotential-Projection algorithm produced the sharpest boundaries with thorax phantom but lacked reconstructing each element with its true conductivity value. When noise is added typical erroneous lines originating from corners of FOV start to distort image and increase both regional and background errors.

The most satisfying results both numerically and perceptually are obtained with Hybrid and J-Substitution algorithms. The success of Hybrid algorithm in reconstructing regions in the center of FOV is clearly seen with thorax phantom simulations. The error of heart region is around 20% for Hybrid algorithm whereas J-substitution algorithm has around 40% error. However, typical erroneous line artifact of Equipotential-Projection algorithm dominates lung region and background errors of Hybrid algorithm which in turn forces Hybrid algorithm to have higher total errors than J-Substitution algorithm.

As a part of the thesis work, an MREIT experiment is conducted as explained in Section 0 and Appendix A. Measured magnetic fields and all components used in the calculation of current density data are given in Section 4.5.6. Measured current density data is consistent with simulation data. However, current density deviations due to square and circle elements of experimental phantom are not enough to reconstruct these elements. Therefore, another experiment including elements with high conductivity contrast with respect to background conductivity can be conducted.

Main reasons of errors in experimental data are alignment problems, position of slices and calculation of magnetic field derivatives. Therefore, special care must be taken in every step of data collection.

According to the reconstruction results obtained with data of experiment 1, Solution as a Linear Equation System algorithm is the most successful one since it reconstructed both circle and square element partially. This result is expected as Solution as a Linear Equation System algorithm proved to be robust to noise especially in low conductivity contrast regions and experimental phantom has a conductivity contrast of only 2. Therefore, when conductivity contrast increases, Solution as a Linear Equation System algorithm may have a poorer performance.

Also, Equipotential-Projection algorithm has a partial reconstruction where square element is slightly distinguished. On the other hand, J-Substitution and Hybrid algorithms can not reconstruct conductivity distribution. Moreover, noise becomes dominant in corners of FOV for J-Substitution and Hybrid algorithms. Integration along Equipotential Lines and Integration along Cartesian Grid Lines algorithms can not reconstruct conductivity distribution with data of experiment 1.

Another experiment with a higher conductivity contrast is also conducted where circle element's conductivity is increased to 1.9 S/m and square element is designed to have nearly zero conductivity. Background is still set to 0.2 S/m. According to results of experiment 2, Solution as a Linear Equation System, J-substitution and Hybrid algorithms reconstructed both circle and square elements clearly. However, conductivity values at corners of FOV diverge for J-Substitution and Hybrid algorithm since these regions have lower current density and more vulnerability to noise. When error percentages for circle element are investigated, Hybrid algorithm seems to have the lowest error which shows its superiority to J-substitution algorithm. Equipotential-Projection algorithm can only reconstruct resistive square element whereas Integration along Equipotential Lines and Integration along Cartesian Grid Lines algorithms failed with data of experiment 2.

A star plot is designed to see the overall performance of reconstruction algorithms with aforementioned criteria. These are reconstruction time, noise performance, error performance, electrode size and reconstructed image quality. Different simulation results are chosen for each criterion as mentioned below.

- Error comparison with noisy data is performed with total error results of SNR 13 simulations with model 1.
- Error comparison is performed by noise-free case simulations of model 1.
- Image quality comparison is carried out with thorax phantom results, such that each reconstruction algorithm is graded from 1 to 5 with respect to its performance.

- Electrode size is 9 cm for Integration along Equipotential Lines, Integration along Cartesian Grid Lines and Solution as a Linear Equation System algorithms and 1.8 cm for other algorithms.
- Reconstruction time for Hybrid and J-substitution algorithms is the time elapsed for three iterations.
- Experimental performance comparison is done with percentage error of circle element for experiment 2.

Number of potential measurements and current injection patterns are not included in comparison since they use the same number of these parameters for consistency. Each axis of star plot is discretized with the numerical results shown in Table 5.1. Discretization of each axis is made in a way that as the distance from origin increases, the performance gets better. For example, reconstruction time axis is plotted with 1/(reconstruction time) values. Star plot is shown in Figure 5.1.

Table 5.1 Numerical Values for Star Plot

	<b>Integ. Eq. Pot</b>	<b>Integ. Cart. Grid</b>	<b>Sol. Lin. Eq. Sys</b>	<b>EPP</b>	<b>Jsub</b>	<b>Hybrid</b>
<b>Reconstruction Time</b>	<b>10 s</b>	<b>10 s</b>	<b>10 s</b>	<b>10 s</b>	<b>8 min</b>	<b>8 min</b>
<b>Noise Error</b>	<b>233%</b>	<b>83%</b>	<b>18.5%</b>	<b>15.7%</b>	<b>18.1%</b>	<b>19.3%</b>
<b>Error</b>	<b>64%</b>	<b>21.2%</b>	<b>12.7%</b>	<b>6.9%</b>	<b>4.6%</b>	<b>3%</b>
<b>Electrode Size</b>	<b>9 cm</b>	<b>9 cm</b>	<b>9 cm</b>	<b>1.8 cm</b>	<b>1.8 cm</b>	<b>1.8 cm</b>
<b>Image Quality</b>	<b>1</b>	<b>2</b>	<b>4</b>	<b>3</b>	<b>5</b>	<b>5</b>
<b>Experimental Error</b>	<b>-</b>	<b>-</b>	<b>77%</b>	<b>80%</b>	<b>69%</b>	<b>64%</b>

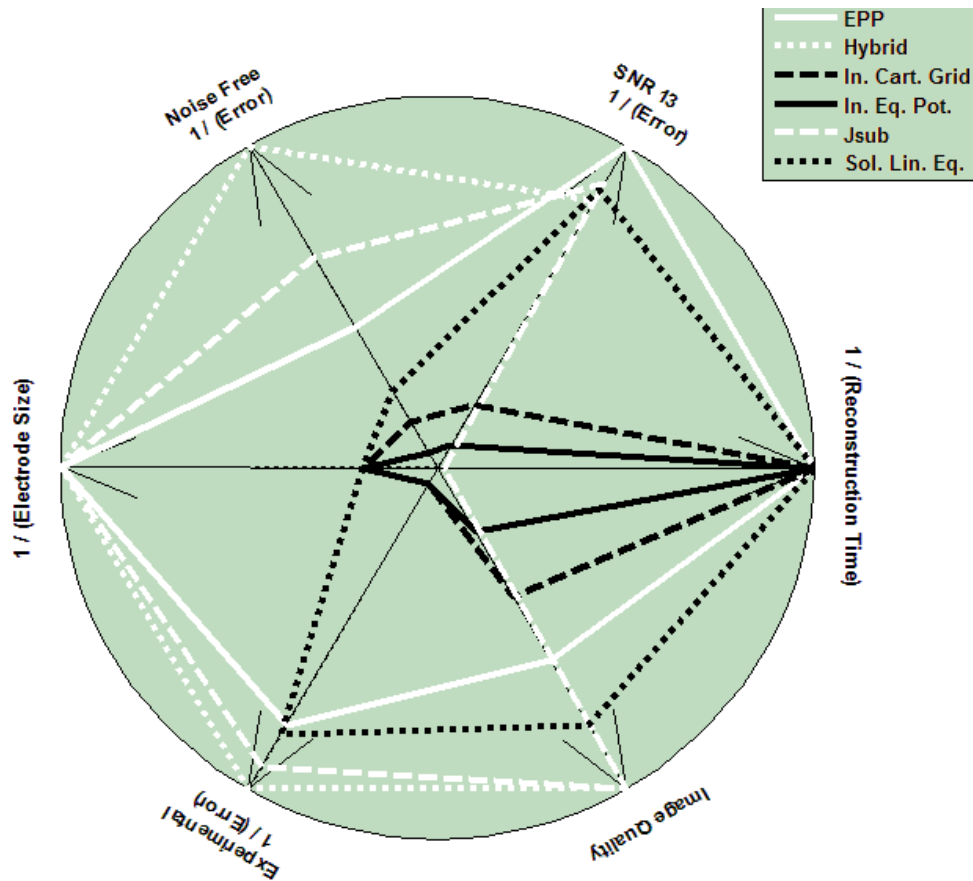


Figure 5.1 Star Plot

## 5.2 Future work

In this thesis, current density ( $J$ ) based MREIT reconstruction algorithms are implemented and optimized with slight modifications. Moreover, these algorithms are compared both with simulated and experimental data set with respect to different criteria. Some future work possibilities are:

- More experiments can be conducted especially with high conductivity contrast phantoms.
- Another MRI system with a higher SNR level can be used.

- Numerical methods for perceptual analysis on performance of reconstruction algorithms can be developed.
- Experiments with real tissues can be conducted.

## References

- [1] Boone, K., Barber, D., & Brown, B. (1997). Imaging with electricity: Report of the European Concerted Action on Impedance Tomography. *Journal of Medical Engineering & Technology* , 21 (6), 201-232.
- [2] Bayford, R. H. (2006). Bioimpedance Tomography (Electrical Impedance Tomography). *Annual Review of Biomedical Engineering* , 8, 63-91.
- [3] Henderson, R. P., & Webster, J. G. (1978). An Impedance Camera for Spatially Specific Measurements of the Thorax. *IEEE Transactions on Biomedical Engineering* , BME-25 (3), 250-254.
- [4] Barber, D. C., & Brown, B. H. (1984). Applied Potential Tomography. *Journal of Physics E: Scientific Instruments* , 17 (9), 723-733.
- [5] Brown, B. H. (2003). Electrical Impedance Tomography (EIT): A Review. *Journal of Medical Engineering & Technology* , 27 (3), 97-108.
- [6] Holder, D. S. (2005). *Electrical Impedance Tomography* (1st ed.). Bristol and Philadelphia: Institute of Physics Publishing.
- [7] Gençer, N. G., Kuzuoğlu, M., & Ider, Y. Z. (1994). Electrical Impedance Tomography Using Induced Currents. *IEEE Transaction on Medical Imaging* , 13 (2), 338-350.
- [8] Gençer, N. G., İder, Z. Y., & Williamson, S. J. (1996). Electrical Impedance Tomography: Induced-Current Imaging Achieved with a Multiple Coil System. *IEEE Transactions on Biomedical Engineering* , 43 (2), 139-149.
- [9] Gençer, N. G., & Tek, N. M. (1999). Electrical Conductivity Imaging via Contactless Measurements. *IEEE Transactions on Medical Imaging* , 18 (7), 617-627.

- [10] Gencer, N. G., & Tek, N. M. (1999). Forward Problem Solution For Electrical Conductivity Imaging via Contactless Measurements. *Physics in Medicine & Biology*, 44 (4), 927-940.
- [11] Tek, M. N. (1998). Electrical Conductivity Imaging via Contactless Measurement: Forward and Inverse Problem Simulations. Unpublished master's thesis, Middle East Technical University. Ankara, Turkey.
- [12] Scott, G. C., Joy, M. L., Armstrong, R. L., & Henkelman, R. M. (1991). Measurement of Nonuniform Current Density by Magnetic Resonance. *IEEE Transactions On Medical Imaging*, 10 (3), 362-374.
- [13] Scott, G. C., Joy, M. L., Armstrong, R. L., & Henkelman, R. M. (1992). Sensitivity of Magnetic-Resonance Current-Density Imaging. *Journal of magnetic resonance*, 97 (2), 235-254.
- [14] Zhang, N. (1992). *Electrical Impedance Tomography Based on Current Density Imaging*. MSc Thesis, Department of Electrical Engineering, University of Toronto. Toronto, Canada .
- [15] Woo, E. J., Lee, S. Y., & Mun, C. W. (1994). Impedance Tomography Using Internal Current Density Distribution Measured by Nuclear Magnetic Resonance. *Proceedings of Society of Photo-Optical Instrumentation Engineers (SPIE) Conference Series, Mathematical Methods in Medical Imaging III*, 2299, pp. 377-385.
- [16] Ider, Y. Z., & Birgül, Ö. (1998). Use of the Magnetic Field Generated by the Internal Distribution of Injected Currents for Electrical Impedance Tomography (MR-EIT). *Turkish Journal of Electrical Engineering & Computer Sciences*, 6 (3), 215-226.
- [17] Eyüboğlu, M., Birgül, Ö., & Ider, Y. Z. (2001). A Dual Modality System for High Resolution - True Conductivity Imaging. *Proceedings of XIth International Conference on Electrical Bio-impedance*, (pp. 409-413). Oslo - Norway.
- [18] Eyüboğlu, B. M. (2006). Magnetic resonance – Electrical Impedance Tomography (MR-EIT) Research at METU. Proc. of 7th Conference on Biomedical Applications of Electrical Impedance Tomography, Joint Conference of World Congress on Medical Physics and Biomedical Engineering, 14, pp. 136-139. Seoul – Korea.

- [19] Ider, Y. Z., Onart, S., & Lionheart, W. R. (2003). Uniqueness and Reconstruction in Magnetic Resonance–Electrical Impedance Tomography (MR–EIT). *Physiological Measurement* , 24, 591-604.
- [20] Kwon, O., Woo, E. J., Yoon, J.-R., & Seo, J. K. (2002). Magnetic Resonance Electrical Impedance Tomography (MREIT): Simulation Study of J-Substitution Algorithm. *IEEE Transactions On Biomedical Engineering* , 49 (2), 160-167.
- [21] Ozdemir, M. S., Eyuboglu, B. M., & Özbek, O. (2004). Equipotential projection-based magnetic resonance electrical impedance tomography and experimental realization. *Physics In Medicine And Biology* , 49, 4765-4783.
- [22] Lorca, D. M. (2007). Implementation and Comparison of Reconstruction Algorithms for Magnetic Resonance-Electrical Impedance Tomography (MR-EIT). MSc. thesis, Middle East Technical University. Ankara, Turkey .
- [23] Eyüboğlu, B. M., Reddy, R., & Leigh, J. S. (May 28, 2002). *Patent No. U. S. 6,397,095 B1*. United States of America.
- [24] Boyacıoğlu, R., & Eyüboğlu, B. M. (2009). J-Substitution and Filtered Equipotential-Projection Based Hybrid MREIT Reconstruction Algorithm. *U Proc. of 11th World Congress of Medical Physics and Biomedical Engineering , Munich, Germany*.
- [25] Joy, M., Scott, G., & Henkelman, M. (1989). In-Vivo Detection of Applied Electric Currents by Magnetic Resonance Imaging. *Magnetic Resonance Imaging* , 7, 89-94.
- [26] Scott, G. C. (1993). *N M R Imaging of Current Density and Magnetic Fields*. PhD Thesis, University of Toronto, Canada .
- [27] Weinroth, A. P. (1998). *Fast Radio-Frequency Current Density Imaging With Spiral Acquisition* . MSc. Thesis, University of Toronto, Canada .
- [28] Carter, M. A. (1995). *RF Current Density Imaging with a Clinical Magnetic Resonance Imager*. Msc. Thesis, University Of Toronto, Canada .
- [29] Quarteroni, A., Sacco, R., & Saleri, F. (2007). *Numerical mathematics* . Berlin ; New York: Springer.

- [30] Birgül, Ö. (2002). Development of Reconstruction Algorithms for Magnetic Resonance Electrical Impedance Tomography and Experimental Realization. PhD Thesis, Middle East Technical University, Department of Electrical Engineering. Ankara, Turkey .
- [31] Özbek, O. (2002). *Imaging Current Density Distribution Using 0.15T Magnetic Resonance Tomography*. Master's thesis, Middle East Technical University, Ankara, Turkey, department of Electrical Engineering .
- [32] Geddes, L. A., & Baker, L. E. (1967). The Specific Resistance of Biological Material—A Compendium of Data for the Biomedical Engineer and Physiologist. *Medical and Biological Engineering and Computing* , 5 (3), 271-293.
- [33] Rush, S., Abildskov, J., & Mcfee, R. (1963). Resistivity of Body Tissues at Low Frequencies. *Circulation Research* , 12, 40-50.
- [34] Woo, E. J., Seo, J. K. (2008). Magnetic resonance electrical impedance tomography (MREIT) for high-resolution conductivity imaging. *Phys. Meas.*, 29, 1-26.
- [35] TX151 and TX150 Product Information,  
<http://www.oilcenter.com/ProductInformationSheets/N-Z/Txproducts.pdf>
- [36] Birgül, Ö., Eyüboğlu, B. M., & Ider, Y. Z. (2003). Current constrained voltage scaled reconstruction (CCVSR) algorithm for MR-EIT and its performance with different probing current patterns. *Phys. Med. Biol.* , 48, 653-671.
- [37] Saha, G. B. (2005). Basics of PET Imaging: Physics, Chemistry, and Regulations. Springer.
- [38] Özsüt, M. (2005). Design and implementation of labview based data acquisition and image reconstruction environment for Metu-mri system. Master's thesis, Middle East Technical University, Ankara, Turkey, Department of Electrical Engineering
- [39] Agar-Agar Technical Information,  
<http://www.merck-chemicals.com/>

- [40] Hasanov, K., F., Ma, A., W., Nachman, A., I., Joy, M., L., G. (2008). Current Density Imaging. *IEEE Transactions On Medical Imaging*, 27, 1301-1309.
- [41] Oh, T. I., Koo, H., Lee, K. H., Kim, S. M., Lee, J., Kim, S. W., Seo, J. K., Woo, E., J. (2008). Validation of a multi-frequency electrical impedance tomography (mfEIT) system KHU Mark1: impedance spectroscopy and time-difference imaging. *Physiol. Meas.*, 29, 295-307.

## APPENDIX A

### MREIT EXPERIMENT PROCEDURE

In Appendix A, experimental setup and procedure for experiment 1 will be explained in detail. In Section 2.5 and Section 4.2.6, general information about data extraction and MREIT experiments is given. In this chapter, further information is provided for interested reader.

In Figure A.1, general setup for a conventional MREIT experiment is given. Main components are MRI system (main magnet and RF coil), current source and phantom. These components will be explained in detail.

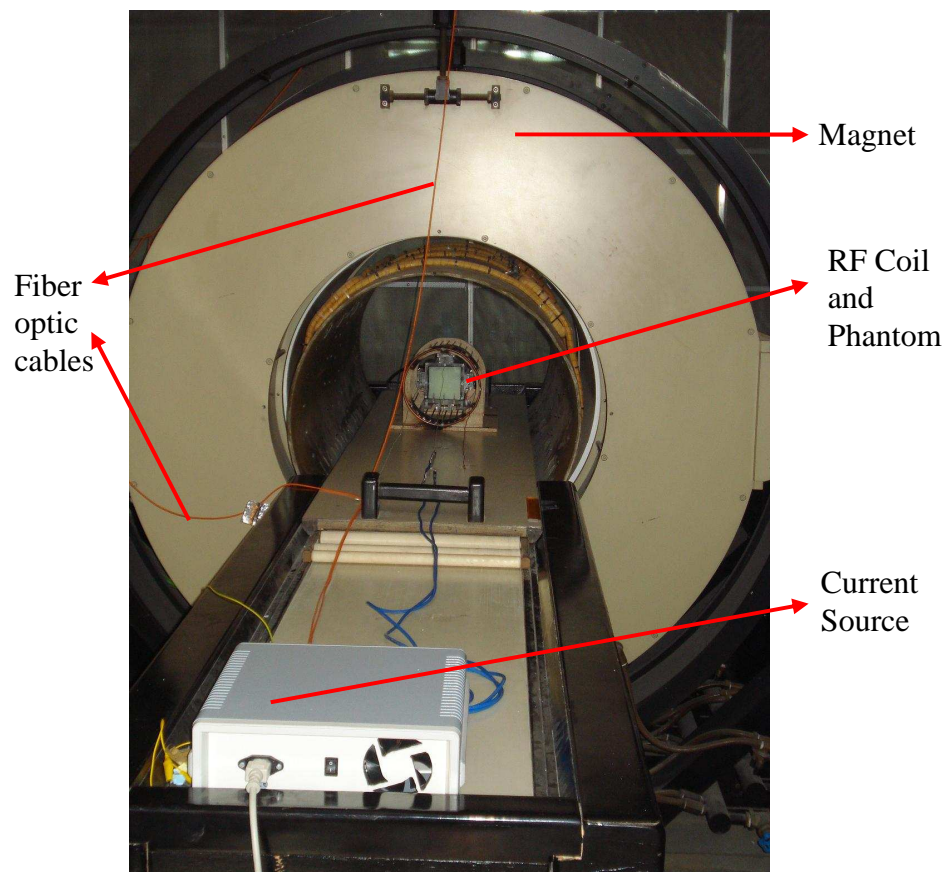


Figure A.1 General Setup for MREIT Experiments

0.15 T METU MRI system is used for conducting the experiments. MRI system is controlled by a software which is designed by Özsüt [38]. Moreover, pulse sequence parameters are assigned and data collection is performed utilizing this software. Another important component is the RF coil which serves both as a transmitter and receiver coil. RF coil in Figure A.2 is designed and implemented as a part of the thesis work. Before data collection, the RF coil has to be tuned.



Figure A.2 RF coil with the phantom inside.

Next component is the current source used for current injection. In a previous study, Özbek [31] designed a current source to conduct MREIT experiments with METU MRI system. However, control of METU MRI system has changed which forced to design and implement a new current source. Two pictures of the current source from the front and back side are shown. The new current source is based on Özbek's design with the difference that trigger for current injection is taken directly from pulse sequence and trigger information is carried to the current source with fiber optic cables to eliminate noise interference. So, a transmitter and a receiver unit are added to previous design for fiber optic transmission. As can be seen in Figure A.3a, there is a BNC output in front of the current source. It measures the voltage on a resistor of

$10\Omega$ , that is the applied current amplitude can be found by dividing the voltage seen by 10.



Figure A.3 Current Source a) Front View, b) Back View

Next step is preparing the phantom. As explained in Section 0, a plexiglas phantom is constructed which is shown in Figure A.4. 2D geometry is obtained with plexiglas walls seen in Figure A.4b. These walls force the current applied to flow between them.

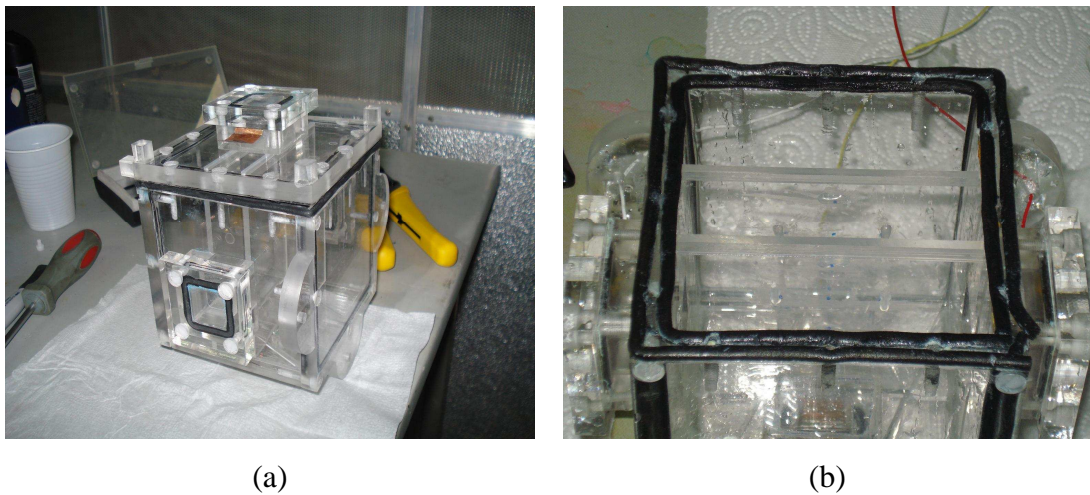


Figure A.4 Plexiglas Phantom, a) Oblique View, b) Upper Side Removed

Phantom elements are prepared with different combinations of three solidifying materials, TX151 [35], TX150 [35] and Agar-Agar [39]. Moreover, NaCl is added to the solutions to increase conductivity. TX151 and TX150 are used to reduce ion diffusion [40]. Also,  $\text{CuSO}_4$  (1g/L) is added to every solution to fix  $T_1$  relaxation time [31]. Preparation procedure for phantom elements is as follows [41],

- NaCl is added to distilled water and solution is stirred.
- TX151, TX150 and Agar-Agar are added and solution is boiled.
- Boiled solutions are poured quickly inside molds shown in Figure A.5

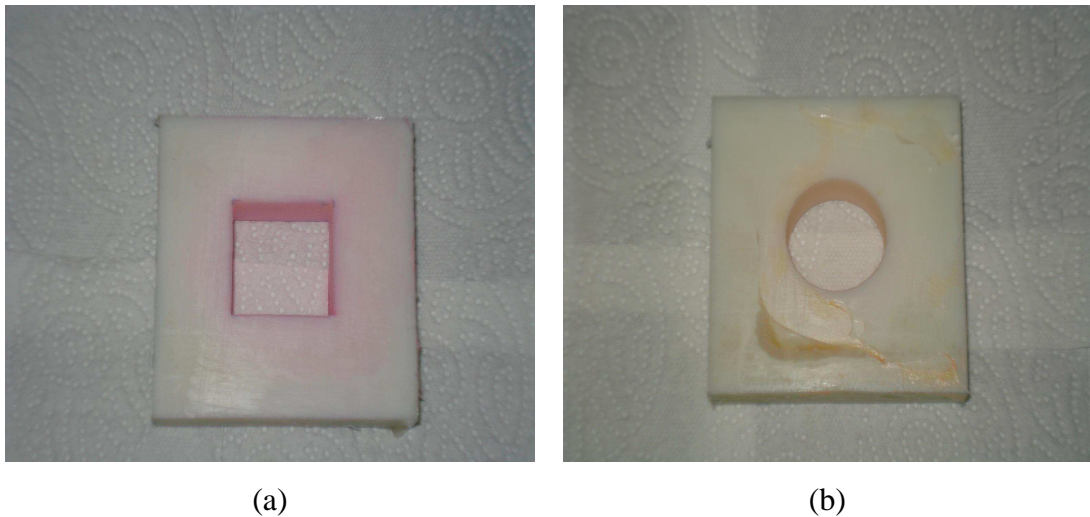


Figure A.5 Molds for Phantom Elements, a) Mold for Square Element, b) Mold for Circle Element

After phantom elements inside the molds are hardened, they are taken out and put inside plexiglas phantom as in Figure A.6. The same preparation procedure is applied to background solution which is poured into the phantom just after phantom elements are placed, shown in Figure A.6b. Critical point for all preparation procedure is the amount of all solidifying materials, distilled water and NaCl inside phantom elements. Conductivity of all elements are found with conductivity cell in Figure A.7. Conductivity values of all elements are determined after each solution is poured and hardened inside conductivity cell. When the solution is hardened inside the

conductivity cell, its conductivity value is also fixed. Amounts of all TX151, TX150, Agar-Agar, distilled water and NaCl for each phantom element are given in Table A.1.

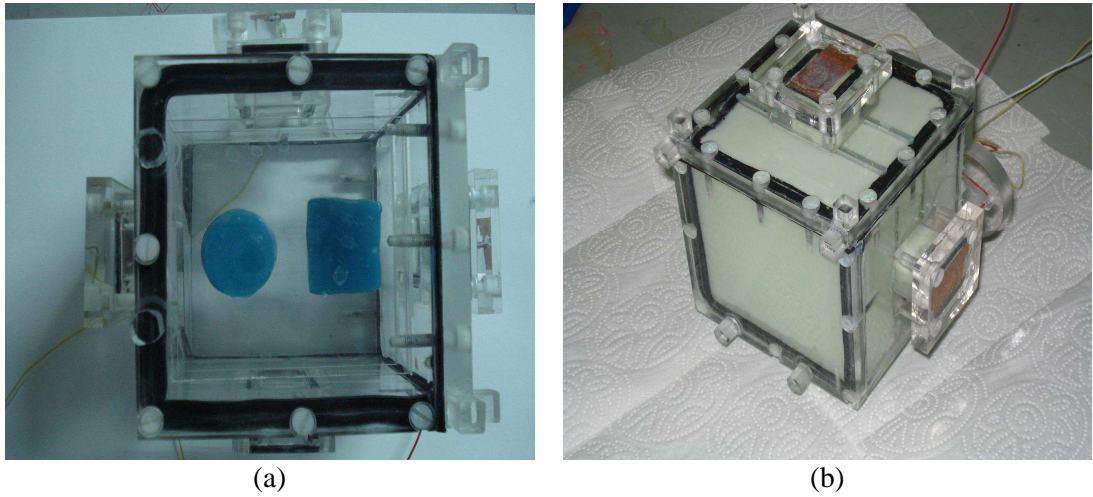


Figure A.6 Phantom with all Elements, a) Phantom Elements, b) Phantom Elements and Background Solution



Figure A.7 Conductivity Cell

Table A.1 Composition of Phantom Elements

	Square Element (0.1 S/m)	Circle Element (0.4 S/m)	Background Solution (0.2 S/m)
Agar-Agar	0.5 g	1 g	-
TX151	-	1 g	1.8 g
TX150	1 g	-	0.2 g
CuSO <sub>4</sub>	0.1 g	0.1 g	0.1 g
Distilled Water	100 ml	100 ml	100 ml
NaCl	-	0.1 g	0.1 g

After experimental phantom is prepared data collection stage starts. In Figure A.8, basic MREIT pulse sequence is illustrated. Here, slice selection, phase encoding and frequency encoding gradients are in  $z$ ,  $y$  and  $x$  directions, respectively.

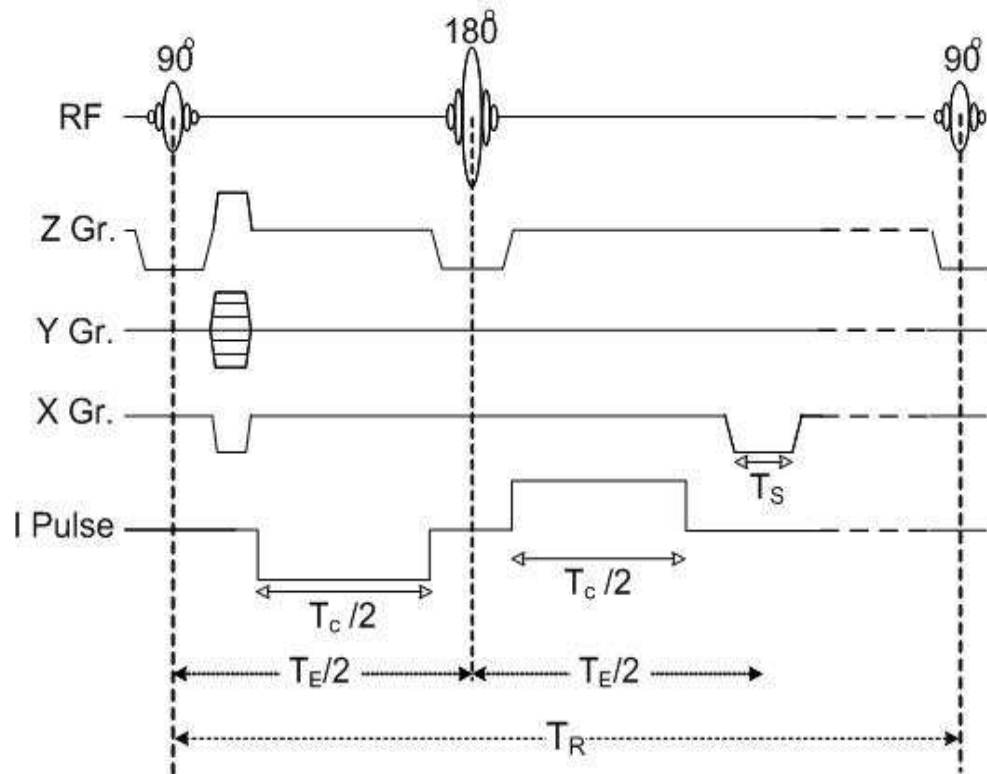


Figure A.8 MREIT Pulse Sequence

Screenshot of the software used for pulse sequence design and data collection for METU MRI system is shown in Figure A.9 for imaging  $B_z$  component. Procedure for imaging  $z$  component of magnetic field ( $B_z$ ) is as follows,

- Current electrodes are connected to the current source.
- Negative current is applied for horizontal current injection and phase image is obtained.
- Current polarity is changed to positive current injection and phase image is obtained.
- Magnetic field ( $B_z$ ) is extracted as explained in Section 2.5
- Above steps are repeated for vertical current injection



Figure A.9 Screen Shot Image of MRI software for  $B_z$  imaging

Next step is obtaining magnetic field in  $x$  direction ( $B_x$ ). First, phantom orientation is changed such that imaging slice is orthogonal to  $x$  direction. In that configuration slice selection, phase encoding and frequency encoding gradients are in  $x$ ,  $y$  and  $z$  directions, respectively. Screen shot of the software for  $B_x$  imaging is shown in Figure A.10. Data collection procedure is the same as the general procedure explained above with the following changes,

- Slice position is adjusted to 5 mm above the center of imaging slice in  $x$  direction and above procedure is repeated.
- Slice position is adjusted to 5 mm below the center of imaging slice in  $x$  direction and above procedure is repeated.



Figure A.10 Screen Shot Image of MRI software for  $B_x$  imaging

Then,  $B_x$  is extracted as explained in Section 4.5.6. Imaging of  $y$  component of magnetic field ( $B_y$ ) is done in the same way as imaging of  $B_x$  with the difference that slice positioning is done in  $y$  direction. Screen shot of MRI software for  $B_y$  imaging is shown in Figure A.11. Here, slice selection, phase encoding and frequency encoding gradients are in  $y$ ,  $z$  and  $x$  directions, respectively.

After all components of magnetic field are obtained current density data both in  $x$  and  $y$  directions ( $J_x$  and  $J_y$ ) are obtained as explained in Section 4.5.6.



Figure A.11 Screen Shot Image of MRI software for  $B_y$  imaging